UNIVERSIDADE DA BEIRA INTERIOR
Engenharia

Design and Analysis of the Mechanical Behaviour of Adhesively-Bonded CFRP T-Joints

João Manuel Vieira Cardoso

Dissertação para obtenção do Grau de Mestre em

Engenharia Aeronáutica

(Ciclo de estudos integrado)

Orientador: Prof. Doutor Abílio Manuel Pereira da Silva

Orientador: Prof. Doutor Pedro Vieira Gamboa

Covilhã, outubro de 2018

This page intentionally left blank

Ao meu avô, Manuel Vieira, que desde cedo me transmitiu o valor incontestável do conhecimento.

This page intentionally left blank

Acknowledgements

Firstly, I would like to gratefully thank my supervisor, Prof. Abílio Silva, for his invaluable support throughout the development of this dissertation, sharing with me his large expertise and experience, and providing me with all the necessary conditions to develop the experimental part of this project.

I would also like to thank Prof. Pedro Gamboa, for all the time he gave to this project, sharing his knowledge and viewpoints, which were many times critical to solve questions that once seemed unsolvable.

To Prof. Paulo Fael, I thank for giving me his insights on various occasions, providing me with the point of view I needed on more technical questions.

To João Nunes Pereira, I thank for accompanying and advising me during all the phases of this work. His valuable guidance and experience were crucial to perceive some mistakes during reviewing.

To the FabLab's personnel, particularly João Correia, I am truly grateful for all the time he gave to this work, supporting me with his incredible know-how, and without which would not be possible to fabricate the specimens. To Prof. Hélder Correia, I must thank for his time and effort fabricating one of the tools, with equipment and technical knowledge that otherwise would not be possible.

From the Optical Centre (Electron Microscopy Laboratory), I thank Óscar Rato and Ana Paula for providing me with the fantastic SEM images that really extended the value of this project.

To Sónia Sousa, I thank for all the hours and outstanding helpfulness performing the water contact angle measurements.

To António Morgado and Francisco Borges, I thank for the time and help while performing the roughness measurements.

To my uncle, Domingos Vieira, and Mecânidraulica, I am thankful for the fabrication of some metal tools and fixtures necessary for the experimental part.

To my family, especially my mother, Luciana Vieira, my sincere gratitude for all the support during these years, and for providing me with all the conditions to conclude the course I love.

To my girlfriend, I will always be grateful for her unconditional support at all times, giving me the strength and positivity when I most needed.

To all my friends, I am thankful for their absolute friendship, even when work times restricted my social interactions with them during these years.

Finally, my gratitude goes to the C-MAST for the opportunity to take this work further, to the University of Beira Interior as an institution and to its staff, and to all the DCA and DEM teachers for the knowledge transmitted during the past years.

This Master's Dissertation has been supported by the project Centro-01-0145-FEDER-000017 – EMaDeS – Energy, Materials and Sustainable Development, co-financed by the Portugal 2020 Program (PT 2020), within the Regional Operational Program of the Center (CENTRO 2020) and the European Union through the European Regional Development Fund (ERDF).

This page intentionally left blank

This page intentionally left blank

Abstract

Adhesively bonded joints have been increasingly applied in primary aerostructures, mainly due to their numerous advantages over mechanically fastened joints. More specifically, bonded T-joints made from carbon fibre reinforced plastics (CFRPs) are commonly found as stiffening members on wing panels and fuselage sections.

Despite the well-known advantages of composites, aluminium stiffeners can yet be considered a safer and more conservative solution, since composite T-joints face delamination problems that typically initiate at the central noodle of the stiffener – the part where the three arms of the stiffener come together – and propagate through the adhesive bondline.

In order to better comprehend the failure mechanisms and failure sequence on these joints when subjected to out-of-plane loadings, stiffener pull-off tests (SPOTs) were experimentally conducted on two CFRP (SEAL® Texipreg HS 160 REM) adherends – skin and stiffener – adhesively bonded with a structural film adhesive (SEAL® Texipreg EA451 U150).

The effects of different surface treatments, curing methods, and noodle filling materials were experimentally studied. Moreover, the bonding surfaces were characterized using scanning electron microscopy, profilometry and contact angle measurements. After failure, the fracture surfaces were analysed by visual inspection, optical microscopy and, in particular cases, SEM fractography to better understand the failure mechanisms. Conclusions from the surface characterization and fractography analysis were properly correlated with the obtained SPOT results.

A novel fabrication method was developed to eliminate the problem of the twisted fibres at the noodle that occur during the curing stage, re-engineering the noodle region with the scope of increasing the through-thickness strength of the joint. This manufacturing alternative proposes a modification to the conventional fabrication scheme, effectively increasing the damage tolerance of the bonded joint.

Keywords

CFRP T-joint; Adhesive bonding; SPOT; Failure sequence; Fractography.

This page intentionally left blank

Resumo

As juntas adesivas têm sido cada vez mais utilizadas em estruturas aeronáuticas primárias, principalmente devido às suas numerosas vantagens em relação a juntas rebitadas ou aparafusadas. Particularmente, juntas em "T" compósitas de matriz polimérica e reforçadas com fibras de carbono (*CFRP*) são frequentemente encontradas como membros enrijecedores (*stiffeners*) em painéis de asas e seções de fuselagem.

Apesar das vantagens bem conhecidas dos materiais compósitos, as juntas em "T" em alumínio ainda podem ser consideradas uma solução mais segura e conservadora, visto que as juntas em "T" compósitas enfrentam problemas de delaminação que normalmente se iniciam no preenchimento central do enrijecedor – a parte onde a alma e o banzo se juntam – e propagam-se ao longo da conexão adesiva.

Com o intuito de compreender melhor os mecanismos e sequência de falha neste tipo de juntas quando sujeitas a carregamentos fora do plano, foram conduzidos experimentalmente ensaios de arrancamento do enrijecedor ("*SPOTs*") em dois aderentes de *CFRP* (SEAL® Texipreg HS 160 REM) – casco (*skin*) e enrijecedor – colados com um filme adesivo estrutural (SEAL® Texipreg EA451 U150).

Foram estudados experimentalmente os efeitos do tratamento de superfície, dos diferentes métodos de cura, e de diferentes materiais de enchimento da zona central do enrijecedor. Além disso, as superfícies tratadas e não tratadas foram caracterizadas através de microscopia eletrónica de varrimento, perfilometria, e medições do ângulo de contato. Após o descolamento, as superfícies de fratura foram analisadas por inspeção visual, microscopia óptica e, em alguns casos particulares, por fratografia através de microscopia eletrónica para melhor compreensão dos mecanismos e modos de falha. As conclusões sobre a caracterização das superfícies e da análise fratográfica foram devidamente correlacionadas com os resultados dos ensaios "*SPOT*".

Um novo método de fabricação foi desenvolvido para eliminar o problema das fibras torcidas que tipicamente ocorre durante a cura dos provetes em "T", redesenhando a região central do enrijecedor com o objetivo de aumentar a sua resistência ao longo da espessura (eixo z). Esta alternativa de fabricação preconiza uma modificação no esquema de fabricação convencional, aumentando efetivamente a tolerância ao dano da junta colada.

Palavras-chave

Junta em "T" de *CFRP*; Ligação adesiva; *SPOT*; Sequência de falha, Fractografia.

This page intentionally left blank

List of Contents

This page intentionally left blank

This page intentionally left blank

List of Figures

This page intentionally left blank

This page intentionally left blank

List of Tables

This page intentionally left blank

List of Acronyms

AF	Adhesive Failure
AFP	Automated Fibre Placement
ASL	Automated Stringer Lamination
ASS	Apparent Shear Strength
ASTM	American Society for Testing and Materials
ATL	Automated Tape Laying
ATP	Automated Fibre Placement
CF	Carbon Fibre
CFRP	Carbon Fibre-Reinforced Polymer
CMC	Ceramic-Matrix Composite
CNC	Computer Numerical Control
CZM	Cohesive Zone Model
DF	Drape Forming
FEA	Finite Element Analysis
FEP	Fluorinated Ethylene Propylene
FRP	Fibre-Reinforced Polymer
FST	Fire, Smoke, Toxicity
FTF	Fibre-Tear Failure
FW	Filament Winding
HLU	Hand Layup
HS	High Strength
ISC	*In situ* consolidation
LFTF	Light-Fibre-Tear Failure
MF	Mixed Failure
NASA	National Aeronautics and Space Administration
NDT	Non-Destructive Test
OOA	Outside-Of-Autoclave
OW	Owens-Wendt
PC	Polycarbonate
PEEK	Polyetheretherketone

PEI	Polyetherimide
PPS	Polyphenylene Sulfide
REM	Resin Epoxy Matrix
RFI	Resin Film Infusion
RTM	Resin Transfer Moulding
SBF	Stock-Break Failure
SEM	Scanning Electron Microscope/Microscopy
SFEV	Surface Free Energy Value
SLJ	Single Lap Joint
SLST	Single Lap Shear Test
SPOT	Stiffener Pull-Off Test
STV	Surface Tension Value
TDS	Technical Data Sheet
TEM	Transmission Electron Microscope/Microscopy
TLCF	Thin-Layer Cohesive Failure
TP	Thermoplastics Forming
UD	Unidirectional
VCCT	Virtual Crack Closure Technique
WCA	Water Contact Angle

Nomenclature

T_g	Glass Transition Temperature
E	Young's Modulus
γ_{SG}	Surface Free Energy of the Solid
γ_{LG}	Surface Tension of the Liquid
θ	Contact Angle
θ_W	Apparent Contact Angle
θ_Y	Young Contact Angle for an Ideal Surface
$\bar{r}$	Average Roughness Ratio

σ_{max}	Tensile Strength
ε	Tensile Failure Strain
R_a	Roughness Average
R_q	RMS (Root Mean Square) Roughness
R_t	Maximum Height of the Profile
R_{pm}	Average Height of Peaks
R_{3z}	Third Maximum Peak-to-Valley Height
R_{zISO}	Ten Point Height of Irregularities
R_{zDIM}	Average Peak-to-Valley Height
L	Evaluation Length
l	Sampling Length
$\delta_{P_{max}}$	Displacement at Maximum Lad
$\delta_{P_{fail}}$	Displacement at Failure Load
$\delta_{P_{init}}$	Displacement at Crack Initiation
P_{max}	Maximum Load
P_{fail}	Failure Load
P_{init}	Crack Initiation Load
$K_{P_{max}}$	Stiffness at Maximum Load
$K_{P_{fail}}$	Stiffness at Failure Load
$K_{P_{init}}$	Stiffness at Crack Initiation
G_I	Energy Release Rate Mode I
G_{II}	Energy Release Rate Mode II

This page intentionally left blank

Chapter 1 – Introduction

Along this chapter, an overview of the importance of composite materials on the aerospace industry will be made, with a particular focus on the growing use of adhesive joints. The motives that led to this work will be mentioned, the objectives will be defined and finally, each chapter will be briefly described, as well as its organization.

1.1. Motivation

Composites based upon thermosetting or thermoplastic polymeric matrices, and containing glass, aramid, or carbon fibres, are being increasingly used in many diverse applications. Particularly, the aerospace industry has been using composite materials for a long time, and their usage is effectively increasing throughout the years, mainly because composite materials offer superior specific strength and stiffness when compared to the traditional metals [1].

Consequently, composite materials have become, together with aluminium alloys, the main structural materials for aircraft primary structures [2]. As it can be seen in Figure 1, since Boeing 787 and Airbus A350XWB have entered in service, composite materials officially claimed more than 50% of the structural weight of commercial aircraft [3].

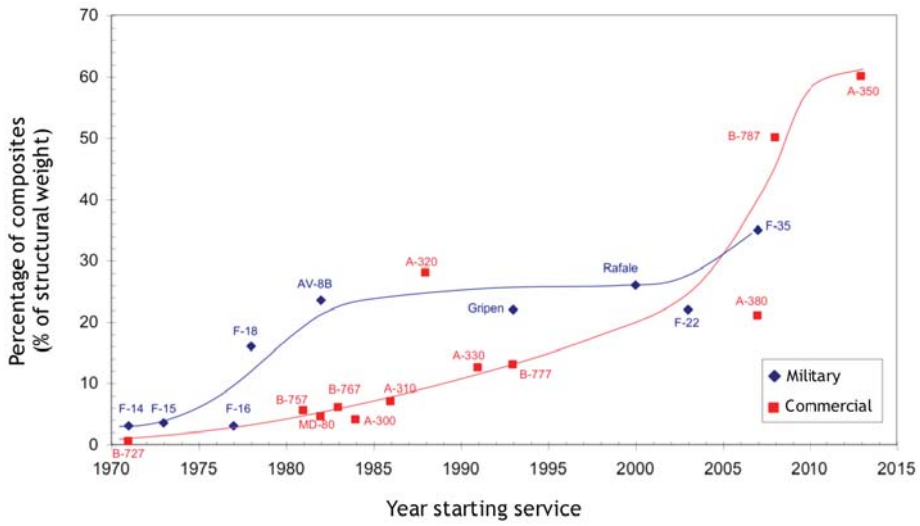

Figure 1 – Evolution of composites' implementation in aircraft structures. Data from [4-6].

However, in order to fully exploit the weight-savings potential of composite materials in full-scale structures, a suitable joining technology must be implemented; and although mechanical fastening has been the standard method for joining aircraft structures, adhesion is attracting increasing interest as a direct alternative to these mechanical methods [2].

Adhesive bonding of aircraft primary structures has been in use for over seventy years [7], but it was not until the last two decades that, with the intensive use of composites in the aerospace industry, adhesives have really emerged as a more adequate joining technology between different structural parts.

It is known that mechanical fastening can damage the composite by breaking its fibres and hence creating local defects and stress concentrations around the holes – both of which reduce the overall structural integrity with decreased performance of the composite laminate [2,8]. By contrast, adhesive bonding not only avoids that, but it also brings a lot of other potential advantages like lower structural weight, lower fabrication cost, improved damage tolerance and superior fatigue resistance [1,8]. Moreover, bonded joints are more continuous, have better design flexibility, and can be considered easier to fabricate. For all these reasons, adhesive bonding has found applications in several engineering applications, from high technology industries such as aerospace, marine, electronics, and automotive; to more traditional industries such as construction, sports, and packaging [8,9].

To what the aerospace industry concerns, there has been an increased use of adhesive bonding, especially for joining and repairing structural components made of fibre-reinforced composites [8]. Figure 2 illustrates the various applications of adhesive bonding in the Airbus A380, which considerably benefits from the reduced weight offered by the bonded composite assemblies [10].

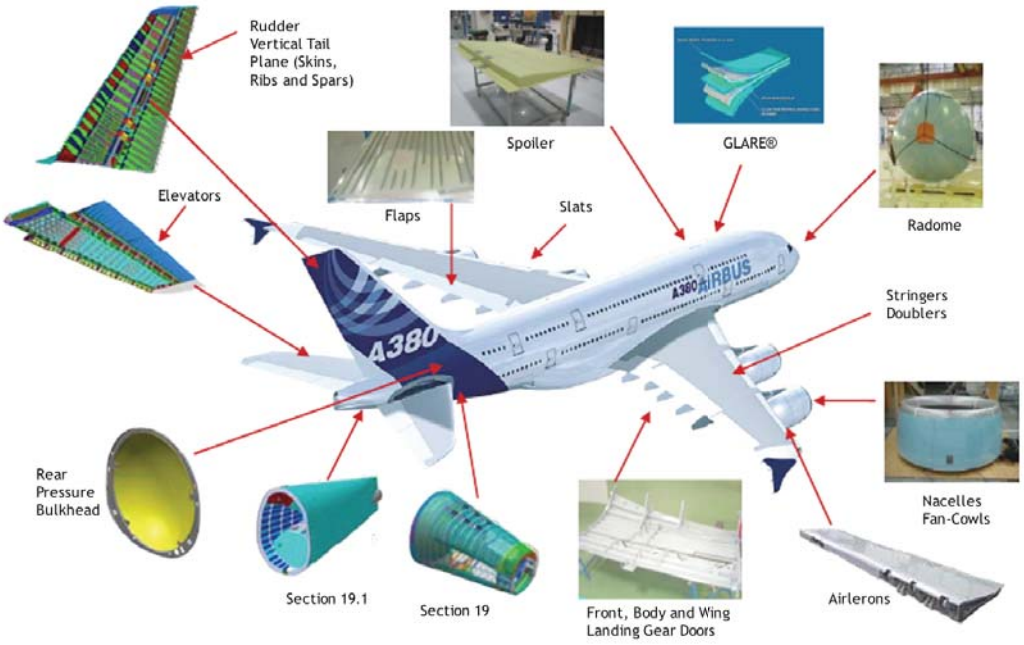

Figure 2 – Exemplary applications of adhesive bonding in the Airbus A380 [10].

In aircraft applications, skin-to-stiffener joints are very common in fuselage panels (Figure 3) and wings, with stiffeners being adhesively bonded to skin sections such as the fuselage or wings [7].

Figure 3 – Composite (Carbon fibre/PEEK) skin panel with co-bonded T-stiffeners [11].

Despite the potential advantages of adhesive bonding, there remains a lack of knowledge – and therefore trust – on the behaviour and performance of adhesively-bonded joints, which has resulted in a tendency to overdesign these structures [8]. Besides, safety authorities often require to include mechanical fasteners as an additional safety precaution, resulting in highly inefficient structures [1,12], which in the particular case of the skin-to-stiffener connection, where were found to be outperformed by their aluminium equivalents [1]. Freitas [13] concluded that the aluminium stiffeners have become highly optimized throughout the last decades, while composite structures still need a lot of research to reach their true potential in terms of weight and performance. Freitas suggested that this can be made by optimizing the design methodology and geometry, and by tailoring the laminate anisotropic properties, making the bonded joint stronger and more damage tolerant, with the aim of lowering the design safety factors.

Lots of the shortcomings of bonded joints were studied and resolved during the last years by developing new materials, methods and models [9]. However, there is still a potential to evaluate and identify the best possible combination of parameters, conceiving novel ideas and technologies which would give the best performance of composite bonded joints [9].

The majority of the research on adhesively bonded joints focus on simplified joints (e.g. single lap joints) and tested with coupon tests [1,14]. However, in order to be applied in the industry, composite bonded joints also need to prove their performance in structural applications and not only at the coupon level [1]. On the other hand, full-scale structures are often unfeasible to test (especially in the aerospace industry), and sub-components tests can be alternatively used to simulate the loading and boundary conditions of full-scale components without compromising the possibility to test different design concepts and materials.

Stiffener pull-off tests (SPOTs) are a particular example of these sub-component tests, which simulates out-of-plane loadings in skin-to-stiffener joints, such as the internal pressure of the fuselage skin and low-pressure zones of the leading edges [3].

SPOTs have been extensively used to evaluate the performance of different design concepts and structural features of skin-to-stiffener joints [1,3,15-32]. However, despite being able to provide a good description of the failure sequence and failure modes, these research papers fail to provide an effective and relatively easy method for improving the through-thickness strength of the joint, especially at the noodle region – were the failure usually initiates.

It is possible to say that with the increasing use of composites over metals, attention should be paid on how this replacement of materials influences the structure's behaviour, and if, or if not, they can perform according to the aviation and aerospace standards. The development of reliable design and predictive methodologies for bonded structures can be expected to result in a more efficient use of composites and adhesives, lower structural weight, and lower material and manufacturing costs [12], acting as a future enabler for secured certification [33]. Figure 4 illustrates the evolution of the number of published documents on the topic of adhesive bonding, following a very increasing trend which attests the ongoing search for testing, optimizing, and predicting the behaviour of adhesive joints.

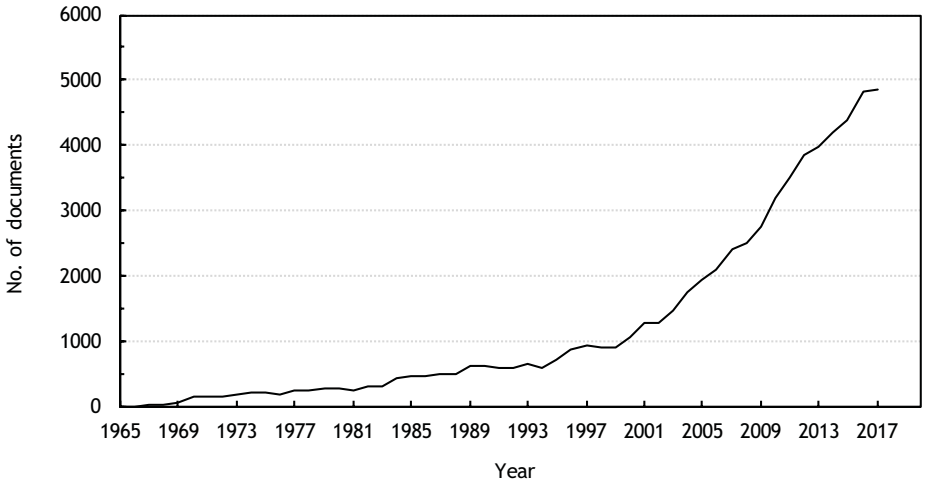

Figure 4 – Evolution (by year) of the number of published documents containing the terms "adhesive bonding" [34].

1.2. Objectives

This project aims to primarily understand the behaviour of skin-to-stiffener T-joints using different methodologies, starting from the comprehension of the mechanisms occurring at a fundamental level, and then moving to the fabrication and design optimization of this particular joint.

In order to do so, the following objectives were outlined:

- Study and presentation of the state-of-the-art in composite materials and adhesively bonded joints; particularizing for the aerospace industry whenever possible.
- Testing and acquisition of some of the main mechanical properties of the bulk adhesive.
- Fabrication of single lap joints and skin-to-stiffener T-joints using relatively easy methods and accessible tools.
- Testing single lap joints using single lap shear tests (SLSTs), while performing a preliminary evaluation of the influence of surface treatment.
- Characterization of the differently treated surfaces using optical and scanning electron microscopy (SEM), surface roughness measurements (profilometry), and contact angle measurements.
- Evaluation of the mechanical performance of differently treated T-joints using stiffener pull-off tests (SPOTs).
- Evaluation of the different procedures to cure the bonded T-joint.
- Design optimization of the T-joint with the aim of increasing its through-thickness strength and evaluation of the different noodle filling materials.
- Characterization of the fracture surfaces using scanning electron microscopy (SEM), identifying the failure mechanisms and failure modes.

1.3. Dissertation Outline

This dissertation is divided into five chapters, which are structured in the following manner:

- The current Chapter 1 consists of a short contextualization of adhesive bonding, introducing the motives that led to this work, with particular emphasis on composite materials, adhesively bonded joints, and skin-to-stiffener joints. The objectives are then properly defined; followed by the organization of this document, with a brief description of each chapter.
- Chapter 2 entails the literature review, which addresses the state-of-the-art of composites and adhesive bonding, presenting and deliberating the most relevant topics – starting from the importance of composite materials and their usage in the aerospace industry, and then particularizing to the adhesively bonded joints and skin-to-stiffener joints.
- Chapter 3 is divided into two sections: Section 3.1, which describes the experimental setup, materials used, fabrication and mechanical testing of the bulk adhesive, specimens' geometry and dimensions for both the single lap joints and the skin-to-stiffener joints (T-joints), and the process carried out to fabricate both types of joints. In section 3.2, the experimental methodology is presented, addressing the methods and techniques used to perform the characterization of the different surfaces and the experimental testing of single lap and skin-to-stiffener joints. At the end of this section, the methodology used to perform the fractographic analysis on the fracture surfaces is described.
- Chapter 4 exposes the obtained results, performing a comprehensive analysis and discussion of the findings from the surface characterization, mechanical testing, and fractographic analysis of the fracture surfaces. Illustrative charts, tables and figures were used whenever possible; and the results were discussed with comparison with the literature.
- Chapter 5 summarizes all the conclusions that resulted from this project, and presents some guidelines for future research.

Annex A provides the typical properties of adhesives used in structural applications, namely epoxies, cyanoacrylates, anaerobics, acrylics, polyurethanes, silicones, and high-temperature adhesives (phenolics, polyimides, and bismaleimides).

Lastly, a Glossary is presented with some of the terms commonly used regarding the subject of adhesive bonding, particularly those referred throughout this document.

Chapter 2 – Literature Review

This chapter addresses the fundamental concepts that relate to the subject of this work, with particular focus on composite materials and adhesive bonding. Starting from a more general approach on adhesively bonded joints, and then moving to the more particular case of the skin-to-stiffener connection, several relevant topics will be presented and discussed using the existing literature. The major developments concerning the study of composite bonded joints will also be presented.

2.1. Composite Materials

Composite materials are undoubtedly becoming more and more important in the fabrication of aerospace structures. From what started out to be a small-scale implementation during the 1960s, with only aircraft parts such as fairings and spoilers being made from composite materials due to their weight savings over aluminium parts [6], the new generation of commercial aircraft use composites on their primary structures such as fuselage and wings – accounting for more than 50% of the total weight of the aircraft as illustrated in Figure 1. This intensive growth in composites usage has required an in-depth knowledge of the behaviour of composite materials [6].

2.1.1. Definition

There are a number of definitions as to what actually is a composite material, but the most overarching probably is: “the combination of two or more distinctly different materials to make an improved or superior material” [35]. Although these individual materials do not dissolve or merge completely in the composite and can often be physically identified [36], they act together as one, producing a material with superior properties than the constituent materials – matrix and reinforcement – from which it is constructed [37].

While there are many classes of composites materials, hereinafter the focus will be on fibre-reinforced polymers (FRP), particularly the ones using carbon fibres (carbon fibre-reinforced polymers, CFRP) which is the most important polymer-matrix fibre material for composite aircraft structures [6] and the very subject of this project.

2.1.2. Matrix

The matrix has the function of supporting the fibres and bonding them together in the composite material. It transfers any applied loads to the fibres, keeps the fibres in their position and orientation, provides the composite environmental resistance and determines its maximum service temperature [37].

As the name implies, fibre-reinforced polymers' matrix is a polymer, often named resin as a generic term. The chemical composition and physical properties of the resin fundamentally affect the processing, fabrication, and ultimate properties of the composite material [6].

There are two main types of resins: Thermosetting and thermoplastics. Thermosetting resins (thermosets) are the most diverse and widely used of all man-made materials. They are easily poured or formed into any shape, compatible with most materials, and cure readily (by heat or catalyst) into an insoluble solid. Thermosetting resins are also excellent adhesives and bonding agents [37]. On the other hand, thermoplastic resins can be softened repeatedly by an increase of temperature and hardened by a decrease in temperature [37,38]. Chemical curing of the material does not take place during processing, and the material can be shaped by moulding or extrusion when it is soft. In fact, processing speed is the primary advantage of thermoplastic materials when compared to thermosets [37].

2.1.3. Reinforcement

Fibre-reinforced polymers (FRP), as the name implies, are reinforced by some type of fibrous material. Specifically, the so-called advanced fibres (such as glass, carbon, kevlar, or ceramic fibres) possess very high strength and very high stiffness coupled with a very low density, and for that reason they are the primary load carrying element of any FRP composite [38]. Consequently, the resulting composite has predominant mechanical properties in the direction of the fibres, and for that reason is said to be anisotropic [37,38].

In order to take advantage of the directional strength characteristics of composites, the fibres must be placed layer by layer in orientations and patterns that optimize their strength and stiffness for a given application, producing optimum mechanical properties and hence a structurally efficient design. For example, 0° plies should be placed to react to axial loads, ±45° plies to react to shear loads, and 90° plies to react to side loads [37].

Although true isotropic properties (as found on metals) are virtually unreachable, it is possible to obtain quasi-isotropic properties from a proper sequence of plies' orientation, or by using multiaxial fabrics (several directions of reinforcement) [6]. Unidirectional tape products (one direction of reinforcement), however, have a higher strength than woven fabrics and can be tailored to a specific part and purpose [37].

2.1.4. Trends in the Aerospace Industry

Since the early development of composites, the aerospace sector has undoubtedly been a very important innovation leader when it comes to the use of fibre composite materials in the industry. While forty years ago aluminium clearly dominated the aerospace industry, times have changed and we can now say the same about composite materials on recent commercial aircraft [39].

The primary advantages that come with the use of composite materials on aerospace and aircraft structures are their high strength, high stiffness, corrosion resistance, and reduced weight (consequently increasing fuel efficiency); while still being relatively easy to handle, design, and repair [37]. Another main advantage is that composite components can be formed into complex shapes, consequently reducing the need for fasteners and joints – which are not only heavy but also potential failure points. This has led to an industry-wide trend of fewer components in overall assemblies, using one-piece designs wherever possible [39].

Although there are many existing and emerging types of composite materials – like ceramic-matrix composites (CMCs), for example – carbon fibre-reinforced polymers (CFRPs) represent the biggest share of composite materials in both cabin and functional components [39].

Among the available CFRPs, unidirectional prepreg tapes have been the standard in the aerospace industry. Prepregs consist of a combination of a fibre reinforcement (in the form of unidirectional tape or fabric) which has been pre-impregnated with the resin matrix (thermosetting or thermoplastic) in a very well defined ratio [37]. As a consequence, prepregs are ready to be laid up into the tool without the addition of any more resin, resulting in several advantages such as: maximum mechanical properties (due to optimal fibre content), low void content, part uniformity, repeatability, cleanliness, and easiness to use.

The procedure associated with curing prepreg composites (thermosets) typically requires a manual bagging operation and an autoclave cycle, using a combination of pressure and heat to achieve full polymerization of the matrix.

Although thermoset resins and autoclave curing have been the mainstays of aerospace composites since their introduction in aircraft, the use of autoclaves was found to be accompanied by high costs, which stem from high acquisition and operating costs. The reduction of these inherent costs is a priority for many airframe manufacturers [40].

For the reasons formerly mentioned, there has been an intensive research focused on finding new methods that eliminate the expensive, energy inefficient, time-consuming, and bottleneck (limited size and manufacturing rates) of bagging and autoclave curing procedures of composites [41,42]. This has been done in two ways: evolving to more automated processes that could increase the pace of production; and by developing new materials and outside-of-autoclave (OOA) methods for composites, specifically thermoplastics [42].

As it is possible to see in Figure 5, automated processes like automated tape laying (ATL) and automated fibre placement (AFP) are the fastest growing processes in recent years and are expected to represent, by 2020, about 50% of all the manufacturing processes used for the production of aircraft components. These automated processes use computer-guided robotics to lay one or several layers of CF prepregged tape (ATL) or tows (AFP) onto a tool to create a part or structure. During this additive process, the fibres are placed layer by layer, in precise orientations and patterns that optimize their strength and stiffness for a given application [41,43]. Some advantages of the ATL/AFP processes, when compared to conventional hand layup, include: material and labour savings, quality improvement, accurate fibre placement at any angle and allowing breaks, and automatic debulking [41]. These systems can be adapted for both thermoset and thermoplastic materials – however, tape laying is traditionally used, if not always, with thermosets [44,45].

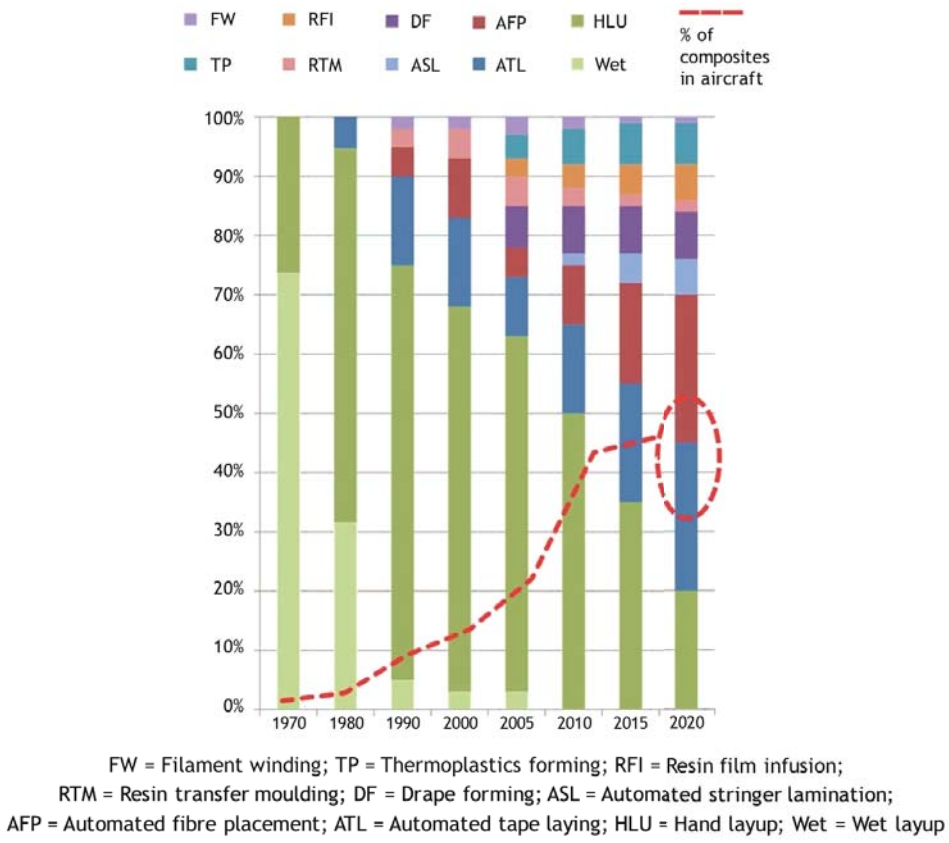

Figure 5 – Change in CFRP manufacturing process vs. airframe content [46].

Prepregs currently used in the aerospace industry are typically impregnated with thermosetting resins, mostly epoxy or polyester. This leads to matrices possessing relatively high values of surface free energy and hence making them more receptive to adhesive bonding [8,47]. In particular, epoxy based composites have fantastic compatibility with other epoxy adhesives.

Notwithstanding, thermoplastic matrices have gained popularity in the last years, and their projected increase in process share is significantly higher than thermosets. Composites based upon thermoplastic polymers typically employ matrices such as polyetheretherketone (PEEK), polyphenylene sulfide (PPS), polyetherimide (PEI), polycarbonate (PC), etc. [46].

Thermoplastic polymers tend to have low values of surface free energy and for that reason are difficult to bond using standard engineering adhesives. In fact, work has concluded that bonding thermoplastic composites using acrylic and epoxy adhesives, based upon abrasion and solvent cleaning pretreatment techniques, leads to significantly lower joint strengths when compared with thermosetting-based composites [47]. However, more recently, different welding technologies have been proposed for thermoplastic matrix composite bonding [48,49] with various degrees of success. This latter option, not possible with thermosets, offers great potential when it comes to fuse or weld moulded subcomponents by co-consolidation and without the use of fasteners or adhesives [46].

Despite some setbacks when put in comparison with thermosets, high-performance thermoplastic prepregs are highly attractive to the aerospace industry. This has to do, in part, to their combination of high fracture toughness, high damage tolerance, long (possibly indefinite) out life and high recyclability compared to thermoset matrices [41,50]. Other advantages over thermosets include [41,47]:

- Melt processability (no curing chemistry, no long soak times);
- Superior solvent and chemical resistance;
- No toxicity/hazardous chemical issues;
- No refrigeration or out-time considerations;
- Great FST (fire, smoke, toxicity) stability;
- Hydrolytic stability – low water absorption;
- Stable glass transition temperature (T_g) even in hot/wet conditions;
- Good fatigue resistance;
- Low coefficient of friction;
- High abrasion resistance.

Thermoplastics are difficult and expensive to process using the methods traditionally used for thermosets (vacuum bagging and autoclave curing) due to their lack of tack and high temperature requirements. This has led to increasing research in the area of *in situ* consolidation (ISC) – which means "consolidation in place" – by using AFP on thermoplastic prepregs. As a direct alternative to the autoclave curing that would follow the layup, each fully impregnated tape can then be melted by a heat source, welded to the layer below, compressed by a roller, and cooled down below melting temperature. If this is done properly, ISC can be achieved, meaning that no additional consolidation process (e.g. autoclave or oven cure) is necessary [51].

OOA processes are starting to appear as state-of-the-art technology in the aerospace industry and may use many different thermal sources such as open flame, hot gas, hot shoe, laser, infrared radiation, etc. [52]. These processing methods are currently only possible using thermoplastic prepregs (as they do not need to chemical cross-link like thermosets), which presumably is one the main reasons for the notable ongoing emergence of thermoplastics in the aerospace industry. Although the raw material costs of aerospace thermoplastics can, in some cases, be higher than competing thermosets, the cost of the finished component can be roughly 20 to 40 percent lower due to reduced handling, processing and assembly costs [46].

In addition to the major advantage of avoiding the use of the cost-intensive autoclave, the ability to co-consolidate complex parts as one provides for a reduction in part count and assembly cost as mechanical fasteners and adhesives are eliminated, which is particularly useful for the skin-stiffener attachment [53]. In fact, OOA methods are a trend being adopted by several of the major players in the aeronautic and aerospace sectors. NASA, for example, is developing their own prepreg-based OOA methods with an eye on its next-generation heavy launch vehicles, since some of their components are extremely large and would not fit inside any existing autoclave [46].

Welding processes (OOA), however, still need further development to reach the highest level of consolidation currently offered by the autoclave processing [52]. This shortfall in the mechanical properties of the welded parts is expected to narrow over time, following the modifications that came, and will continue to come, from researchers' work [52]. Although a final maturity phase is yet to be reached [51], extensive and costly testing and recertification are currently a work in progress to bring these projects from paper to reality. Several large-scale aircraft demonstration projects were already proven to align well with the vision for future aircraft manufacturing, in which automation and thermoplastic composites should be the key drivers.

Recently, other OOA approaches have also been demonstrated, as the novel manufacturing method developed by MTorres at the end of 2017 [54]. The demo piece, illustrated in Figure 6, represents a curved one-piece fuselage, including stiffening roads, frames, and floor, without the use of single fastener; made by automated fibre placement of dry CF tape, then resin infused and oven cured (OOA).

As a conclusion, it is possible to remark that rapid manufacturing of composites is an area of great interest to the aerospace industry. The automation of the manufacturing processes for composites can achieve an increased production rate, reduction in labour costs and improved geometric repeatability when compared to conventional hand layup; while the parallel development of high-performance thermoplastics and new techniques for OOA processing, such as ISC using ATL/AFP, or even RFI or RTM, are expected to be continually optimized and take an even higher process share due to their major cost-savings, despite the required high capital investment [43].

Figure 6 – New fuselage concept manufacturing process developed by MTorres [54].

2.2. Adhesive Bonding

Adhesives have been successfully used for many years in diverse sectors of industry such as aerospace, automotive, biomedical/dental, construction, electronic, marine, etc. [55]. Over the last decades, major developments in the technology of adhesives have been reported, leading to an enormous increase in the mechanical performance of adhesives and adhesive joints, therefore inciting their usage in more technically demanding applications [56]. Particularly in the aerospace industry, adhesive bonding has emerged as a direct alternative to riveting or fastening aircraft primary structures [7].

Adhesion is defined as the attraction between two substances, as a result from intermolecular forces that establish between them [57]. Figure 7 illustrates an adhesive joint, from which different regions can be distinguished. The materials to be bonded are called substrates – or adherends, after being bonded [56]. The region between the adhesive and the adherend is referred to as the interphase, and has different physical and chemical from those of the bulk adhesive or the adherend. If a substance is used on the substrate to improve adhesion or to protect the surfaces, it is referred to as primer [57].

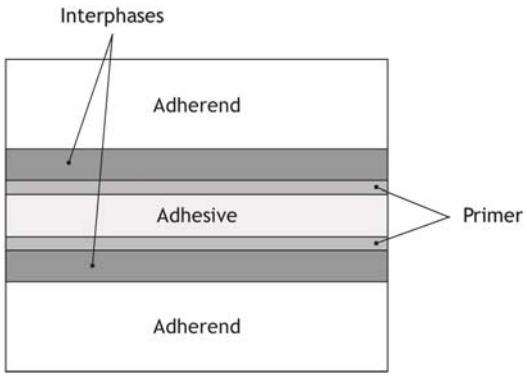

Figure 7 – Adhesive joint. Adapted from [57].

2.2.1. Bonded and Mechanically Fastened Joints

Adhesively bonded joints are an increasingly used alternative to mechanically fastened (riveted or bolted) joints in engineering applications, as they provide many numerous advantages over these methods. Among the most important advantages, it is possible to highlight the more uniform stress distribution along the bonded area, higher stiffness, and enhanced load transmission [57]. Figure 8 illustrates the comparison between the stiffness and stress distribution on riveted and bonded joints. The increase in stiffness and more uniform stress distribution in the bonded stiffened panel is mainly obtained by the higher contact area (and less non-reinforced area).

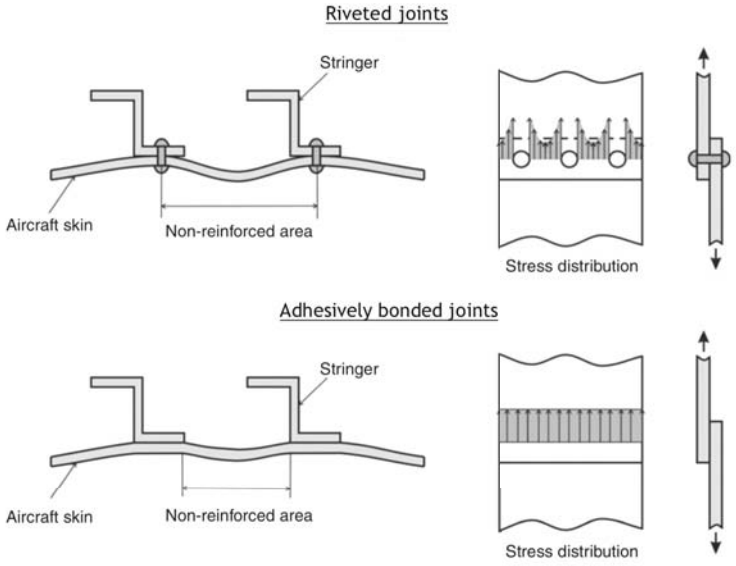

Figure 8 – Improved stiffness (left) and more uniform stress distribution (right) of adhesively-bonded joints compared to riveted joints. Adapted from [57].

The better fatigue resistance of the adhesively bonded joints is, together with the reduced weight, one of the most important advantages in aircraft bonded structures, which are expected to sustain cyclic fatigue loads for considerable periods of time without any adverse effect on the load-bearing capacity of the airframe [8,12].

Mechanical fastening is usually considered to be less costly than adhesive bonding because of its simplicity, low-cost tooling and inspection requirements [12]. However, drilling holes in composites is highly labour intensive, and special care is required to avoid damaging the composite (Figure 9). In addition, bolted structures often need numerous mechanical fasteners with washers/shims to prevent damaging the composite structure during bolt clamp-up. Another disadvantage is that CFRP composites have a high potential for causing galvanic corrosion when used with metallic fasteners and structures [37]. For these reasons, adhesively bonding a structure may in many cases be the more economical option, despite the high tooling and process costs [12].

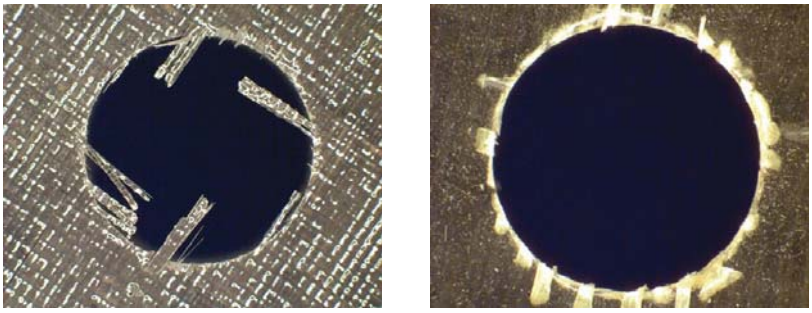

Figure 9 – Damaging of composite's fibres from hole drilling: a) Splintering; b) Delamination [58].

Table 1 lists the main advantages and disadvantages of adhesively bonded and bolted joints.

Table 1 – Advantages and disadvantages of adhesively bonded and bolted joints [12].

Advantages	Disadvantages
Bonded Joints	
Low-stress concentrations in adherends	Difficulty in bonding thick sections
Lightweight	Difficult to inspect and repair
Stiff connection	Prone to environmental degradation
Excellent fatigue life	Sensitive to peel and cleavage stresses
No fretting problems	Cannot be disassembled
Smooth surface contour	High quality control required
Damage tolerant	Difficulties in recycling materials
Bolted Joints	
Easy to disassemble	Considerable stress concentration
No thickness limitations	Added weight of mechanical fasteners
Simple joint configuration	Metallic components are prone to fatigue
Straightforward manufacturing and inspection	Hole formation can damage the composite
Environmentally insensitive	Composites have poor bearing properties
Insensitive to peel forces	Fretting problems in metals
Residual stresses are generally not a problem	Extensive shimming is often required for composites

Chowdhury et. al. [59] have performed an extensive investigation to compare riveted, bonded and hybrid (mixing adhesive and rivets) composite lap joints. The authors reached the conclusion that riveted lap joints exhibit the lowest static and fatigue performance, whilst the hybrid solution performed the best, mixing together the advantages of bonding and riveting.

The hybrid solution arrested rapid crack growth and prevented sudden catastrophic failure [2], however, it may not be considered ideal from an assembly point of view since it constrains many of the advantages of the two joining methods. Particularly when using composite materials, the fact that adhesive bonding preserves the integrity of the parent material is one of the major reasons for its preference over the mechanical methods.

To sum up, it is possible to say that the choice of the joining technique is dependent on several factors (materials to be joined, durability, load transfer paths, etc.), but the many advantages offered by adhesive bonding justify the attention paid by scientists to increase the strength of the adhesive itself – which is still limited and not completely suitable for highly stressed structural parts [2] – and the reliability in adhesive joints by developing new design and predictive methodologies [12].

2.2.2. Applications in the Aerospace Industry

Adhesive bonding has been used in the manufacture of primary aircraft structures, such as the fuselage and wings, for over 70 years [7]. The very first adhesives used in aircraft structures emerged from synthetic polymers used in advanced technological applications, which were developed during the mid-1940s and were capable to transmit considerable loads [57]. Since then, the aeronautical industry is considered one of the main precursors of the adhesive bonding technology and increasingly uses adhesives as more composites are introduced in aircraft [57].

De Havilland and Fokker industries were the pioneers in using adhesive bonding in aircraft structures. De Havilland Dove (1945) and the Fokker F27 Friendship (1955) aircraft are renowned for their successful widespread use of adhesive bonding using the Redux 775 phenolic adhesive [7]. A few years later, other manufacturers started to use epoxy adhesives on their aircraft, such as the Boeing 727 (1963) which used the Cytec FM1000 hot cured epoxy adhesive.

More recently, and with the increased usage of composites materials in aircraft structures, manufacturers have started to extensively use adhesives for primary parts of aircraft [12]. Nevertheless, adhesive bonding is still mostly used for secondary (not main load-bearing) structures [12], such as bonding of stiffeners/stringers to skins for both fuselage and wing construction (which is the very subject of this project) and of metallic honeycomb to skins for elevators, ailerons, tabs and spoilers [2,7].

2.2.3. Adhesives and Structural Adhesives

According to Kinloch [56], an adhesive may be defined as a material which, when applied to surfaces of materials, can join them together and resist separation.

Two main types of adhesives can be distinguished: structural and non-structural adhesives. According to Adams and Wake [60], a structural adhesive is an adhesive which can resist substantial loads and is responsible for the strength and stiffness of the structure. Its shear strength can vary from 5 MPa for a polyurethane to 50 MPa for an epoxy [57]. Non-structural adhesives, on the other hand, are not required to support substantial loads, and can be applied on lightly loaded structures for positioning or sealing purposes, for example.

Adhesives can also be classified by the nature of their base polymer, which may be natural or synthetic. According to their chemical composition, they can be either thermosets, thermoplastic, elastomeric, or a mixture of these (hybrid). In terms of the chemical family, adhesives used in structural applications include epoxies, cyanoacrylates, anaerobics, acrylics, polyurethanes, silicones, and high-temperature adhesives (phenolics, polyimides, and bismaleimides) – and whose typical properties are presented in the Annex A. Epoxy adhesives are very frequently used to bond composites based on epoxy matrix because of the very good compatibility between the resin and adhesive [8].

Table 2 lists some typical mechanical properties values for different types of adhesives [8].

Table 2 – Typical adhesives' mechanical properties values [8].

Adhesive	Type	Shear modulus (MPa)	Shear strength (MPa)	Shear strain (%)
AV138	Epoxy	1559	30	7.8
DP805	Acrylic	159	8.4	180
SikaFlex 265	Polyurethane	0.7	4.5	450
RTV 106	Silicone	-	1.3	400
AS1805	Silicone	0.68	1.47	330
Redux 326	Bismaleimide	1180	36.5	3.63

Adhesives can be supplied in the form of a paste or a film. For aerospace applications, film adhesives are typically used. Films often carry some support material (polyester, nylon, or glass fibres) that is embedded in the adhesive with the purpose of improving handling of the films prior to cure, preventing adhesive bleeding during cure, and controling the bondline thickness. In terms of composition, rubber-toughened epoxy adhesives are among the most widely used in the aircraft industry [37].

Alternatively, paste adhesives are used to secondary bond repair patches to damaged parts, and also in places where film adhesives are difficult to apply. Some advantages of paste adhesives are that they can be stored at room temperature and have a long shelf life. The main disadvantage is that the bondline thickness is difficult to control, affecting the strength of the bonded joint [37].

Recent trends in the development of new adhesives include smart adhesive materials such as self-healing or disbond adhesive materials. Reuse, recycling and recovery of bonded parts are one of the major concerns of the industry, to which bio-adhesives can be a viable solution [9].

In conclusion, the selection of the adhesive material for a specific application depends on many factors such as the type of adherend to be bonded, curing temperature, expected environmental condition during service, type of load, cost, etc. [9]. Special attention should be paid when exposing the adhesive systems to harsh environments, which can considerably deteriorate their performance [8].

2.2.4. Loading Modes

Although the loading scenarios in adhesively bonded joints can be extremely different, it is possible to identify five pure loading modes that can be found in adhesive joints:

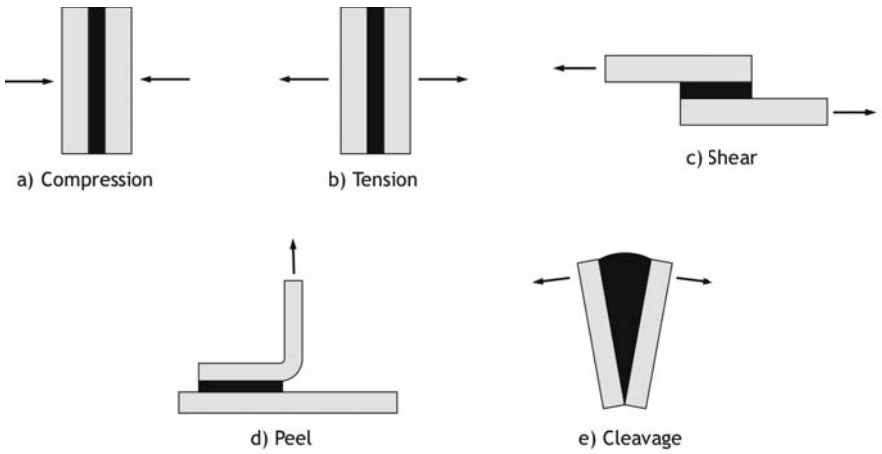

Figure 10 – Loading modes in adhesively bonded joints.

a) **Compression** loads are uncommon and sometimes unconsidered, due to the fact that under a pure compression load the joint will very unlikely fail [61].

b) **Tensile** loads are developed when forces act perpendicularly to the plane of the joint and are distributed uniformly over the entire area of the bond. This loading distribution promotes a good joint strength with respect to the bonded area. However, in real applications, due to

deflection of the adherends and difficulty to guarantee the exact thickness of the adhesive layer and the alignment of the bonded parts, loads rarely are purely axial, and peel or cleavage stresses may occur, making the joint more likely to fail [62].

c) **Shear** loads act in the plane of the adhesive and promote sliding between the adherends. This loading mode uses the joint area to the best advantage, giving an economical joint that is most resistant to joint failure – for that reason, and whenever possible, most of the load should be transmitted as a shear load [61,62]. Nevertheless, in real applications stress, peaks occur at the edges of the overlap (primarily due to load misalignment [57]), as illustrated in Figure 11a.

d) **Peel** loads try to split flexible adherends (at least one is flexible) apart at one end of the bonded assembly, which originates high stress concentrations at the loaded overlap edges, as illustrated in Figure 11b. This offers lower strength than joints loaded in shear because stresses are concentrated in a small area of the total bond, therefore, unless the joint is wide or the load is small, failure of the bond will occur. This type of loading is to be avoided if possible [61].

e) **Cleavage** loads occur when forces at one end of a bonded assembly act to split rigid adherends apart. In joints under a cleavage load, similar to peel, stresses are not evenly distributed along the adhesive layer, but instead are concentrated at one side of the joint. A sufficiently large area is needed to accommodate this stress, resulting in a costlier joint [61]. Both cleavage and peel stresses are undesirable for adhesive bonding.

Figure 11 – Stress distribution along a SLJ: a) Adhesive shear stress; b) Adhesive peel stress [57].

As it was mentioned, joints which are only subjected to shear forces can sustain a greater load and have a greater strength than with any other loading modes. On the contrary, cleavage and peeling forces are not advisable for the joint strength due to the small area that is actively resisting to the load. However, under real loading situations, neither of these pure loading modes is observed, but rather a combination of them [61].

2.2.5. Joint's Configurations

As presented by Adams and Wake [60], a wide variety of adhesively bonded joints configurations are available to meet specific engineering applications. Some examples of the most frequently used joints, and which have been thoroughly analysed in the literature, are single-lap joints, double-lap joints, and scarf joints. These, and some other typical joint configurations, are illustrated in Figure 12.

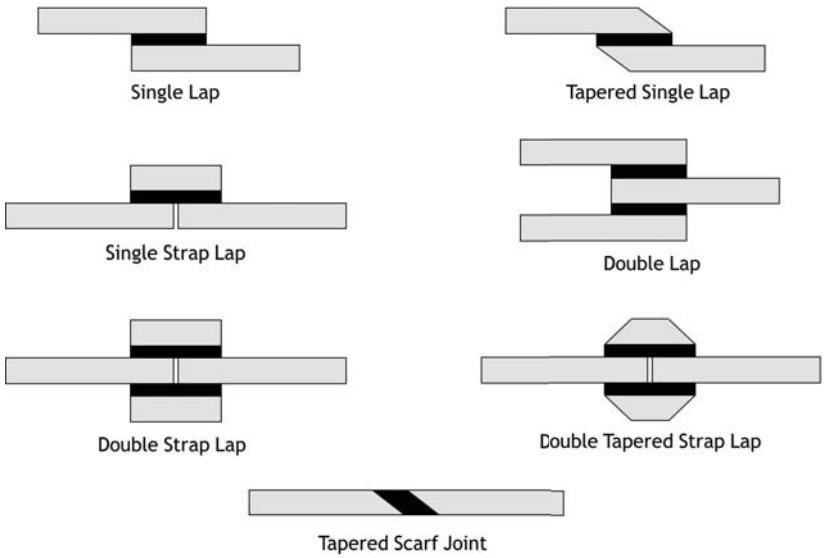

Figure 12 – Examples of adhesively bonded joints configurations.

Chamis and Murthy [63] described a step-by-step procedure for the preliminary design of composite adhesive joints, for use in hot/wet service environments, under static and cyclic loads. One of the most important things to consider when designing an adhesive bonded joint is that it should be done in a way that minimizes stress concentrations [61]; and some stresses, such as peel and cleavage, should be minimized, while others maximized, such as shear and compressive stresses [8].

It has also been found that attention should be given to the design of the shape of the ends of the joint's overlap, where shear and peel stresses tend to be maximum. For example, controlling the shape of the adhesive overflow by creating a spew fillet (Figure 13) may greatly reduce the adhesive shear and peel stress concentrations, resulting in an increase in the joint strength [47].

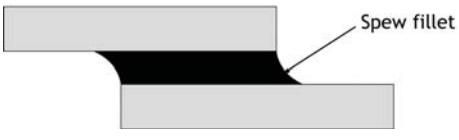

Figure 13 – Spew fillet.

2.2.6. Failure Modes

According to the standard ASTM D 5573-99 [64], there are seven classes of failure modes that can occur in adhesively bonded fibre-reinforced plastic (FRP) joints. These are illustrated in Figure 14.

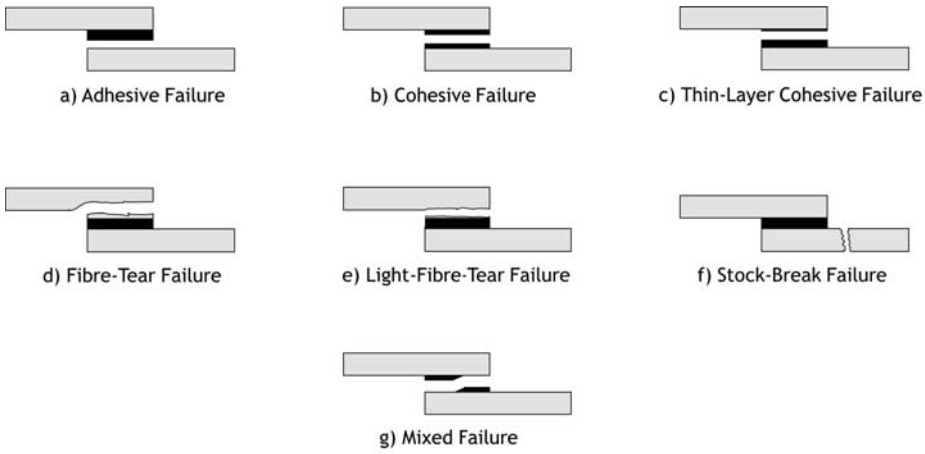

Figure 14 – Classes of failure modes on FRP joints.

a) **Adhesive failure** (AF) (sometimes referred to as interfacial failure) occurs between the adhesive and one of the adherends, leading to complete separation at the adhesive-adherend interface. Visually, one of the adherends has no adhesive, while the other adherend has the entire layer of adhesive attached to it. This failure mode may result from a bad surface preparation or a bad choice of adhesive.

b) **Cohesive failure** (CF) occurs when the bonding strength between the adherend and the adhesive is higher than the strength of the adhesive. In this failure mode the separation is within the adhesive and both failure surfaces have a thin layer of adhesive.

c) **Thin-layer cohesive failure** (TLCF) (sometimes referred to as interphase failure) is similar to cohesive failure, except that the failure is very close to the adhesive-adherend interface, and is characterized by a light dusting of adhesive on one adherend's surface and a thick layer of adhesive left on the other.

d) **Fibre-tear failure** (FTF) occurs exclusively within the fibre-reinforced plastic (FRP) matrix and is characterized by the appearance of reinforcing fibres on both ruptured surfaces.

e) **Light-fibre-tear failure** (LFTF) occurs within the FRP adherend, near the surface, and is characterized by a thin layer of FRP resin matrix visible on the adhesive, with few or no fibres transferred from the adherend to the adhesive.

f) **Stock-break failure** (SBF) occurs when the separation is within the adherend but outside the bonded region.

g) **Mixed failure** (MF) is a combination of different classes (e.g. adhesive and cohesive failures). This may happen because of a non-uniform cleaning in the adherend's surfaces, or due to some areas with bad adhesion.

Failure modes are determined by the quality of the bond at each interface, specimen geometry, and loading [8]; and for that reason a good post-failure analysis is crucial to determine the failure mode of the joint in order to being able to further optimize its design, fabrication or curing procedure of the adhesive, for example.

Furthermore, when studying the crack propagation in adhesively bonded joints, it is important to distinguish the three ways of applying a force to enable a crack to propagate, which according to the fracture mechanics are [65]:

- Mode I fracture – opening mode (a tensile stress normal to the plane of the crack);
- Mode II fracture – sliding mode (a shear stress acting parallel to the plane of the crack and perpendicular to the crack front);
- Mode III fracture – tearing mode (a shear stress acting parallel to the plane of the crack and parallel to the crack front).

These three different crack loading modes are illustrated in Figure 15.

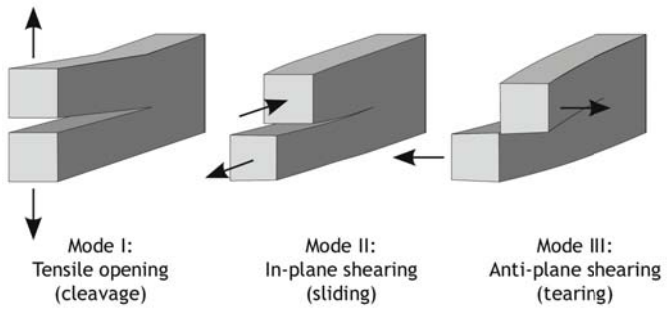

Figure 15 – Three standard loading modes of a crack according to the fracture mechanics [66].

Any loading combination of two or more of these modes is named mixed-mode loading [66].

2.2.7. Parameters Affecting Bonded Joints' Performance

There are a great number of parameters that affect the performance of bonded joints, as surface preparation, joint configuration, bonding method, failure mode, geometrical and material parameters, etc. [9]. The environmental factors such as pre-bond moisture, moisture, and temperature, can also greatly affect the durability of adhesive joints. Therefore, all these parameters must be taken into account during the design and fabrication of bonded joints in order to achieve a good performance of the final bonded structure. In fact, most adhesive bond failures can be attributed to poor processes during fabrication, with poor quality surface preparation being the most significant deficiency [67].

Along this subsection and considering the purpose of this project, three different parameters will be a subject of a deeper study: the bonding manufacturing process, surface preparation, and the adhesive bondline.

2.2.7.1. Bonding Manufacturing Process

There are mainly four manufacturing bonding processes to manufacture bonded joints using composite substrates: co-curing, co-bonding, secondary bonding, and multi-material bonding. A scheme of each of these manufacturing processes is illustrated in Figure 16.

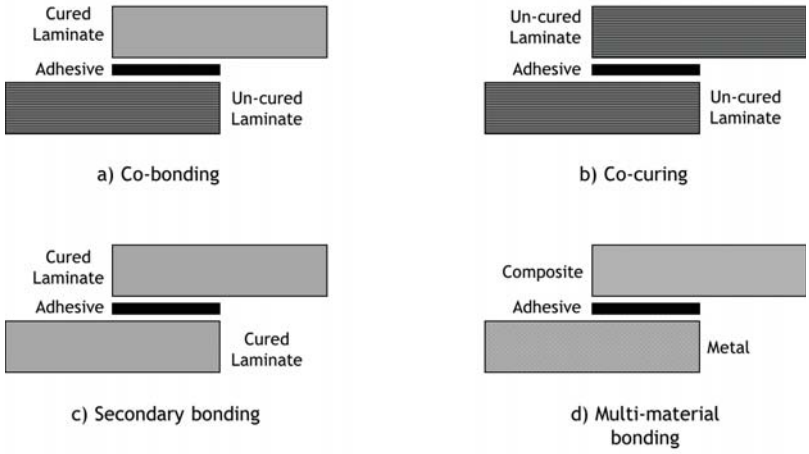

Figure 16 – Different manufacturing bonding processes. Adapted from [9].

The **co-bonding** process is performed when one substrate is cured with the adhesive (the other substrate is already pre-cured), while in the **co-curing** process both substrates are simultaneously cured. An adhesive is often used to improve the peel strength (although it is not obligatory for the co-curing process) [37].

Differently, **secondary bonding** consists in curing the adhesive between two previously cured composite substrates [37].

Another process, referred to as **multi-material bonding**, follow a similar procedure to the secondary bonding, but uses a combination of metal and composite substrates instead of only composite substrates [9].

The co-curing and co-bonding processes are usually preferred over the secondary bonding because the number of parts and cure cycles are reduced, and for that reason they are commonly used for repairing composite structures [9]. However, for large and complex structures – which imply dimensional limitations – the secondary bonding process is sometimes more suitable.

The influence of the bonding method on the performance of the joint has been investigated by several authors. Mohan et al. [68] found out that the co-cured bonded joints exhibited lower strength than the secondary bonded joints in both mode I and mixed-mode loading. Song et al. [69] also noticed the same trend in the strength of single lap joints (co-cured without adhesive > secondary bonded > co-cured with adhesive > co-bonded). This has to do with the fact that the moisture present in the composite was released during cure and spread out in the adhesive layer, weakening the interface and causing a lower strength of the co-cured and co-bonded joints [9].

2.2.7.2. Surface Preparation

The success of a bonded joint strongly depends on the surface treatment of the adherends, as it is the most important process governing the quality of an adhesive bond [8,12,67].

Surface pretreatments are carried out to achieve one or more of the following:

- To remove completely, or to prevent formation of, weak boundary layers;
- Optimise the degree of contact between the adhesive and adherends, using chemical or physical modifications of the substrate surfaces;
- To protect the adherend's surfaces before bonding. Although composite substrates are not very reactive with atmospheric contaminants (unlike metals), there is a wide range of contaminants resulting from manufacturing and handling the composite that could by their nature form a weak boundary layer and reduce the bonding strength.

The type of pretreatment is often a compromise between the best surface preparation, economics of component manufacture, and health and safety issues [55].

Table 3 illustrates the most often used surface pretreatments for adhesive bonding.

Table 3 – Surface pretreatments for adherends [70].

Mechanical	Chemical	Energetic
Alumina gritblast	Solvent cleaning	Plasma
Cryoblast	Detergent wash	Corona discharge
Sodablast	Acid etch	Flame
Peel ply	Anodising	Excimer laser
Silicon carbide abrasion	Primer	

Prior to adhesive bonding, it is necessary to ensure the removal of all contaminants (lubricants, dust, loose corrosion layers, micro-organisms) from the substrates' surfaces, but also good surface wettability, high surface energy, good activation of material surfaces being bonded, etc. [9]. This is particularly important for composite materials, since the primary aim of the surface treatment is to increase the surface free energy value (SFEV) of the adherends as much as possible (necessarily higher than the surface tension value, STV, of the adhesive) [71]. While most metals and ceramics have a fairly high surface energy, plastic composites do not, and thus require a technique that shears the top layer of molecules on the composite matrix surface, this way creating many broken atomic bonds without damaging underlying fibres.

There are two main easy and accessible techniques used when preparing composite substrates for adhesive bonding: the peel ply method, typically using polyamide (nylon) or polyester fabrics; and silicon carbide abrasion followed by solvent cleaning. The abrasion method is often conducted after a peel ply surface has been exposed [47].

Peel ply is a woven synthetic fabric which is added as the last layer in the layup and cured to the composite part to be bonded. It is then removed just prior to bonding, exposing, in principle, a clean, activated, and bondable surface. However, it has been noticed that the composite matrix resin interacts with the peel ply material and that interphase or residues of the peel ply are left on the composite surface [9], as illustrated in Figure 17.

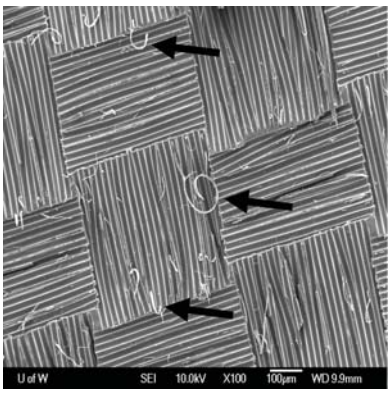

Figure 17 – SEM micrograph showing tendrils of polyester peel ply fibres left after removal of a dry peel ply before bonding [71].

To overcome this problem, it is either necessary to use a peel ply which does not leave contaminants behind, or to eliminate the residual contamination. This latter route has been the one typically followed in many industries, by abrading the surfaces after peel ply removal, followed by a solvent wipe to remove the abrasion products. The peel ply is useful for protecting the surface from any contamination before bonding, and after removed, light scuff sanding eliminates the high resin peak impressions produced by the peel ply weave (which, if they fracture, create cracks in the bondline [37]). This has been demonstrated to be one of most cost-effective techniques for surface preparation of composite substrates [47], effectively increasing the strength of the joint (in terms of shear strength or fracture toughness) when compared to a joint only pre-treated with a peel ply [47,72]. However, mechanical abrasion causes visible damage to the composite's fibres, negatively affecting the bulk mechanical properties of the adherends [70].

Other alternative surface treatments include plasma, laser, corona discharge and blasting treatments, for example. These techniques are among the most effective bonding pretreatments for composites, particularly thermoplastics [70], but have the main disadvantage of high acquisition and operating costs [9].

The water contact angle (WCA) is a commonly used non-destructive test (NDT) for predicting the surface energy of the substrate via the Young's equation for surface wetting. According to Young's equation, there is a relationship between the contact angle θ, the surface tension of the liquid γ_{LG}, the interfacial tension γ_{SL} between liquid and solid and the surface free energy of the solid γ_{SG}:

$$\gamma_{SG} = \gamma_{SL} + \gamma_{LG} \cdot \cos\theta$$

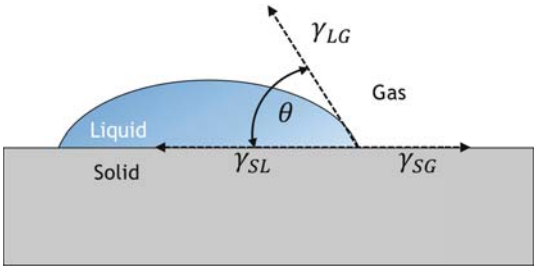

Figure 18 – Schematic diagram of the components of the three-phase system relevant for wetting.

To determine the degree of wetting, the contact angle (θ) that is formed between the liquid and the solid surface is measured, and the surface free energy values (SFEV) of the solid can be obtained using different surface energy models. One of the most used methods is the Owen-Wendt (OW) two liquid model – one polar and one nonpolar test liquids – which allows for dissociation of the total surface energy into polar and nonpolar (dispersive) components [73].

The results of contact angle measurements can be translated into surface free energy values, and an increase in the surface free energy, for one, can be interpreted as an improved wetting characteristic [72]. Wetting is the ability of liquids to form interfaces with solid surfaces. As illustrated in Figure 19, the smaller the contact angle and the smaller the surface tension, the greater the degree of wetting, and presumably the better the quality of the adhesive bonding.

Figure 19 – Different degrees of surface wetting: a) Poor wetting; b) Good wetting.

2.2.7.3. Adhesive Bondline

The effect of the adhesive thickness on bonded joints was studied by several authors using analytical, numerical and experimental methods in several joint configurations. However, most of the research was performed on single lap joints (SLJs) under tensile shear tests.

For SLJs, some authors concluded that strength decreases as the adhesive thickness increases, except for SLJs bonded with elastomeric adhesives. This was attributed to the fact that the thicker bondline contained more defects such as voids, micro-cracks and higher interface stresses [9]. Arenas et. al. [74] performed a statistical evaluation on tensile single lap shear tests based on the Weibull distribution and concluded that the optimum adhesive thickness in structural adhesives was about 0.5 mm.

Other authors have found that the fracture energy of the joint increases as the adhesive thickness increases for a ductile adhesive, but for a brittle adhesive it is the opposite. It was also found, using numerical simulations, that the ductility of the adhesive increases as the adhesive thickness is increased [9]. This results in a more compliant joint to shear stresses, as the extra adhesive thickness distributes the shear strain over a larger dimension, lowering the strain per unit length and the stress concentration at the ends of the bondline [55].

It is possible to conclude that there is no generalized correlation between the joint strength and adhesive thickness, and this unpredictable behaviour may be attributed to various factors such as the type of loading (mode I, mode II, or mixed), adherend behaviour (elastic or plastic), type of adhesive (ductile or brittle), geometry of joints, etc. [9]. Moreover, most of the work was performed under mode I and mode II loading conditions, and there is limited research regarding the effect of bondline thickness under mixed-mode loading [9].

Another important factor to consider during the fabrication of adhesively bonded joints is to maintain a constant and uniform bondline thickness. Figure 20 illustrates the unequal stress

distribution at a single lap joint with an unevenly bondline thickness, causing a reduction of the bonding strength.

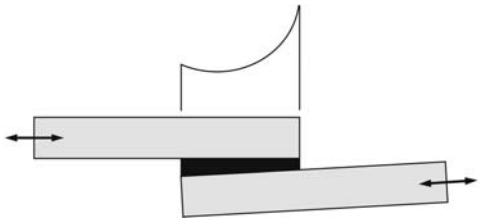

Figure 20 – Unequal stress distribution through an unevenly bonded joint. Adapted from [75].

As mentioned in the subsection 2.2.3, bondline thickness uniformity is often achieved by embedding a textile membrane in the adhesive film (i.e. carrier).

2.3. Skin-to-Stiffener Joints

The skin-to-stiffener joint is a particular example of a T-joint, and a typical case of adhesively bonded aircraft structures, with stiffeners (or stringers) being longitudinally bonded to skins for both fuselage (Figure 21a) and wing (Figure 21b) construction [2,7].

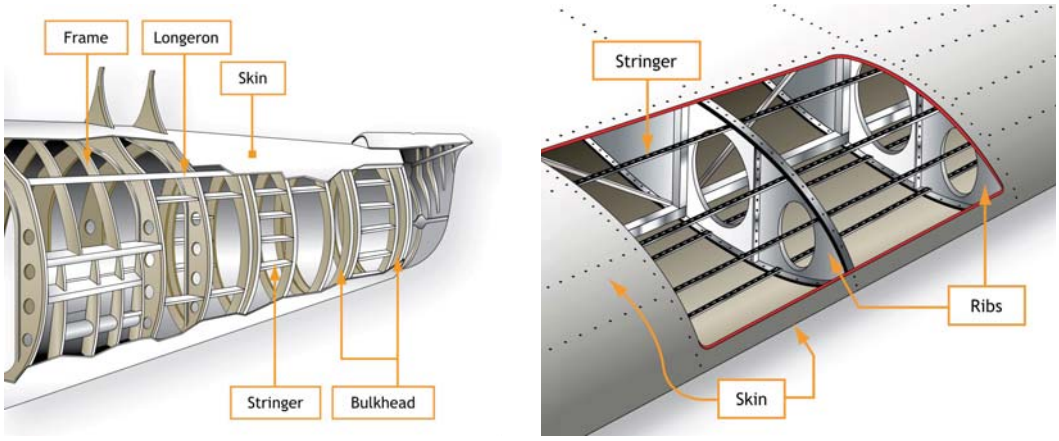

Figure 21 – Semi-monocoque aircraft structure: a) Fuselage; b) Wing. Adapted from [76].

Stiffeners are generally designed to primarily take axial (longitudinal loads), preventing tension and compression stresses from bending the fuselage or wings' skin. They act as stiffening elements of the skin, and introduce multiple load paths which may provide protection against damage and crack growth. The biggest advantage of using stiffeners is the increased bending stiffness of the structure with a minimal addition of material, which makes these structures highly desirable for destabilizing compressive loads and out-of-plane loads [77,78]. Furthermore, the use of composites makes it possible to further tailor the stiffness and strength

characteristics of the individual elements (such as the web, noodle, flanges) of a stiffened skin to meet different structural requirements [78].

One of the very first reports on the analysis of the mechanical behaviour of stiffened panels was presented in 1962 by Boeing [79], and consisted on the estimation of the stresses' distribution in skin-stiffener type continuous panels under random loading.

In 1984, NASA [80] described in detail an analysis procedure for determining the stresses in the interface layer between the skin and the attached flange of stiffened composite panels.

During the last decades, most of the researchers have been focused on studying the debonding of the skin-to-stiffener joint, particularly under out-of-plane (normal) loadings. Evaluation is often carried using stiffener pull-off tests (SPOTs), either by experimental testing or using analytical or numerical methods.

Due to the emergence of composite materials in aircraft construction and their unpredictable behaviour when compared to traditional metals, most of the recent research was performed on CFRP specimens. Several authors have studied different design concepts and structural features of these CFRP T-joints using SPOTs [1,3,15-32], from which some examples can be highlighted:

Huang [21] studied the influence of the stiffener radius and concluded that when the stiffener radius was larger than 9 mm, there were some very twisted fibres at the intersection (Figure 22) of the web and skin – the noodle, also referred to as delta-fillet – reducing the strength of the joint. This was attributed to the fact that the laminate with larger radius had difficulty to conform to the contour of the tool, causing the plies to bridge across the corner area during bagging and curing.

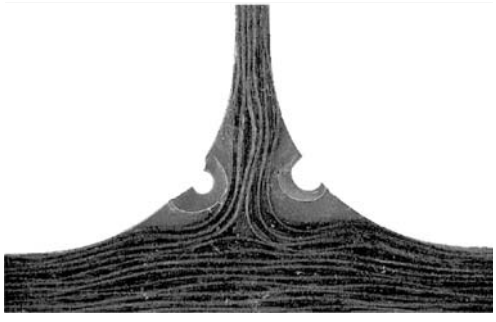

Figure 22 – Twisted fibres and excess resin distributed in a 9 mm corner [21].

Huang [21] concluded that the optimum radius ranged from 3 to 6 mm, but higher joint strengths could be achieved by eliminating the manufacturing problem of the fibre twisting. Huang also concluded that a flange length of 15 mm was sufficient to create a strong structure, and a greater flange length would not necessarily increase the strength of the joint.

Other manufacturers chose to fill the gap between the radius bends with adhesive, foam, or a triangular noodle formed with unidirectional prepregged fibres, to ensure the smooth formation of the overlaminate to support load transfer between the orthogonal panels [81]. The influence of the area and quality of the noodle has also been investigated by Kumari et al. [82] and Trask et al. [25].

Freitas et. al. [1] compared the performance of hybrid (metal/CFRP) skin-to-stiffener joints with metal (metal/metal) skin-to-stiffener joints, and concluded that due to unstable delamination in the noodle of the CFRP stiffener, metal joints performed better than the hybrid joints. In a later work, Freitas et. al [3] also studied the influence of temperature in similar hybrid joints, and concluded that the increase of ductility of the composite epoxy resin (provided by the increase in temperature) causes a decrease of stress concentrations at the stiffener, resulting in better performance of the bonded joint in terms of maximum load.

Burns et. al. [15] used the biological principle of hierarchical (multi-scale level) design of tree branch joints to design a novel carbon/epoxy T-joint, resulting in a significantly improved tensile strength compared to a conventionally designed T-joint.

Other researchers have focused their attention in the study of these joints using Finite Element Analysis (FEA), e.g. as performed by Carneiro et. al. [16] using Cohesive Zone Models (CZM), or using the Virtual Crack Closure Technique (VCCT) [83].

In the subject of health monitoring of these joints, Ma et. al. [22] implemented an experimental setup for the detection of interface debond of CFRP T-joints using piezoelectric sensors. Other methods have been also presented, such as a vibration based damage identification algorithm using finite element models [84].

Several articles have been published on the improvement of the through-thickness strength of skin-to-stiffener joints using 3D reinforcement techniques such as “z-pinning”, “weaving”, “stitching”, and “tufting” [18]. All of these techniques consist in some kind of through-thickness reinforcement, such as carbon pins. It was discovered that these methods were effective on stopping delamination between the skin and the stiffener [27], but such benefits were only possible by sacrificing in-plane strength/elastic properties of the laminates [85]. Furthermore, these techniques are often considered unsuitable for reinforcing uncured prepreg laminates and to assembly CFRP parts [33], and for that reason, only a few composite components containing 3D reinforcements are currently in service in the aerospace industry [27]. Silva et. al. [85] performed a brief review on some of the most relevant through-thickness reinforcement technologies for CFRP/Metal and CFRP/CFRP joints.

Chapter 3 – Experimental Procedure

In this chapter, the materials and methods used during the experimental procedure will be described, including the fabrication and mechanical characterization of the bulk adhesive. The geometry and dimensions of the specimens will be properly presented, along with the process carried out to fabricate them. Subsequently, the experimental methodology will be exposed for the two types of performed tests (tensile single lap shear and stiffener pull-off tests), following an order that may not seem ideal from a planning point-of-view, but represents the chronological order of events – which were decided throughout the course of the project based on the previous results.

3.1. Experimental Setup

3.1.1. Materials

3.1.1.1. Adherends

The adherends' material consisted of a modified epoxy resin reinforced with high strength carbon fibres (prepreg) in the form of a unidirectional tape (0.164 mm thick), being its commercial name SEAL® Texipreg HS 160 REM [86]. According to the manufacturer's data, the maximum glass transition temperature (T_g) of the REM epoxy matrix is 125 °C, which is the temperature recommended for its cure cycle.

The mechanical properties of the prepreg laminate were already defined by the manufacturer and are presented in Table 4, according to the information on the technical data sheet (TDS) [87].

As stated in the literature review, prepregs have become the most often used material in the aerospace industry, and this prepreg in particular is often used by aircraft manufacturers as primary airframe material. It is aimed, this way, that the final specimens will represent as reliably as possible the mechanical properties of similar aircraft structures.

The number of layers and their orientation will vary according to the type of test, and for that reason they will be mentioned in detail in the next subsection (3.1.2).

Table 4 – Mechanical properties of the HS160 T700 REM UD tape 36% [87].

Cured Material Property	Unit	Actual Values
Tensile Modulus 0°	GPa	123.0
Tensile Strength 0°	MPa	2294
Tensile Strain	%	1.72
Compression Modulus 0°	GPa	109.8
Compression Strength 0°	MPa	1152
Flexural Modulus 0°	GPa	134.0
Flexural Strength 0°	MPa	1850
Inter-laminar Shear Strength	MPa	81.5
Cured Ply Thickness	mm	0.164

3.1.1.2. Adhesive

The adhesive chosen was a structural epoxy adhesive film, SEAL® EA451 U150 (unsupported). It is compatible with the HS 160 REM prepreg and was designed for co-curing or secondary bonding of composite substrates, including honeycomb and foam sandwich panels. Such as the prepreg, this structural adhesive is used in the aerospace industry for bonding aircraft composite structures.

According to the manufacturer's data, the maximum glass transition temperature (T_g) of the adhesive is 190 °C, and it can be cured within a range of curing temperatures from 90 °C to 180 °C. Table 5 shortly presents the properties of this adhesive after co-curing, as indicated in the adhesive's TDS [88].

Table 5 – Adhesive performance values for honeycomb co-cured composite under climbing drum peel testing [88].

Cured Material Property	Test Method	Adhesive	Value (Torque)	Units
Honeycomb Climbing Drum Peel	ASTM D1781-98 (R04)	EA451 K185	60.8	Nm/m
Honeycomb Climbing Drum Peel	ASTM D1781-98 (R04)	EA451 K300	81.1	Nm/m

Unfortunately, these values correspond to tests performed on slightly different adhesives (both EA451 K185 and EA451 K300 carry a supporting knit and have higher weight gsm), and provide very limited information, without any indication of the bulk adhesive properties. Hence, it was necessary to characterize the bulk adhesive behaviour with the purpose of obtaining some of its mechanical properties, particularly the stress-strain curve and the Young's modulus. These values are not only crucial to understand the behaviour of the bonded joints at different scenarios, but also indispensable to posteriorly perform any kind of strength prediction through numerical simulations.

From the literature [89], it was found that the best practice would be to manufacture bulk specimens and test them using tensile tests. Therefore, a flat sheet of adhesive was produced from which the bulk testing specimens were cut. This was made by stacking eight 194 × 290 mm layers of adhesive film (about 0.1 mm thick each) on top of a metal tool covered with Teflon® for posterior releasing and inside a rectangular metal frame (5 mm thick) that was used for stopping the adhesive to flow out during its cure, as illustrated in Figure 23. The layers were stacked up applying hand pressure after each one, while taking care not to contaminate the adhesive with skin oil or other substances. Stacking the first layer of adhesive film was an especially difficult procedure, due to lack of tack between the adhesive and the Teflon®. Following this observation, in order to make the placement of the first layer easier, the adhesive was placed shortly after taking it out from the freezer so that it was in a more brittle state.

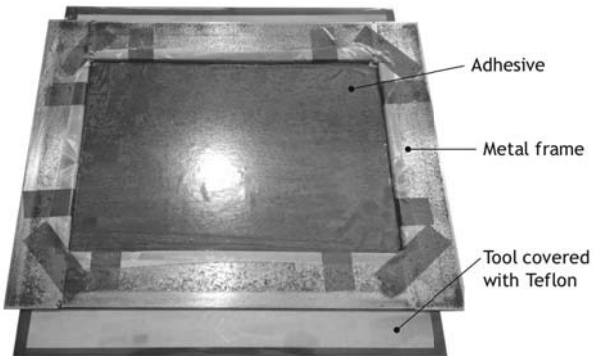

Figure 23 – Setup used to cure the bulk adhesive.

The final "laminate" was cured inside the autoclave following the manufacturer's instructions, using a cure cycle at 125 °C for one hour. When completed its cure, the bulk adhesive plate was removed from the tool without major difficulties by virtue of using the Teflon® sheet.

After inspecting the plate, it was clearly seen that there was a large number of voids entrapped in the adhesive – especially at the upper surface – as shown in Figure 24.

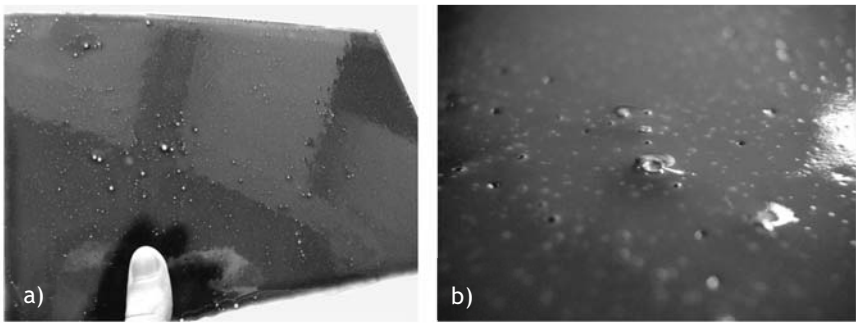

Figure 24 – Cured bulk plate of EA451 U150 film adhesive: a) Void distribution in the overall plate; b) Close-up photography of the voids at the upper surface.

This formation of voids is a known problem associated to adhesive films, as studied by several authors [90-93], and can lead to premature failure of the adhesive joint. According to Bascom [90], the sequence of events that takes place during the cure of the adhesive is as illustrated in Figure 25:

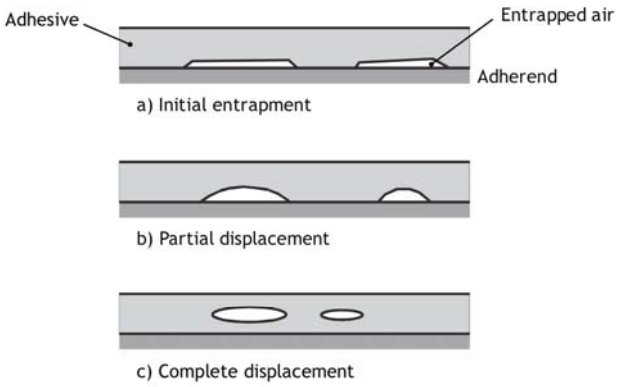

Figure 25 – Air entrapment and displacement process between an adherend and the adhesive film [91].

L.F.M. da Silva et al. [91] noticed that the origin of the voids appears to be not only the air trapped between the film and the adherend, but also air or other gases (steam, solvents, etc.) entrapped in the resin (adhesive), whether this is in the form of a film or paste.

Consequently, it was necessary to find a manufacturing procedure that lets the air and other gases escape, this way minimizing the number of voids in the adhesive. Several techniques are suggested in the literature to minimise this problem, such as the "vacuum release" technique by Bascom and Cottington [92]; and the technique suggested by Patrick which uses hydrostatic pressure in an autoclave [94]. The first technique consists in increasing the temperature to a point at which the adhesive is most fluid such that, when the vacuum is released, the voids collapse to a negligible volume; while the latter considers that the higher the hydrostatic pressure, the more the gas in each void is pressurised and its volume reduced [91]. Bascom and

Cottington [92] found that an increase in bond strength of as much as 30% can be obtained by complete void removal using the vacuum release technique.

Considering the findings made by L.F.M. da Silva et al. while producing similar bulk specimens of paste and film adhesives [91], it was decided to perform a modified version of the "vacuum release" technique. The revised procedure consisted in increasing the temperature up to 120 °C inside the autoclave, while applying vacuum, and maintaining these conditions for 90 minutes. During this increased time, at the temperature in which the adhesive is at its most fluid state (Figure 26), it was expected that most of the air and gases would escape from it. Moreover, after this time the vacuum was released, hopefully collapsing the voids; followed by the application of 1 bar of (relative) pressure to compress the remaining voids and create a good surface finish. According to L.F.M. da Silva et. at. [91], a higher pressure would not necessarily lead to any additional benefits since it would probably not be translated into hydraulic pressure in the (liquid) adhesive, but rather flowing out the adhesive outside the frame (which is not perfectly sealed). From that point, the temperature and pressure were remained constant at 120 °C/1 bar for 30 more minutes, and then the adhesive was left to cool down to room temperature inside the autoclave. Finally, the pressure was re-established to 0 bar and the cured plate was removed from the tool.

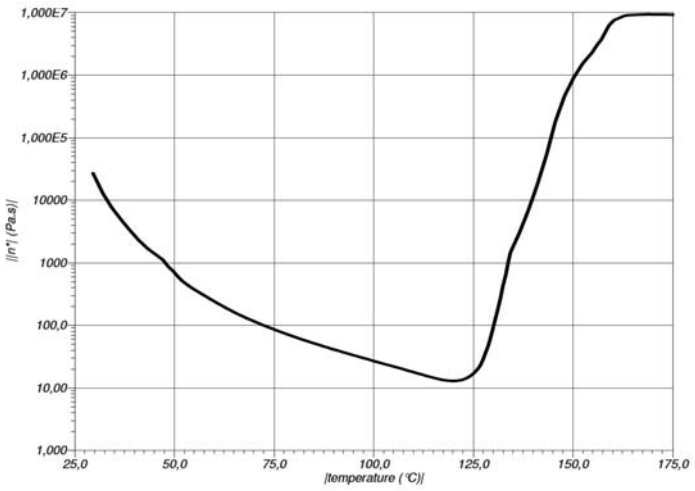

Figure 26 – Viscosity profile of the EA451 adhesive film: temperature vs complex viscosity. Data obtained from the TDS [88].

Besides the new established curing procedure, the number of adhesive layers was increased from 8 to 20. This is estimated to result in a cured plate about 2 mm thick, from which more robust specimens could be obtained. Figure 27 illustrates the curing setup for the adhesive, which – in order to apply vacuum and pressure – was placed inside a vacuum bag, covered by a Teflon® sheet and a breather.

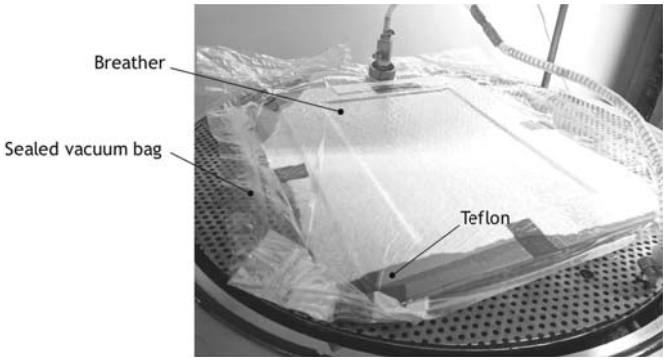

Figure 27 – Setup used to cure the adhesive inside the autoclave using the modified "vacuum release" technique.

Unfortunately, the cured adhesive plate still exhibited a fair amount of voids, especially near the upper surface, but some regions were considered acceptable for testing. The 2 mm bulk plate was abraded up to 1.7 mm using the surface grinder Chevalier® FSG-2A618, providing a better surface finish and elimination of some of the smaller voids, and then 6 specimens were cut out from it using a CNC water jet cutter (Pronum WaterJet 3015). In Figure 28a it is possible to see the visual appearance of the grinded plate, and in Figure 28b a SEM micrograph of the voids at the upper surface.

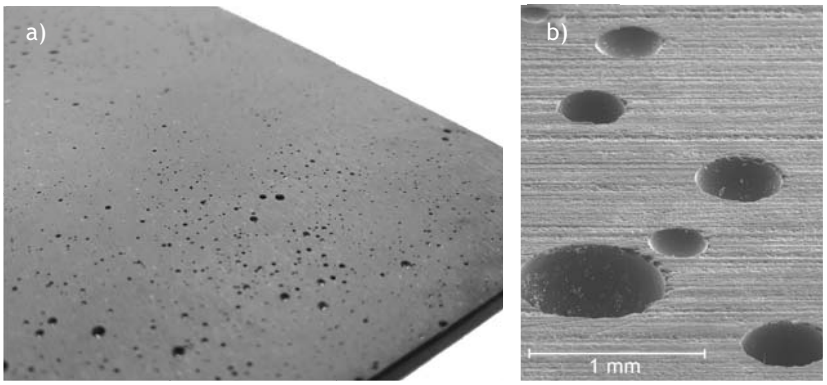

Figure 28 – Cured bulk plate of EA451 U150 film adhesive using the modified procedure: a) Macroscopic picture; b) SEM micrograph using a magnification of ×50.

The bulk adhesive specimens have a dog-bone shape and were dimensioned according to the fifth type of specimens of the standard ASTM D638-14 [95], but with increased tab's width to avoid breaking in the grips and allow for better positioning. Figure 29 illustrates the geometry and dimensions of the specimens.

Prior to testing, the dimensions of the specimens were individually measured using a micrometre and a calliper, yet they presented very low dimensional deviations among them (relative standard deviation less than 1%) due to the fact that they were cut using a CNC water jet cutter.

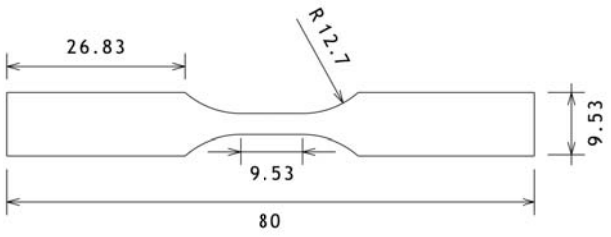

Figure 29 – Bulk adhesive specimen's dimensions (values in mm).

The specimens were positioned with a distance between grips of 25.4 mm (Figure 30), and quasi-static tensile tests were performed at room temperature (~20 °C) using a Shimadzu AGS-X universal test machine (10 kN load cell; acquisition software Trapezium X v1.4.0*)* with a testing speed of 1 mm/min, in accordance with the ASTM D638-14 [95]. A total of five specimens were tested.

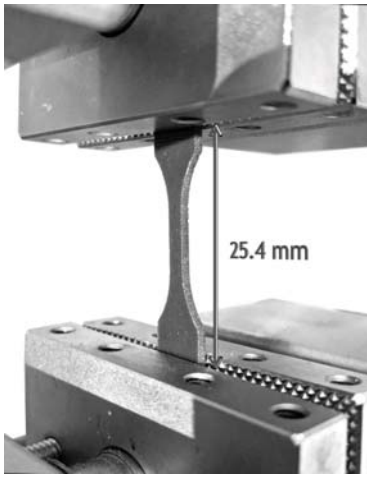

Figure 30 – Positioning of the specimen prior to testing.

After failure, it was found out that, as expected, some voids were visible in the fracture surfaces (Figure 31), presumably causing a decrease on the tensile strength. Therefore, the acquired values were adjusted according to the real fracture area, which was calculated using the software ImageJ v1.52a from analysis of pictures taken using the Nikon SMZ-2T stereomicroscope.

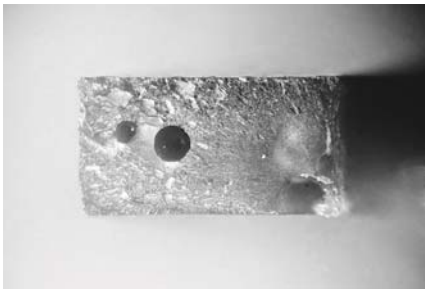

Figure 31 – Typical fracture surface of the bulk adhesive.

Table 6 lists the tensile mechanical properties obtained (after correction) for the EA451 U150 adhesive: Young's modulus (E), tensile strength (σ_{max}) and tensile failure strain (ε). The Young's modulus was directly obtained from the average value of the slopes (by linear regression, $R^2 > 0.99$) of the stress-strain curves of each specimen.

Table 6 – Obtained tensile mechanical properties of the EA451 U150 adhesive (average $\pm$ relative standard deviation).

E [GPa]	σ_{max} [MPa]	ε [%]
6.2 $\pm$ 2%	46.3 $\pm$ 13%	0.76 $\pm$ 14%

The results have a significant confidence since within the five valid specimens tested only 2% of standard deviation was observed from the average value of 6.2 GPa for the Young's modulus (E). Tensile strength (σ_{max}) and tensile failure strain (ε) values have a higher deviation, but are still within an acceptable range. Comparing these values with the mechanical properties found in the literature for various structural adhesives [96], it is clear that the EA451 adhesive performs similarly to other very brittle adhesives, such as the Redux 326 bismaleimide film adhesive, but with considerably lower tensile strength, and slightly lower tensile failure strain.

A typical experimental stress-strain curve is shown in Figure 32. No ductile deformation was found, indicating that the adhesive is very brittle. From the examination of the fracture surface (Figure 31) it was also possible to see a very characteristic brittle tension failure morphology, with very little deformation of the adhesive and a well-defined textured microflow starting from the bottom right, where the crack initiated and then rapidly propagated.

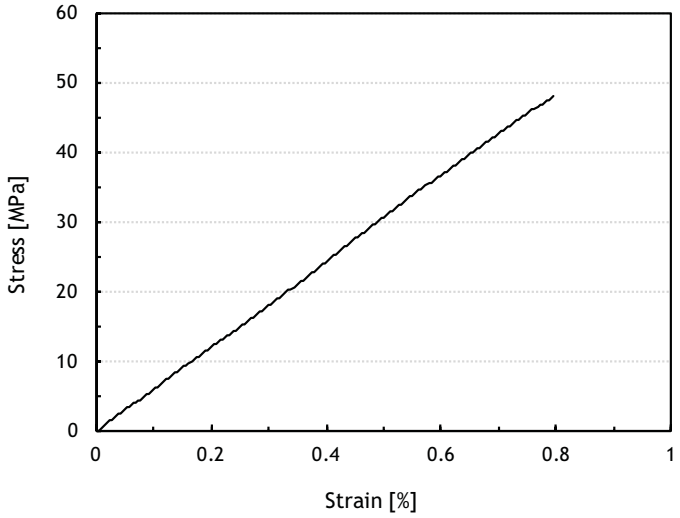

Figure 32 – Typical stress-strain for the EA451 U150 adhesive.

3.1.2. Specimens

3.1.2.1. Single Lap Joint

For the single lap shear test (SLST), the geometry of the composite specimens (single lap joints) was selected according to standard test method ASTM D 5868-01 [97], which is meant to complement ASTM D 1002 and extend its application to single lap adhesive joints of fibre-reinforced plastic (FRP) adherends. The specimens consisted of two CFRP rectangular strips of 101.6 × 25.4 × 2 mm with 12 plies laid up in the following orientation: $[0^0_2, 90^0_2, 0^0_2]_s$. The SLJs were produced by bonding the two rectangular strips together with the adhesive film along a squared overlap of 25.4 mm, as well as two CFRP bonded tabs at the end of the strips. The final geometry and dimensions can be found in Figure 33.

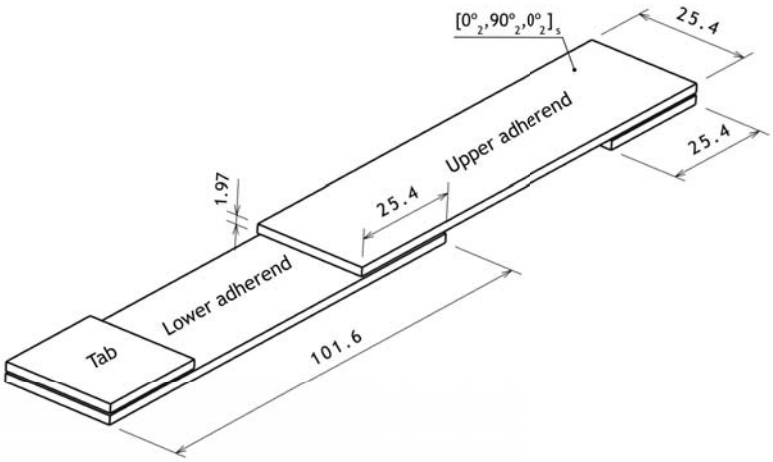

Figure 33 – Geometry and approximate dimensions of the single lap joint specimen (values in mm).

The tab ends were intended to minimize the load misalignment during the tensile test caused by the overlap in the middle, as illustrated in Figure 34.

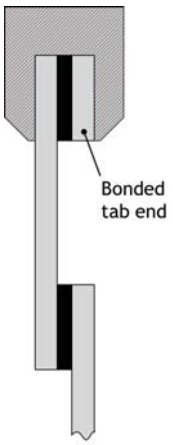

Figure 34 – Bonded tab ends (not at scale). Image adapted from [98].

3.1.2.2. Skin-to-Stiffener Joint

The stiffener pull-off test (SPOT) specimens consisted of two CFRP adherends: an inverted T-shaped stiffener (Figure 35) and a rectangular skin, with the stiffener being adhesively bonded to the skin at its mid length (Figure 36). It was decided to use a quasi-isotropic layup sequence, equal for both the adherends, of $[-45°/0°/45°/90°/90°/45°/0°/-45°]_s$. This multi-orientation type of fibre placement simulates the properties of isotropic materials (such as metals) and is very frequently used on aerospace composite structures [37].

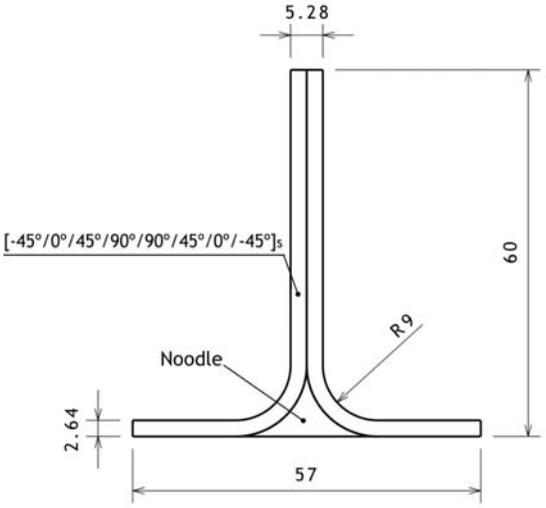

Figure 35 – Stiffener's geometry and dimensions (values in mm).

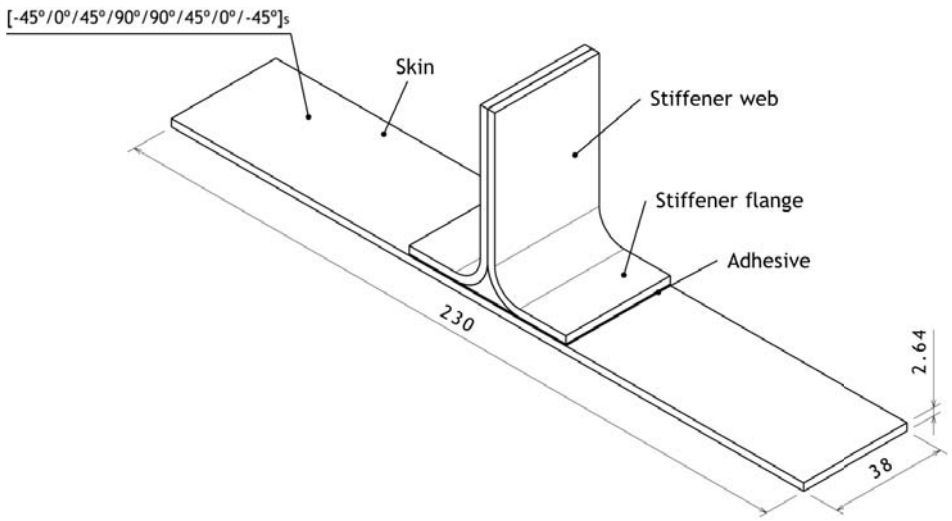

Figure 36 – Bonded joint geometry and skin's dimensions (values in mm).

3.1.3. Fabrication

In this subsection, the procedures carried out to fabricate the specimens for the single lap joint and the skin-to-stiffener joint will be described. Whereas the fabrication of the SLJ adherends was pretty straightforward and based on procedures very well described in the literature [89,99,100], the fabrication of the skin-to-stiffener joint (specifically the stiffener) is not standardized and hence entails a more complex fabrication plan, which is poorly described and illustrated in the literature, too difficult to replicate using relatively common tools and equipment, or "protected" by patents from aircraft structures' manufacturers [101-106].

3.1.3.1. Single Lap Joint

The process carried out to fabricate the CFRP single lap joints can be summarized as follows:

1. The prepreg roller was removed from the freezer, and allowed to partially thaw for approximately half an hour (at room temperature).

2. 12 plies (300 × 300 mm) were cut out using a box cutter (Figure 37).

Figure 37 – Cutting of the prepreg.

3. Each prepreg layer was placed upon a metal plate tool, which was covered with a Teflon® sheet (Release 234 TFP-1) for posterior releasing. The plies were laid-up according to the stacking sequence of $[0^0_{2,}\ 90^0_{2,}\ 0^0_2]_s$.

4. During layup, the plies were slightly heated with the use of a heating gun for better adhesion, and after placing each layer, hand pressure and a spatula were used to remove the air bubbles (Figure 38).

Figure 38 – Application of hand pressure during layup.

5. Following the final prepreg ply, the laminate was covered with another Teflon® sheet and a layer of a polyester breather (Airweave® N10) for providing airflow under vacuum, and then placed inside a bagging film (Stretchlon® 700) and sealed using a heat-sealing machine (Lovero SK-510).

7. The vacuum bag (Figure 39) was subjected to a thermal cycle inside the autoclave (Figure 40) according to the manufacturer's instructions – 1 hour of curing at 125 °C and 5 bar (relative pressure) – after which it was left to cool down overnight.

Figure 39 – Bagging setup for curing the CFRP laminate.

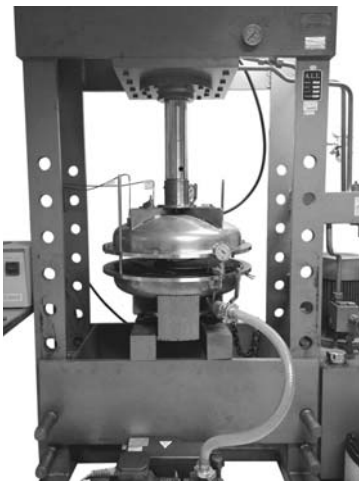

Figure 40 – Autoclave.

8. The final specimens were machined using the CNC water jet cutter (Pronum WaterJet 3015) at a cutting speed of 70 cm/min.

9. All the bonding surfaces (strips' overlap and tab ends) were cleaned with acetone to remove any oils or contamination from the surface that could lead to poor bonding. Additionally, some of the specimens were manually abraded with 120 grit silicon carbide sandpaper until no evidence of surface gloss was visible, followed by another acetone cleaning to remove the abrasion products. Special care was made during sanding to minimize fibre breakage in the composite laminate, while still removing a small layer of resin. Figure 41 illustrates the visible difference between the untreated and treated (abraded) surfaces.

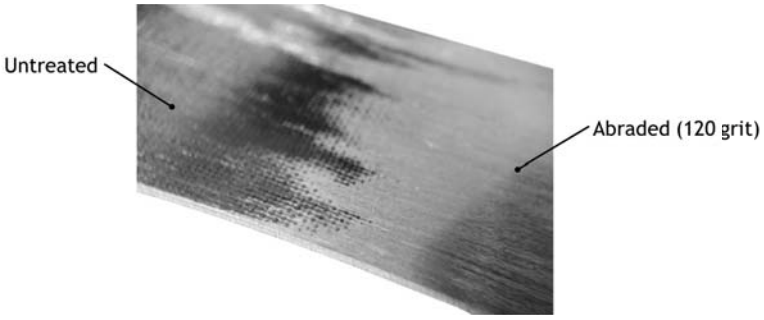

Figure 41 – Visual comparison between the not abraded (left) and abraded (right) surfaces.

10. The strips and the tab ends were secondarily bonded in only one cure cycle inside the autoclave, using 5 layers of the EA451 U150 structural adhesive film under a cure cycle of 125 °C for one hour, as recommended in the TDS. In order to properly fabricate the joint, a procedure similar to the one suggested by Boutar et al. [100] was followed, which consisted in designing and fabricating a specifically designed metal tool (Figure 42) to ensure that the specimens overlapping was 25.4 mm and that the bondline thickness was constant of 0.5 mm (which, according to Arenas et. al. [74], is the optimum adhesive thickness in structural adhesive joints). Some weights were added on top of the adherends to guarantee the alignment and application of pressure during bonding. Some specimens were cured with only one layer of adhesive film, but in this case without the use of the metal tool, only applying pressure by the use of weights.

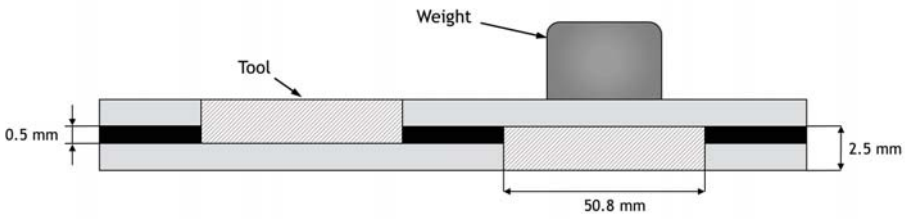

Figure 42 – Setup used for curing the single lap joint (not at scale).

11. Finally, after the cure was completed and the SLJ specimens have reached room temperature, the excess of resin from the overlap boundaries was removed by abrasive means (using sandpaper and small milled-tooth files) in order to avoid high stress concentration zones that could result in early failure initiation.

3.1.3.2. Skin-to-Stiffener Joint

To fabricate the CFRP skin-to-stiffener joint, it was decided to cure the adherends in separate stages. Despite increasing the number of cure cycles, secondary bonding prevents any release of moisture between the adhesive and the skin or stiffener, thus increasing the strength of the joint [9,37]. Although stiffeners/stringers are usually pre-cured and then bonded to the skin during its cure (co-bonded) [33,37], secondary bonding is sometimes preferred for allowing better flexibility during assembly by making possible their later integration into the fuselage.

The process carried out to fabricate the skin-to-stiffener joints was partially similar to the one used for fabricating the SLJs and can be summarized as follows:

1. The prepreg roller was removed from the freezer, and allowed to partially thaw for approximately half an hour (at room temperature).

2. 16 plies (300×300 mm) were cut off for the skin, and 32 plies (380×100 mm) for the stiffener. The plies were cut using a box cutter and taking into account the four possible orientations (0º, 90º, 45º and -45º).

3. Each layer was placed upon a tool, previously covered with a Teflon® sheet (Release 234 TFP-1) for releasing, and on top of it (except on the "untreated" specimens), a nylon peel ply to provide a clean and active surface for secondary bonding. A metal plate was used as a tool for the skin (Figure 43a); while for the stiffener, the plies were laid upon the convex size of two L-shaped metal parts (Figure 43b).

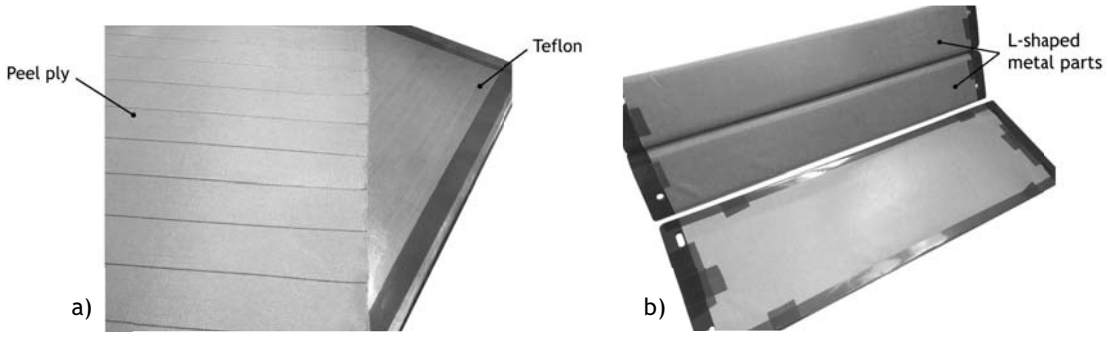

Figure 43 – Tooling parts: a) Skin's tool; b) Stiffener's tool.

4. The plies were laid up according to the stacking sequence $[45°/0°/45°/90°/90°/45°/0°/-45°]_s$, equal for the skin and the stiffener. As pointed out in the literature [37], it is a good practice to adopt a symmetrical laminated in order to minimize any residual thermal stresses caused during cure of the resin. During layup, the plies were slightly heated with the use of a heating gun for better adhesion and, after placing each layer, hand pressure and a spatula were used to remove the air bubbles. Additionally, the stiffener laminates were debulked after the first ply and every subsequent 3 plies. This procedure consisted on covering the prepreg laminate with a perforated release film (which allows air and volatiles to escape [37]) and a breather ply, applying vacuum for approximately 5 minutes before subsequent layup. Debulking ensures that there is a homogeneous consolidation, that air is removed from between the prepreg layers before final curing, and helps the prepreg to conform to the tool shape, especially in the corner [107,108]. The bagging setup used during the debulking process is illustrated in Figure 44, and pictures taken during and after the debulking are shown in Figures 45a and 45b, respectively.

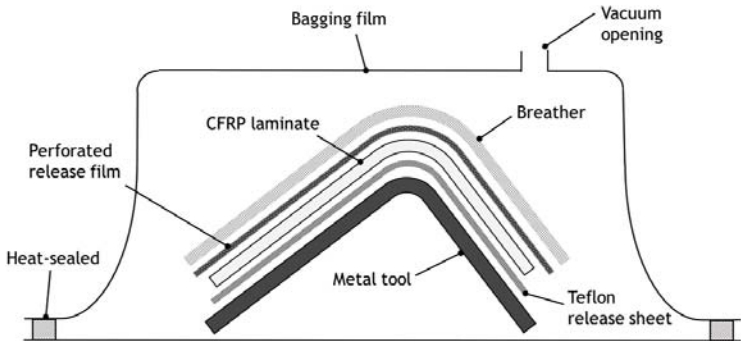

Figure 44 – Bagging setup to debulk the stiffener specimens.

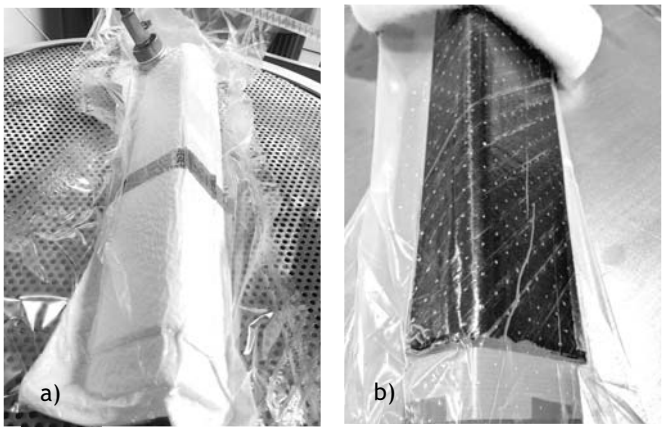

Figure 45 – Debulking process: a) During; b) After.

5. Following the final debulking process, the two L-shaped laminates were put back to back, and the cavity between (noodle) was filled with either unidirectional plies, rolled adhesive film, or left empty (with or without using an additional tool). Subsequently, the three parts of the tool were put together and slightly tightened using six Ø6 mm bolts (Figure 46).

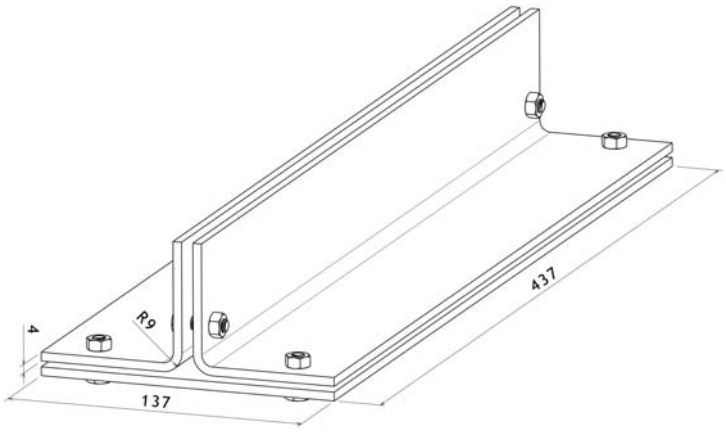

Figure 46 – Dimensions of the stiffener's tool (values in mm).

6. The laminate (or tool, in the case of the stiffener) was entirely covered by a layer of polyester breather (Airweave® N10) to provide airflow under vacuum; and the complete setup was then placed inside a heat-sealed bagging film (Stretchlon® 700 sealed with the Lovero SK-510 sealing machine) as schematized in Figures 47a and 47b for both the skin and the stiffener, respectively.

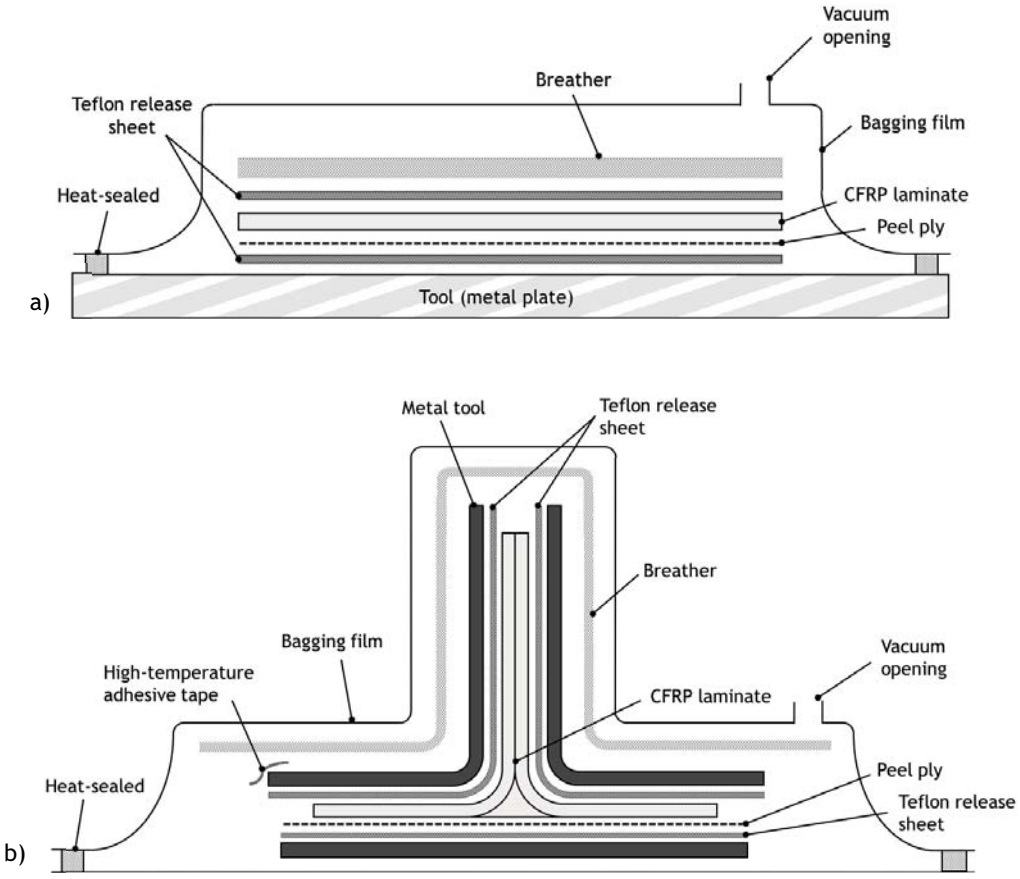

Figure 47 – Bagging setup: a) Skin's setup; b) Stiffener's setup.

7. The vacuum bag was subjected to a thermal cycle inside the autoclave according to the manufacturer's instructions (Figure 48). After 1 hour of curing at 125 °C and 5 bar (relative pressure), the laminate was left to cool down overnight. The peel ply was left on the laminate in order to preserve the surface from any contamination that could result in poorer bonding. The skin specimens' geometry was drawn on the CAD software CATIA v5, and exported for CNC machining using FabLab's (UBI's Manufacturing Laboratory) Pronum WaterJet 3015 at a cutting speed of 70 cm/min. From each cured CFRP laminate plate (300 × 300 mm), it was possible to obtain nine 38 × 200 mm skin specimens. The stiffener specimens were manually cut using an angle grinder to cut lengthwise along the stiffener's flanges and a RF-912B bandsaw to cut crosswise, and then rectified to the final dimensions using a surface grinder machine (Chevalier® FSG-2A618). Up to nine specimens were obtained from the long 200 mm CFRP stiffener.

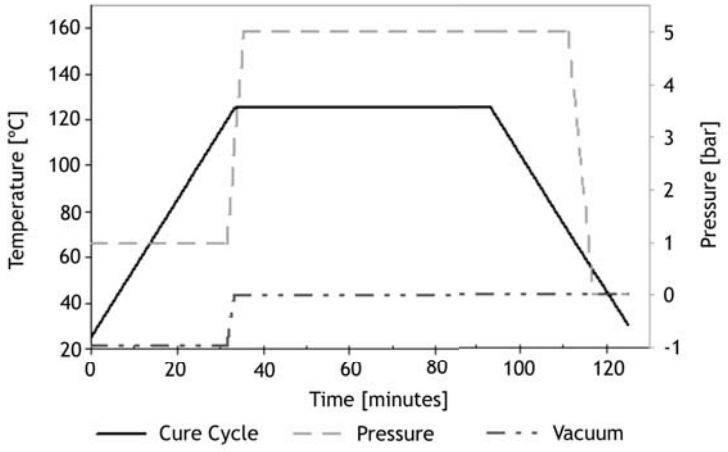

Figure 48 – Recommended cure cycle for the HS 160 REM. Adapted from [86].

8. Prior to the adhesive curing, the adherends were dried for 24 hours at 50 °C (inside the Carbolite Eurotherm oven) to avoid any release of moisture from the CFRP specimens to the adhesive [93]. The peel ply was removed from the parts, and the bonding surfaces of some specimens (depending on their series) were abraded with 120 or 240 grit silicon carbide sandpaper, followed by an acetone cleaning to remove the abrasion products. Typically, four layers of adhesive film were cured between the adherends for 1 hour at 125 °C inside the autoclave, while using weights on the stiffener flanges to apply pressure. Some variations of the curing procedure of the adhesive were made on certain specimens, as it will be explained in the next section.

9. After reaching room temperature, the skin-to-stiffener joints were removed from inside the autoclave and the excess of adhesive was removed using small milled-tooth files and 240 grit sandpaper on the Struers DAP-V 10" Round Polisher (Figure 49) in order to avoid high stress concentration zones which could result in early failure initiation.

Figure 49 – Removal of the excess adhesive using the Struers DAP-V Round Polisher.

3.2. Experimental Methodology

3.2.1. Single Lap Shear Test

The single lap shear test (SLST) is a very widely used test for characterizing adhesively bonded joints. While being quite simple (and cheap) to prepare and test, the single lap joint (SLJ) reproduces the geometry of many practical applications, as various joints encountered in aeronautical structures [98]. In fact, SLSTs are still among the most widely used tests for gathering important mechanical information of adhesively bonded systems, namely the "apparent" shear strength [57,98], providing, for example, means by which FRP surface treatments may be compared [97]. For all these reasons, they were the obvious choice to perform some preliminary testing, as a quality validation of the adhesive and a way to increase the proficiency in producing, preparing, and testing adhesive joints.

It was also intended to perform a brief study of the influence of different surface treatments (untreated, abraded with 120, 240 and 400 grit sandpaper), but after machining the specimens with the water jet cutter it was found out that many of them exhibited a high degree of delamination (Figure 50), making them unfeasible for testing.

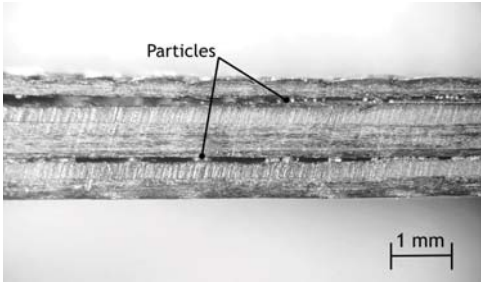

Figure 50 – Fibre delamination and embedded particles on specimens machined by water jet.

Besides, some shiny particles were found between the delaminated layers, which at first seemed difficult to explain. Mayuet et. al. [109] have studied the defects developed onto the surface of CFRP samples machined by water jet and discovered that the shiny spots (Figure 50)

correspond to abrasive particles from the water jet that penetrated in these spaces during machining. These particles may also have caused additional damage between layers as they still possess sufficient cutting energy at the moment of their introduction.

Taking this into account, only five total specimens were possible to validate for testing. Their nomenclature is indicated in Table 7:

Table 7 – Specimens' nomenclature.

Nomenclature	No. of adhesive layers	Surface treatment	No. of valid specimens
5lay_120	5	120 grit sandpaper	3
5lay_none	5	None	1
1lay_120	1	120 grit sandpaper	1

The specimens were tested using the Instron 1341 servo-hydraulic testing machine (100 kN load cell; data acquisition software Wave Metrics version 1.5) using standard tensile fixtures. All SLSTs were carried out under monotonic loading at room temperature (~20 °C) with a cross-head speed of 13 mm/min (at displacement control), in accordance with the standard test method ASTM D 5868-01 [97].

After each test, the fracture surfaces were examined visually and using optical microscopy to determine the failure mode. The "apparent" shear strength of the joint was calculated by dividing the value of the ultimate applied load at failure by the overlapping bond area (25.4×25.4 mm). It was only possible to obtain an average result for the "5lay_120" series.

3.2.2. Stiffener Pull-Off Test

Following the learning curve initiated with the SLSTs, it became easier to move to the more challenging and complex skin-to-stiffener joints, for which the overall process had to be planed, from the design and fabrication of the specimens to the testing of the bonded joints.

Firstly, it was necessary to guarantee an adequate experimental setup to perform the pull-off tests. Given that there were no existing fixtures that were able to clamp the skin during the pull-off, they had to be developed and produced. It was decided that the best procedure was to fabricate two specifically designed steel fixtures in a way that they would be compatible with the Instron 1341 (Figure 51) T-slot table (used for bending tests).

Figure 51 – Instron 1341 testing machine.

Therefore, two types of fixtures were produced: clamping fixtures, and simply supporting fixtures. Each type consists of a two-piece symmetrical pair of metal parts, whose geometry and dimensions are illustrated in Figure 52:

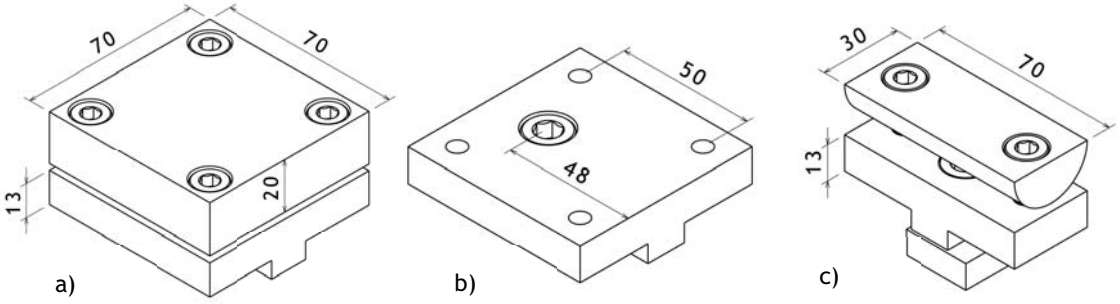

Figure 52 – Geometry and dimensions (values in mm) of the fixtures: a) Clamping fixture; b) Lower part of the clamping fixture; c) Simply supporting fixture.

Each part is attached to the Instron T-slot table using a Ø10 mm steel bolt and a steel nut, and the upper and lower pieces are tightened together using four (in the case of the clamping fixture) or two (plus two washers as spacers, for the simply supporting fixture) Ø8 mm steel bolts.

Similar types of fixtures were used in SPOTs reported in the literature [1,3,15-32], but clamping fixtures seem to be more often preferred, unless failure at the support points is observed [29]. Because of that, and also because the clamping fixtures offer a higher structural integrity of the overall system – partially because the main bolt is positioned in the inner side, this way creating a backstop for the bending moment during the pull-off – it was decided to use them for all the SPOTs.

The final SPOT setup is illustrated in Figure 53. From the side view (Figure 53b) it is possible to see how the fixtures are attached to the Instron's table. During testing, a vertical tensile load was applied to the stiffener web, which is clamped to the Instron's tensile hydraulic grip.

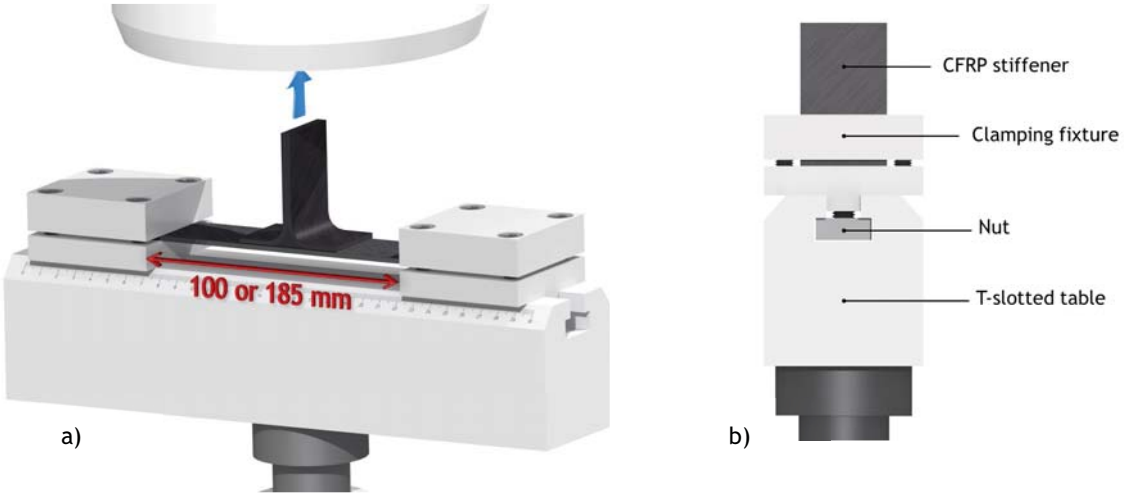

Figure 53 – Stiffener pull-off test setup: a) Perspective view; b) Side view.

To what the experimental procedure concerns, the first step was to characterize the differently treated surfaces using scanning electron microscopy (SEM), profilometry, and water contact angle (WCA) measurements. SPOTs were then performed on "standard" skin-to-stiffener joints (bonded after different surface treatments), trying to achieve a correlation between the previous findings of the surface characterization, and the mechanical performance of the joint.

After performing the first tests, it became evident that the process used to cure the adhesive was inadequate, leading to numerous macro-voids in the adhesive bondline; so a step back was taken to evaluate different approaches to cure the adhesive and find an optimal method that minimizes or eliminates the macro-voiding problem.

Thereafter, using the best possible combination of the previously studied parameters, different designs of the stiffener were experimentally tested, entailing a novel design and fabrication method that minimizes the twisting of the fibres during the composite curing. The fracture surfaces of these specimens were then analysed by fractography (using SEM) in order to better understand the failure mechanisms and deduce the occurring failure modes.

All SPOTs were carried out using the Instron 1341 servo-hydraulic testing machine (100 kN load cell; data acquisition software Wave Metrics version 1.5) under monotonic loading at room temperature (~20 °C), with a cross-head speed of 2 mm/min when the skin span was 185 mm, and 1 mm/min when the skin span was 100 mm (at displacement control). Typically, a minimum of three specimens for each condition were tested. The loads and cross-head displacements were recorded during testing, all tests were video-recorded, and pictures were taken at relevant occurrences (e.g. crack initiation).

After each test, all the fracture surfaces were photographed, then examined visually and using optical microscopy. Some of the specimens of the last series (different noodle designs) were later dissected for SEM fractography analysis.

3.2.2.1. Influence of the Surface Treatment

From the possible surface treatments typically used prior to bonding adhesive joints, it was decided to study four differently treated surfaces: untreated, abraded with 120 grit, abraded with 240 grit sandpaper, and treated will peel ply (without release agents).

In order to do so, the resulting surfaces' morphology was evaluated using SEM. Four different rectangular specimens were prepared following the same procedure carried out when fabricating the skin-to-stiffener joints, and later observed using the Hitachi S-3400N scanning electron microscope (Figure 54) at the UBI's Optical Centre. Several images were taken using ×50 (only for the peel ply treated specimen), ×100, and ×500 magnifications.

Figure 54 – Hitachi S-3400N scanning electron microscope.

Although the SEM micrographs were very successful in evaluating the surface's morphology, they were incapable of providing an accurate evaluation of the surface roughness. Therefore, the roughness of the specimens' surface was evaluated using a Hommel T1000 linear surface profiler with a LV16 skidded drive unit (Figure 55). The specimens were placed and fixed with duct tape to a stable platform, and three valid measurements were made for each specimen using an evaluation length (L) of 4.80 mm and a sampling length (l) of 0.80 mm.

Figure 55 – Hommel T1000 linear surface profiler and LV16 unit.

The surface parameters possible to obtain were R_a, R_q, R_t, R_{pm}, R_{3z}, R_{zISO}, R_{zDIM}, and each can be defined as follows [110,111]:

Roughness Average (R_a) is the arithmetic average of the absolute values of the profile heights over the evaluation length. This parameter is easy to define and gives a good general description of height variations, however, it does not give any information about the wavelength and it is not sensitive to small changes in profile.

RMS Roughness (R_q) is the root mean square average of the profile heights over the evaluation length and represents the standard deviation of the distribution of surface heights.

Maximum Height of the Profile (R_t) is the vertical distance between the highest peak and the lowest valley along the evaluation length.

Average Height of Peaks (R_{pm}) is defined as the arithmetic average of the maximum height of peaks obtained for each sampling length (l) of the evaluation length (L).

Third Maximum Peak-to-Valley Height (R_{3z}) is the arithmetic average of the third maximum peak-to-valley heights in the evaluation length.

Ten Point Height of Irregularities (R_{zISO}) is the arithmetic average of the absolute values of the heights of five highest profile peaks and the depths of five deepest valleys within the evaluation length.

Average Peak-to-Valley Height (R_{zDIM}) is defined as the arithmetic average of the maximum peak-to-valley height within five consecutive sampling lengths over the evaluation length.

After properly characterizing the surfaces' morphology, it was important to assess their wettability and surface free energy. This was made conducting water contact angle (WCA) measurements using the contact angle goniometer "Dataphysics contact angle system OCA" with a high speed camera (Figure 56). The procedure consisted on depositing a liquid droplet of 4μl of demineralized water (polar liquid) into the specimens' surface (just after being cleaned with acetone), and measuring the static contact angle after 3 seconds. Subsequently,

a similar process was carried out depositing 2μl of diindolylmethane (nonpolar liquid) on the same specimens. Three valid measurements for each specimen and liquid were recorded to the "SCA 20 Software for OCA and PCA", where the average angle measurements for both liquids were introduced, returning the values for the surface energies for each specimen – including the dispersive and polar components – using the Owens-Wendt (OW) method.

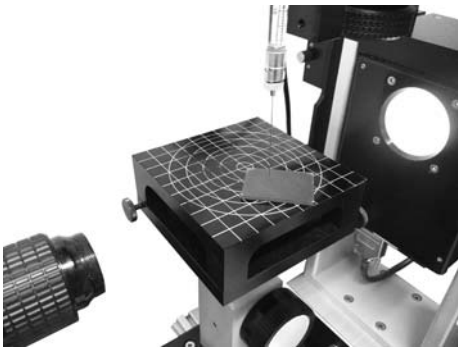

Figure 56 – Dataphysics contact angle system OCA goniometer.

During the first tests, it was interesting to notice (by examination of the water droplet from a top view) that on the abraded specimens, the water droplet had an affinity to align to the fibres' direction, forming an oblong shape. This was confirmed by placing a water drop using a syringe and observing its behaviour through a stereo microscope, from which the image in Figure 57 was taken. This phenomenon probably occurred due to the capillary action between the water drop and the exposed fibres (the "valleys" between them).

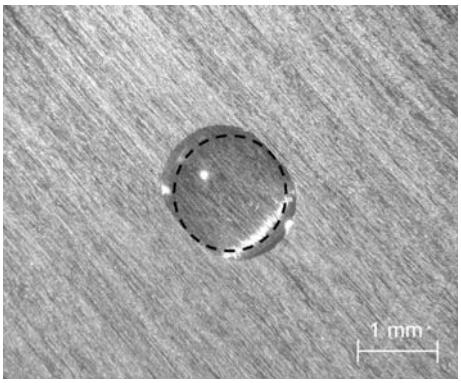

Figure 57 – Water drop on the abraded surface.

As the literature does not seem to define any standard testing procedures taking into account this effect, it was decided to repeat the measurements, rotating the specimen so that its fibres were not aligned at 45º with the camera view (Figure 58 – view a), but rather perpendicularly oriented (Figure 58 – view b). As expected, this resulted in a slight decrease of the WCA values.

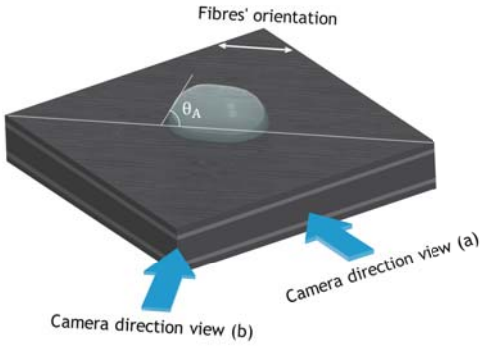

Figure 58 – Different orientations of the specimen to the goniometer camera view.

Following the surface characterization of the surfaces, SPOTs were performed on three series of skin-to-stiffener joints with different surface treatments: untreated, treated will peel ply (without any release agents), or abraded with 240 grit sandpaper (after removing the peel ply). The grit size was only decided to be 240 after performing the surface characterization, and was also based on the findings by Boutar et. al. [100], which concluded that for bonded single lap joints, surfaces treated with higher grit sizes (finer sandpapers) have resulted in higher shear strength of the joint.

Except for the surface treatment, all T-joints were produced under the same conditions. The noodle was filled with unidirectional fibres prior to the specimens' cure, and four layers of adhesive film were later cured between the skin and the stiffener at 120 °C for 1 hour, applying the "vacuum release" technique when it first reached 120 °C, but without using hydrostatic pressure (only with weights on top of the stiffener flanges).

SPOTs were performed on a minimum of three T-joints for each surface treatment condition, and a skin span of 185 mm was used. The obtained values were the maximum load P_{max}, displacement at maximum load $\delta_{P_{max}}$, and stiffness $K_{P_{max}}$. Stiffness was obtained by diving the maximum load of each specimen with the correspondent displacement at maximum load.

3.2.2.2. Influence of the Joint Fabrication Method

The aim of this second study was to understand, from a range of seven different methods to cure the adhesive, which one would give the best results in terms of maximum load capacity of the cured T-joint.

Considering the number of different curing methods, it was necessary to make a compromise between the number of specimens and the number of curing methods to evaluate, meaning that in order to evaluate all the methods, it would not be feasible to produce at least 21 specimens (following the same practice of testing at least three specimens for each condition). Taking this into account, it was decided to test only one valid specimen for each curing method.

Despite being an inadequate procedure in terms of reliability of the results, this allowed to quantitatively and qualitatively evaluate a satisfactory number of parameters that would otherwise not be possible (within a reasonable time and resources).

The T-joints were individually produced using the same adhesive cure cycle of 120 °C for 1 hour inside the autoclave. Each joint was left to cool down inside the autoclave overnight in order to assure a gradual temperature decrease and reduce residual stresses that might reduce the joint strength [98].

Table 8 presents the correlation between the specimen's nomenclature and the curing method used. This table will be repeated further in Chapter 4, as it pertains to the results observed.

Table 8 – Correlation between the specimen's nomenclature and the curing method used.

Specimen nomenclature	Number of adhesive films	Fibreglass carrier	Pressure	Vacuum release	Particles addition
A	2	No	No	No	No
B	4	No	No	No	No
C	4	Yes	No	No	No
D	4	Yes	5 bar	No	No
E	4	Yes	No	Yes (120 °C)	No
F	4	Yes	5 bar	Yes (120 °C)	No
G	4	No	5 bar	No	Cork

It was possible to evaluate the influence of the following parameters: number of adhesive layers (2 vs. 4); application of a fibreglass veil as a carrier to control the bondline thickness and adhesive bleed off; application of hydrostatic pressure (5 bar) inside the autoclave; application of the vacuum release technique (at 120 °C); application of hydrostatic pressure together with the vacuum release technique; and embedding micro-particles of cork in the adhesive.

The fibreglass veil was cut out to the proper dimensions, and placed after the second film layer of adhesive (and before the third), as illustrated in Figure 59.

Figure 59 – Application of a fibreglass veil as a carrier for the adhesive.

The procedure of embedding micro-particles of cork in the adhesive was made following the conclusions published by Barbosa et. al. [112], which have successfully increased the toughness of a brittle epoxy paste adhesive by using natural micro-particles of cork. In order to try to replicate this procedure and hopefully achieve the same results on the EA451 U150 adhesive (which was found to be very brittle), micro-particles of cork were "powered" between the layers of film adhesive (Figure 60). About 0.04 g of cork particles were used, representing ~11% in terms of mass fraction of the uncured adhesive (4 layers). Obtained D-Values by particle size analysis were [113]: D10 = 18.6 μm, D50 = 78.9 μm e D90 = 208.3 μm. These values are the intercepts for 10%, 50% and 90% of the cumulative mass, respectively. The density of the cork particles is ~0.1095 g/cm^3.

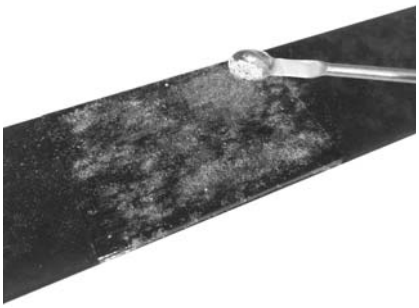

Figure 60 – Application of micro-particles of cork between the adhesive layers.

Furthermore, it was learned from the first tests that it was necessary to use some kind of physical barrier in order to avoid the adhesive flowing out of the bonding area during its cure. In order to do so, high temperature duct tape was used in the exterior all borders of all specimens.

After the complete cure and cooling of the T-joints, SPOTs were performed using a skin span of 185 mm. The results were only evaluated taking into account the maximum load, P_{max}, of each joint.

3.2.2.3. Influence of the Noodle Design

Using the best combination of parameters evaluated up to this point, the final series of specimens consisted in a complete redesign of the noodle region, introducing an additional tool during the fabrication of the stiffener, and comparing the performance of the obtained T-joints with other designs more often used and described in the literature.

The idea for the noodle redesign was motivated by the findings reported by Huang [21], which suggested that if there was no twisting of fibres, a stiffener with a large radius and a large cross-section area would not so easily fail in the noodle compared with a smaller one, and could eventually lead to a stronger joint.

The developed auxiliary tool consists in a deltoid shape metal rod which is introduced in the noodle cavity of the CFRP stiffener after its layup and prior to curing, as illustrated in Figure 61:

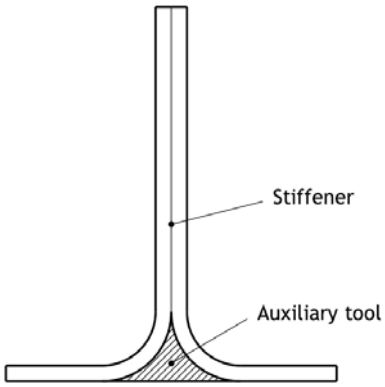

Figure 61 – Auxiliary tool positioning.

The auxiliary tool was machined from a steel bar using the FabLab's CNC Litz CV-1000 Vertical Machining Center. Its geometry and dimensions can be found in Figure 62, along with a picture of the finished tool.

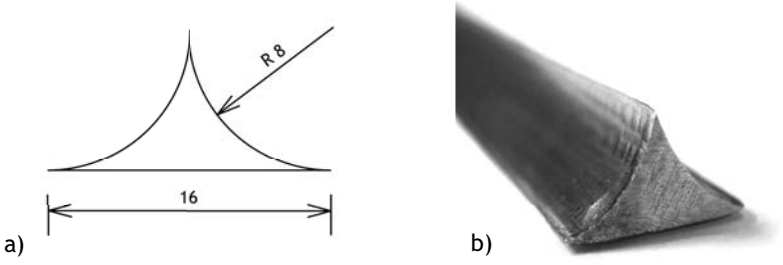

Figure 62 – Auxiliary tool: a) Dimensions and geometry; b) Finished tool.

Preceding its placement, the auxiliary tool was covered with high-temperature duct tape to facilitate demoulding. Subsequently, the deltoid-shaped tool was placed on the empty space between the L-laminates as illustrated in Figure 63.

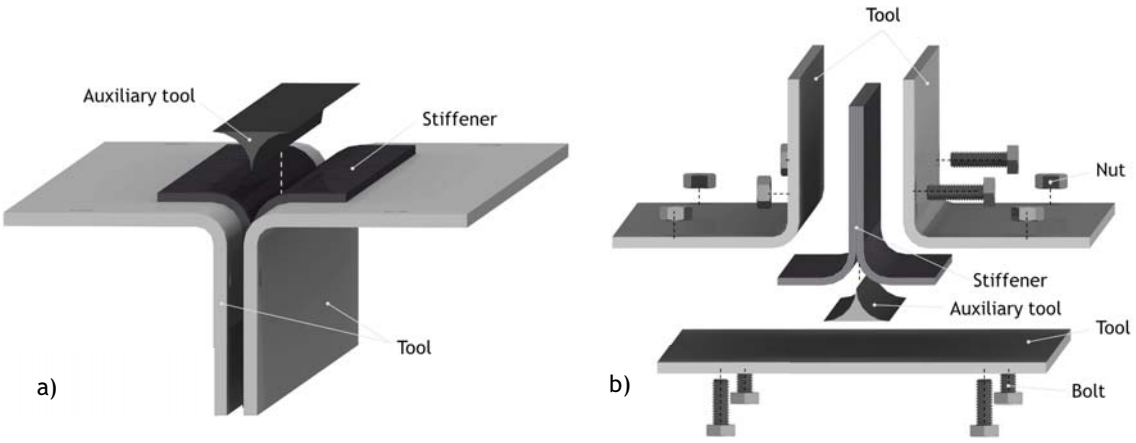

Figure 63 – Tooling setup with the auxiliary tool: a) Introduction of the auxiliary tool after layup; b) Complete tooling setup.

Two series of specimens were produced using the auxiliary tool: either left empty (nomenclature: "Tool_empty") or filled with five pieces of adhesive which were hand rolled (Figure 64a) and pushed into the noodle cavity while applying hand pressure to remove any entrapped air ("Tool_adhesive"). Three other series of specimens were produced without using the auxiliary tool, filling the noodle before the laminate's cure with either unidirectional fibres ("Std_fibres"), rolled film adhesive ("Std_adhesive"), or left empty ("Std_empty"). Prior to bonding, all adherends were cleaned with acetone and with an organic brush to remove any contaminants and dust (Figure 64b). The joints were then cured inside the autoclave at 125 °C for 1 hour and using 5 bar of hydrostatic pressure. The fibreglass veil was used as a carrier in all specimens, as well as high-temperature duct tape in the exterior borders to avoid the adhesive flowing out.

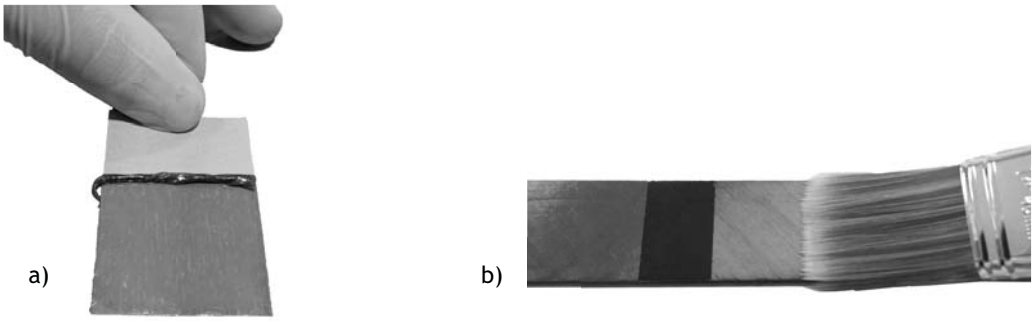

Figure 64 – Preparation for bonding: a) Formation of hand rolls of adhesive; b) Cleaning of the skin adherends.

Table 9 lists the specimens' nomenclature and the corresponding filling material used.

Table 9 – Correlation between the specimens' nomenclature and the filling material used.

	Auxiliary tool	Filling material
Std_fibres	No	Unidirectional fibres
Std_adhesive	No	Rolled film adhesive
Std_empty	No	Empty
Tool_empty	Yes	Empty
Tool_adhesive	Yes	Rolled film adhesive

SPOTs were performed with a skin span of 100 mm and a cross-head speed of 1 mm/min. This reduction in the skin span was expected to increase the stiffness of the skin and hopefully induce a crack initiation in the noodle region. The following parameters were recorded: maximum load P_{max}, displacement at maximum load $\delta_{P_{max}}$, stiffness at maximum load $K_{P_{max}}$, failure load P_{fail}, displacement at failure load $\delta_{P_{fail}}$, stiffness at failure load $K_{P_{fail}}$, crack initiation load P_{init}, displacement at crack initiation $\delta_{P_{init}}$ and stiffness at crack initiation $K_{P_{init}}$.

3.2.3. Fractographic Analysis

After the failure of composite components, studying the fracture surface morphology (fractography) is crucial to provide an insight of the damage and failure mechanisms, leading to important findings that can be useful for optimising future designs and develop predictive models based on the experimental observations [35].

Additionally to the visual and optical inspection of all exposed surfaces, the failure surfaces of the specimens with different noodle designs were analysed using scanning electron microscopy (SEM). This technique uses a narrow electron beam that is scanned across the fracture surface, building up images that are similar in appearance to optical images, therefore making interpretation much easier than with other methods such as TEM [35].

In order to analyse the surfaces using SEM, three different areas of interest had to be selected for dissection so that they would be possible to fit inside the microscope. When dissecting the specimens, cuts were preferably made through regions in which there was evidence of single failure modes and away from potential sites at which the failure has initiated or changed mode or direction, in order to reduce the introduction of post-failure damage.

Cuts were made using a Struers Accutom-2 cutting machine with a diamond blade at a slow cutting rate and without any water lubrication, as recommended by Greenhalgh et. al. [35] to avoid contamination of the fracture surfaces by water contaminants and lubricants. Nevertheless, the cutting process generated a fine dust that ingressed into the fracture surface. This resulting dust was removed, firstly, using dry compressed air, and then by cleaning the specimens using an ultrasonic bath in distilled water, followed by a 30 min dry at 40 °C in the oven (Carbolite Eurotherm). The specimens were then stored in a protective box containing a silica desiccant. Special care was taken when handling the specimens to avoid any contamination (such as skin oil) that might appear embedded within the fracture surface.

Just prior to SEM analysis, the specimens were sputter gold coated to ensure that the surface is conductive and that there is no deviation of the electron beam (specimen charging). During the analysis, the specimens were tilted to 60 degrees in order to assist in perceiving the surface depth and allow features like cusps and scarps to be clearly visible.

This page intentionally left blank

Chapter 4 – Results and Discussion

In this chapter, the results for both the single lap shear tests (SLSTs) and the stiffener-pull-off tests (SPOTs) will be presented. This includes the characterization of the different bonding surfaces, experimental testing, and failure analysis through visual inspection, optical microscopy and scanning electron microscope (SEM) fractography.

4.1. Single Lap Shear Test

The single lap joints (SLJs) were successfully produced as illustrated in Figure 65. The load-displacement curves of all specimens are presented in Figure 66, and the results for the maximum "apparent" shear strength, as well as the maximum loads, are presented in Table 10.

Figure 65 – Single lap joint.

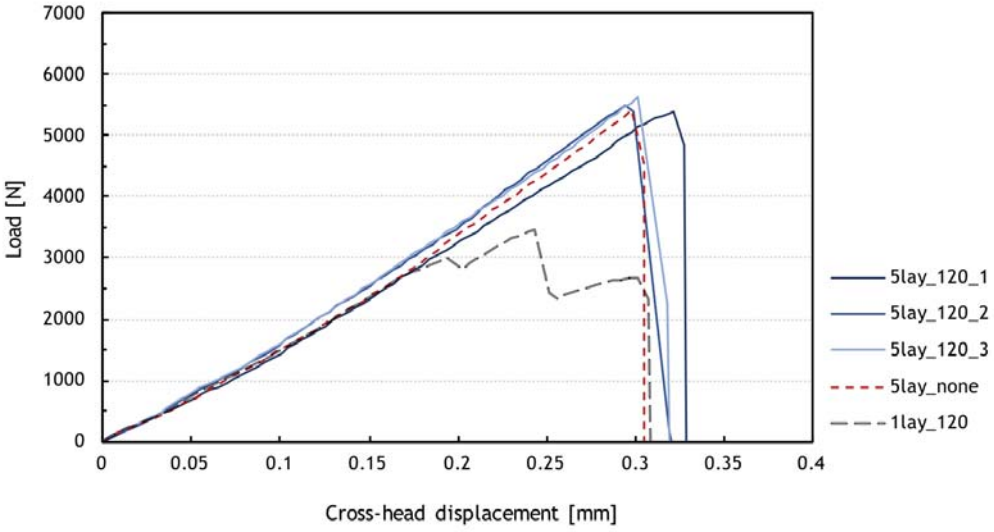

Figure 66 – Load-displacement curves for the single lap shear tests.

Table 10 – Obtained absolute values for the maximum load (P_{max}) and "apparent" shear strength (ASS). Values for the "5lay_120" are presented in the form of "average $\pm$ relative standard deviation".

Specimen's series	P_{max} (N)	ASS (MPa)
5lay_120	5507 $\pm$ 2%	8.54 $\pm$ 2%
5lay_none	5424	8.41
1lay_120	3471	5.38

Comparing these values to the ones found in the literature, they were found to be lower than expected, but still within the usual range for SLJs tested according to the same standard (ASTM D5868-01) [99,114], which is a satisfactory indication of the quality of the adhesive. However, it is worthwhile to note that the values of the "apparent" strength of the joint are also dependent on the adherend material and some other factors of preparation of specimens such as the adhesive curing procedure.

In terms of types of failure, the SLJs either failed by adhesive failure, with a complete layer of cured adhesive being visible in one of the surfaces; or by mixed failure (coexisting cohesive and adhesive failures). Although the number of tested specimens was too small to achieve conclusions about the influence of the surface treatment, it is plausible that the cause of adhesive failure was from poor surface preparation, as found for the "5lay_none" specimen which did not underwent any kind of surface treatment. Table 11 presents the correlation between each specimen and its failure type.

Table 11 – Types of failure of the SLJ specimens.

Specimen	Type of failure
5lay_120_1	Mixed failure (cohesive and adhesive)
5lay_120_2	Mixed failure (cohesive and adhesive)
5lay_120_3	Adhesive failure
5lay_none	Adhesive failure
1lay_120	Mixed failure (cohesive and adhesive)

In terms of the failure sequence, all the specimens bonded with five layers of adhesive failed very abruptly, coincidently with the moment where they sustained the maximum load. The joint bonded with just one layer had a different behaviour, undergoing two load drops before the final failure, which occurred at a value inferior to the maximum load, and about half of the maximum/failure load for the other joints. This progressive failure of the adhesive was probably

caused by non-uniform bonding at the overlap from an insufficient quantity of adhesive, as illustrated in Figure 67. All specimens failed at approximately the same displacement.

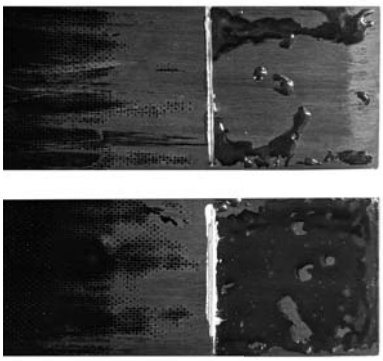

Figure 67 – Non-uniform bonding of SLJ.

To sum up, although no conclusions were possible to make regarding the influence of the surface treatment, it was possible to perform a comparative evaluation with other joints from the literature in terms of "apparent" shear strength, detect some manufacturing mistakes such as non-uniform adhesive bondline, and learn about some technical aspects that should be considered when producing and testing bonded joints.

4.2. Stiffener Pull-Off Test

The skin-to-stiffener joints were successfully produced. Figure 68a illustrates the cured stiffener filled with unidirectional prepreg plies in the noodle region, and Figure 68b illustrates the cured bonded joint pre-treated with a peel ply.

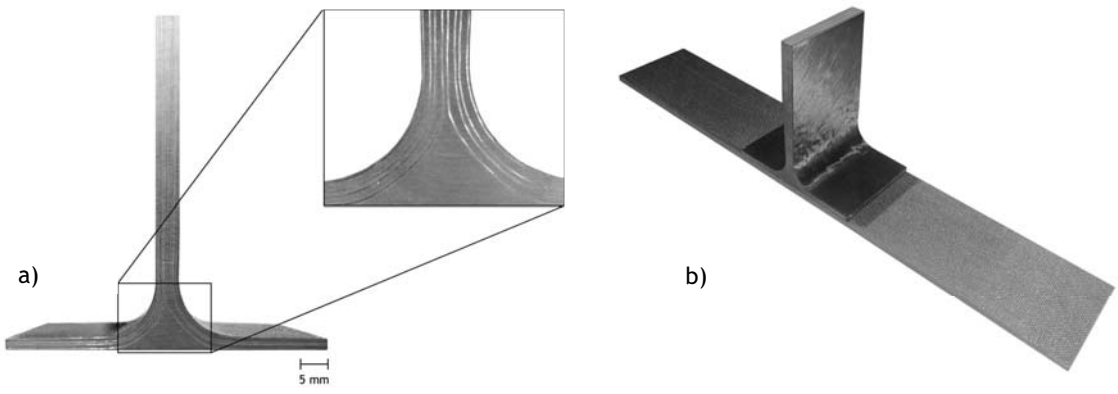

Figure 68 – Cured specimens: a) Stiffener filled with 0º plies in the noodle; b) Skin-to-stiffener joint.

The final dimensions of the specimens are illustrated in Figure 69. The difference between the planned (Figures 35 and 36) and the final dimensions (Figure 69) of the specimens can be chiefly attributed to the resin bleed off that occurred during the cure stage of the CFRP laminates, especially in the stiffener where additional pressure was applied with the use of bolts. It was noticed that in most of the stiffener specimens, the thickness of the stiffener flanges was smaller at the ends than at the middle (near the noodle). This effect is sometimes referred to as the "Mexican hat effect", and is a common problem associated with the manufacturing of stiffeners and stringers [105].

In order to control the resin bleed off, high-temperature duct tape could be used along edges of the laminate, creating a physical barrier that stops the resin to exit during cure; and spacers could be placed between the two "L" parts of the tool and the lower part, guaranteeing an exact and constant thickness along the stiffener flanges. Unlike traditional hand laid-up laminates, most prepregs contain the ideal amount of resin for maximum cured properties (the used HD 160 REM adhesive contains 36% of resin), which means that no resin needs to be removed during cure.

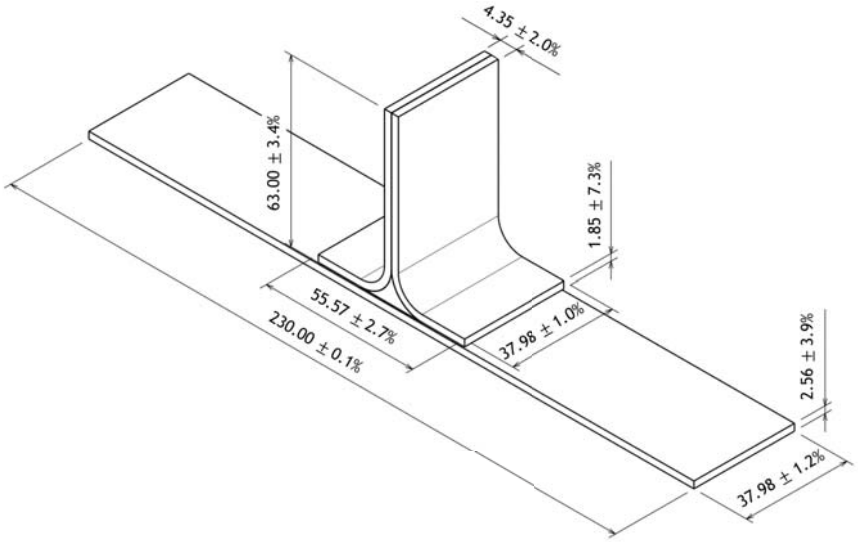

Figure 69 – Final dimensions of the cured skin-to-stiffener joint (average ± relative standard deviation; values in mm).

The average thickness of the adhesive bondline was 0.7 mm, with a relative standard deviation of only 3% (Figure 70).

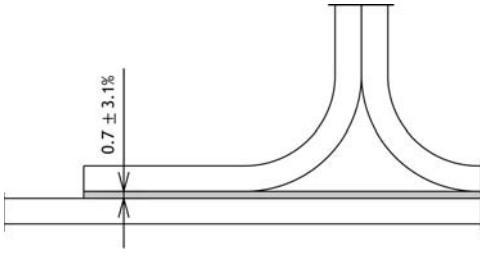

Figure 70 – Adhesive bondline thickness (average ± relative standard deviation; values in mm).

4.2.1. Surface Characterization

4.2.1.1. Scanning Electron Microscopy

SEM micrographs of the CFRP specimens are illustrated in Figure 71 for the untreated, abraded with 120 grit sandpaper, abraded with 240 grit sandpaper, and peel ply treated surfaces.

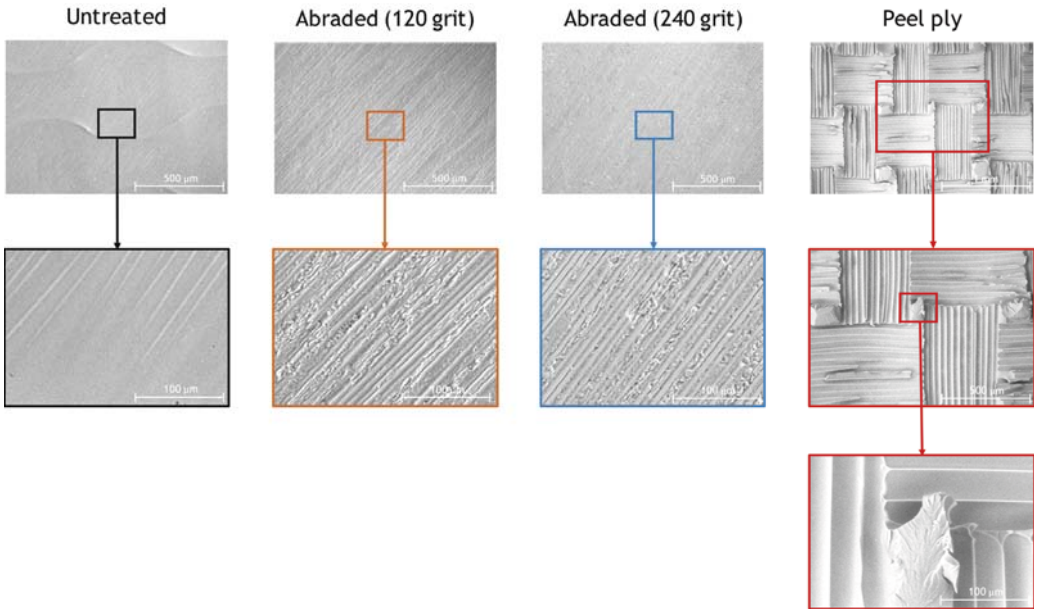

Figure 71 – SEM micrographs of the differently treated surfaces.

These SEM micrographs were extremely useful to understand and distinguish the different morphologies, which exhibited very distinct features.

On the untreated surface, it was possible to observe that the surface was very smooth, except for the curved lines, which correspond to the imprints left from the Teflon® sheet. The fact that most of the carbon fibres are covered and cannot be seen, suggests that the substrate is still covered with a considerable layer of epoxy matrix.

Both the abraded specimens presented similar surfaces, with a sharp and rough texture. As a result of the removal of the top layer of resin, the carbon fibres were exposed. Some of the fibres were noticeably damaged during the abrasion process. The specimen abraded with 120 grit sandpaper seemed to exhibit a rougher surface than the one with 240 grit, with larger and more visible “scratches” on its surface.

Lastly, the peel ply treated specimen exhibited a very textured and well defined surface, which was provided by the peel ply imprints that were left on its surface. There appears to be no sign of remains (tendrils) of the peel ply fibres, but rectangular regions of fractured epoxy were found between the warp and weft tows, similarly to other surfaces that have been reported in the literature [115] when using nylon peel plies. This surface morphology implies that

interfacial fracture between the peel ply fabric fibres and the epoxy matrix has occurred (probably due to insufficient strength between the peel ply and the matrix), as illustrated by the red arrow (no. 2) in Figure 72. The green (no. 1) arrow represents the ideal mode of fracture, which in reality is rarely achieved. The other two arrows, blue (no. 3) and orange (no. 4), represent other undesirable modes of fracture that can happen if the bond between the peel ply and epoxy is stronger than the peel ply fibres, or if the interlaminar strength of the laminate is low, respectively.

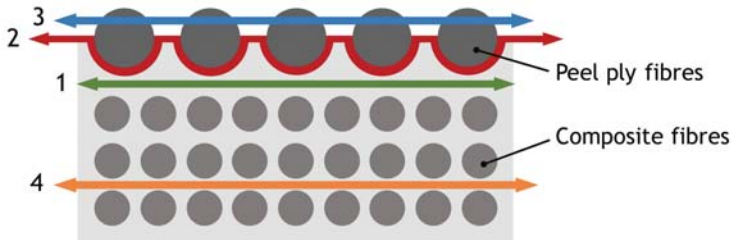

Figure 72 – Possible fracture paths during removal of peel ply. Adapted from [115].

4.2.1.2. Profilometry

The results from the roughness measurements are presented in Table 12 with all the obtained parameters.

Table 12 – Obtained surface roughness parameters (average ± relative standard deviation).

	R_a (µm)	R_q (µm)	R_t (µm)	R_{pm} (µm)	R_{3z} (µm)	R_{zISO} (µm)	R_{zDIM} (µm)
Untreat.	1.6±22%	2.0±20%	10.1±13%	6.3±18%	N/A	9.4±14%	8.8±14%
120 grit	0.9±6%	1.1±5%	6.1±2%	2.6±8%	4.5±2%	5.7±3%	5.3±1%
240 grit	0.7±3%	0.9±3%	5.5±7%	2.4±5%	3.8±5%	4.9±3%	4.8±2%
Peel ply	11.2±11%	13.1±11%	55.6±13%	25.3±9%	18.1±14%	51.0±14%	46.8±6%

Figure 73 illustrates some examples of typical roughness profiles (R-Profiles) obtained for the differently treated specimens.

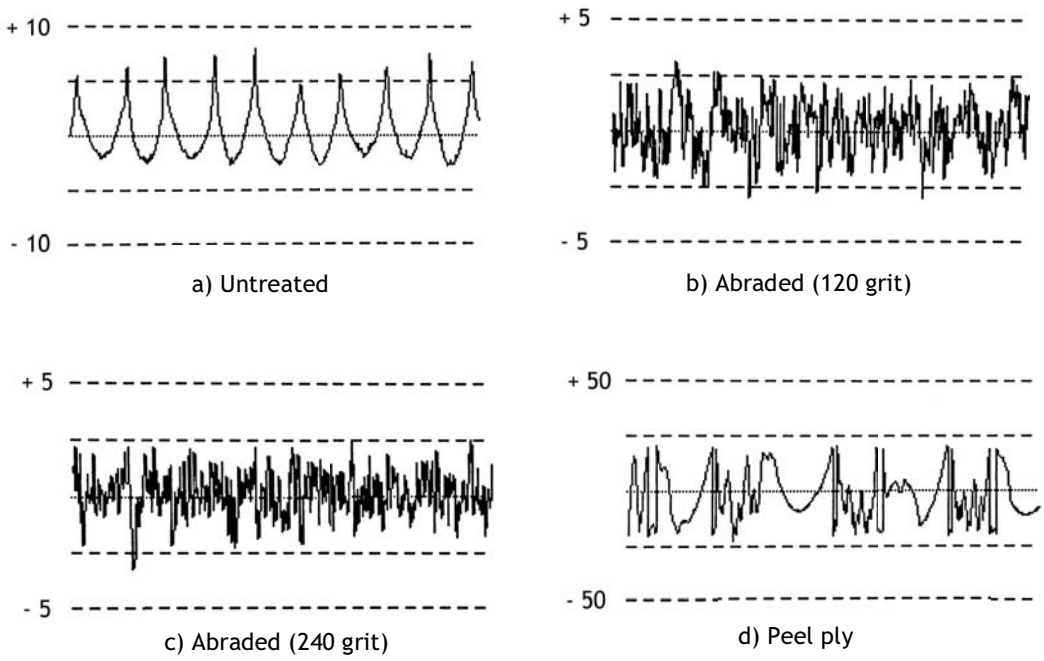

Figure 73 – Surface roughness profiles: a) Untreated; b) Abraded with 120 grit sandpaper; c) Abraded with 240 grit sandpaper; d) Peel ply.

All parameters show a similar trend: the higher values for the surface roughness parameters were obtained from the peel ply treated specimen (with an arithmetic average roughness 600% higher than the untreated specimen), being followed by the untreated surface, and then the surfaces abraded with 120 and 240 grit sandpaper. Although the abraded surfaces had very similar results, the specimen abraded with 120 grit had slightly higher values for all the roughness parameters.

Another interesting observation is that it was not possible to obtain the R_{3z} value for the untreated specimens. Analysing its R-Profile (Figure 73a), it is clear why that may have happened: the high length separation between peaks/valleys did not allow to process at least five third point height parameters in order to obtain an average value of peak-to-valley height.

Despite the very distinct results obtained from profilometry, when comparing them with the findings previously made using SEM micrographs (Figure 71) of the surface's morphology (from which we concluded that, for example, the untreated surface was the smoothest), it was realised that the roughness parameters are misrepresentative in terms of fully characterizing the surface roughness – meaning that they do not account for other surface parameters and then might have led to deceitful conclusions.

Particularly in the case of the untreated specimen, all the roughness parameters were higher than the ones obtained for the abraded specimens, but only because they result from an evaluation length of 4.80 mm, where the peak points from the Teflon® imprints have caused an

increase in the roughness parameters, which are an arithmetic average of surface features along that evaluation length (except for the maximum height of the profile, R_t).

Another way to intuitively compare the surface roughness of the untreated and the abraded surfaces is by visual examination of their reflectivity. In fact, it was clear that the untreated surface has a much higher reflectivity than the abraded one (Figure 74), and therefore should, at least at a micro-scale, have a less rough surface than the one abraded with sandpaper [116,117].

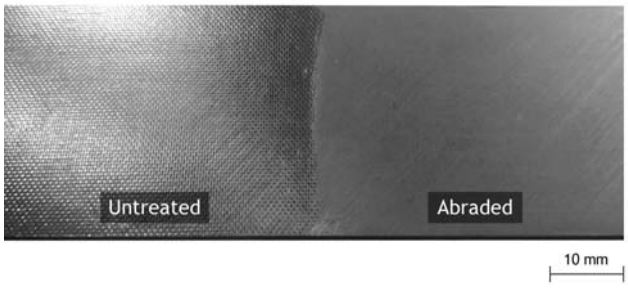

Figure 74 – Comparison between abraded and untreated surfaces' reflectivity.

In order to better illustrate the correspondence between the roughness parameters (especially the peaks and valleys) and the surface morphology, some pictures were taken using optical microscopy and edited in a way that the roughness profiles were overlapped with an example of the matching location at the specimen surface (Figure 75).

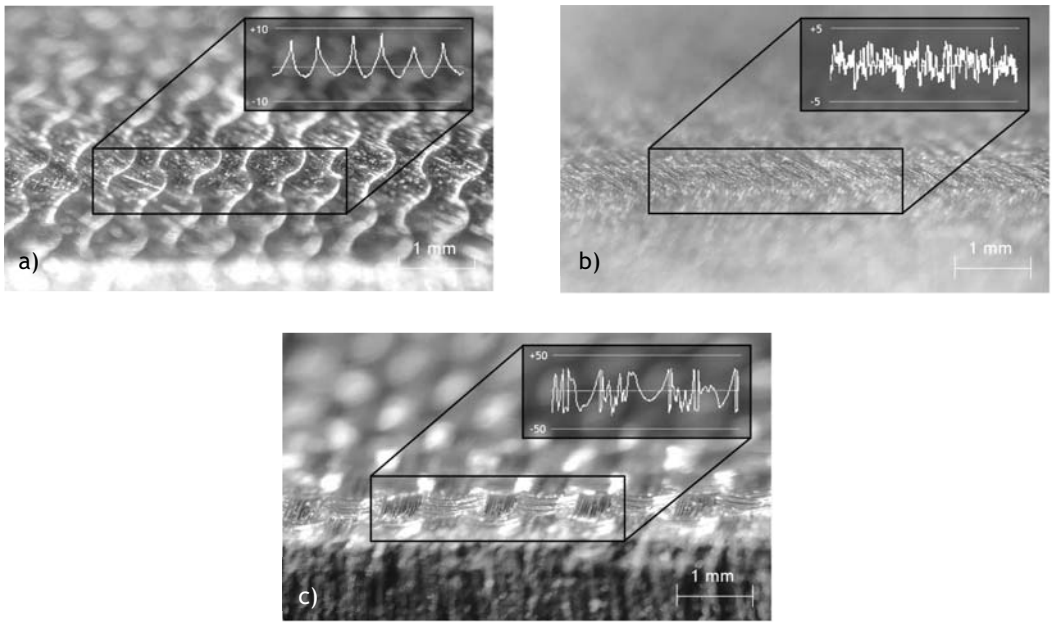

Figure 75 – Correlation between the surface morphology and the roughness profiles: a) Untreated; b) Abraded with 240 grit; c) Treated with peel ply.

The values for the (relative) standard deviation are satisfactory, except for the untreated and peel ply treated specimens. The irregular nature of these specimens' texture (with the surface morphology varying according to the location) has resulted in different measured roughness parameters, as the measurements were also made at different positions within the specimen.

A final comment can be made saying that, in general, the real surface geometry is so complicated that even a large number of parameters cannot provide a full description of the surface morphology. In this particular case, the used profilometer only provides amplitude parameters, which are used to measure the vertical characteristics of the surface deviations from the mean line. On the other hand, if spacing parameters – like the number of peaks and slopes, mean spacing between peaks, average wavelength, etc. –, were obtained, it is excepted that they would deliver a much better description of the surface roughness. In particular, it would be of great importance to obtain an estimation of the surface area of each specimen, as it is directly related to the bondable surface area (with increased mechanical interlocking), and one of the most important parameters governing the bonding quality [70]. Nevertheless, from the analysis of the roughness profiles (Figure 73), it is safe to assume that the specimens abraded with 240 grit sandpaper have the highest surface area, as the number of peaks and valleys is visibly higher than with any other specimens.

4.2.1.3. Contact Angle Analysis

The contact angle measurements for the water and diiodomethane droplets are indicated in Table 13, together with the obtained surface free energy values (SFEV) for each specimen using the Owens-Wendt (OW) method.

Table 13 – Contact angle and surface free energy values for the differently treated surfaces.

	Contact angle (average ± relative standard deviation)		**Surface Energy (mN/N)**		
	Water	Diiodomethane	Total	Dispersive	Polar
Untreated	72° ± 2.6%	36° ± 1%	47.6	41.6	6.1
120 grit	80° ± 0.1%	31° ± 7%	46.6	43.8	2.9
240 grit	78° ± 2.4%	23° ± 6%	49.7	46.7	3.0
Peel ply	59° ± 3.8%	13° ± 20%	59.3	49.5	9.9

The peel ply is the specimen with the highest value of total surface energy, followed by the specimen abraded with 240 grit sandpaper. It is interesting to notice that although the average water contact angle is higher for the abraded surfaces than for the untreated surface, when

using the diiodomethane (non-polar or dispersive liquid) the results are the opposite, meaning that the abraded surfaces interact better with non-polar liquids than the untreated. Therefore, the behaviour is different whether the liquids are in contact with the epoxy resin or with the carbon fibres.

The high relative standard deviation of contact angles values for the peel ply specimens can be explained by the amorphous shape of the drops in this case. As similarly reported by Flinn and Tracey [118], the drop spreads through the peel ply channels freely and then stops when reaching a peel ply imprint with perpendicular peel ply channels. A picture of this phenomenon was taken using the Nikon SMZ-2T stereomicroscope and is illustrated in Figure 76.

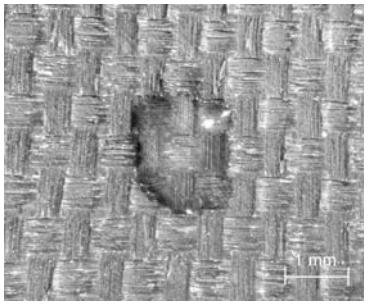

Figure 76 – Amorphous shape of a water drop in the peel ply treated surface.

The bulk adhesive was also tested following a similar procedure, in order to assess if it had the tendency to better interact with materials with higher dispersive or polar components. The results are presented in Table 14.

Table 14 – Contact angle and surface free energy values for the differently treated surfaces.

	Contact angle (average ± relative standard deviation)		**Surface Energy (mN/N)**		
	Water	Diiodomethane	Total	Dispersive	Polar
EA451 U150	94° ± 1%	45° ± 2%	37.7	37.1	0.6

The bulk adhesive has a surface energy of 37.7 mN/N, from which about 98% account for the dispersive component. This means that it tends to interact much better with surfaces with high dispersive components of surface free energy. Analysing once again the results from Table 13, it is possible to conclude that the surface with the highest dispersive component is the peel ply treated, being followed by the surface treated with 240 grit sandpaper.

Another very simple, quick and non-destructive test that has been frequently used to assess the surface preparation quality, is the water break test. It consists in pouring water onto the surface and observing how the water behaves, in order to determine if the bonding surface has sufficient surface energy to achieve proper adhesion.

Therefore, in order to better and intuitively observe the differences between the wettability behaviour on differently treated surfaces, a water break test was performed on an untreated skin specimen which was partially abraded with 240 grit sandpaper. Both surfaces were completely wet under running tap water, and then observed how they behaved when removed from the water.

Due to the gravity effect, the water trickled along the surface. After a few seconds, it was possible to observe (Figure 77) that the upper part (abraded surface) retained a lot of water, forming a water sheet (indicating hydrophilic behaviour), while the lower part (untreated) had a hydrophobic behaviour, beading the water and causing it to run down almost completely.

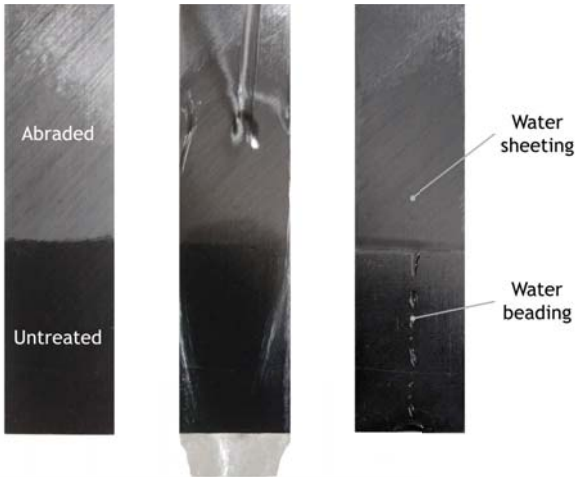

Figure 77 – Water break test.

These results were somewhat unexpected since the water contact angle measurements clearly indicated a higher water contact angle for the abraded specimens, which should mean less wettability of the surface when in contact with water. This apparent contradiction between the contact angle measurements and the water break tests can be explained by the following causes:

1. Water contact angle measurements were performed on a non-ideal surface, particularly due to the high and non-uniform roughness of some specimens. Wenzel [119] proposed the following equation for the apparent contact angle formed by a liquid wetting a rough surface: $cos\,\theta_W = \bar{r} \cdot cos\,\theta_Y$, where θ_W is the apparent contact angle, θ_Y is the Young contact angle for an ideal surface, and $\bar{r}$ is the average roughness ratio, defined as the ratio between the actual and projected solid surface area ($\bar{r} = 1$ for a smooth surface and > 1 for a rough one). Unfortunately, the average roughness ratio, $\bar{r}$, is not possible to obtain directly and can only be calculated from 3D roughness parameters. It is possible to assume, however, that if the Wenzel equation were used, the Young's contact angle would be considerably smaller for the abraded specimens (which is assumed to be the one with the largest surface area); and as pointed out in previous research [72], the surface energy (its increase) of rough surfaces is mostly governed by their physical morphology. Another very important phenomenon (and not

described by the Wenzel equation) is called wetting hysteresis, which is the range of apparent contact angles from the advancing (maximal) contact angle to the receding (minimal) contact angle [120], and can be of the order of dozens of degrees [57], possibly leading to conflicting results;

2. Chemical modifications of the surface, as the abraded surface has many more fibres exposed, while the untreated surface has a layer of epoxy matrix. Other physical phenomenon can also be taking place, such as adhesion forces and/or capillary action (as illustrated in Figure 58) between the liquids and the exposed carbon fibres. The chemistry of the peel ply treated surfaces might also be affected by the fractured epoxy portions that were found;

3. It has been pointed out in the literature [118] that recent research has shown that the water break test might be inadequate for composite surfaces. On the contrary, contact angle measurements are more sensitive and have the potential to quantitatively evaluate the surface free energy. It is not possible, however, to conclude which of the two tests give a better indication of the surface wettability in this particular case.

From these tests, and for the reasons formerly pointed, it is possible to conclude that even a large number of parameters cannot provide a full description of the surface free energy and morphology. While the SEM micrographs provided a good description of the surface, both the profilometry and wettability results have led to conflicting observations – although this can possibly be amended if the factors previously mentioned are taken into account.

4.2.1. Influence of the Surface Treatment

The stiffener pull-off tests on differently treated joints have provided the results indicated in Table 15, in terms of maximum load (P_{max}), displacement at maximum load ($\delta_{P_{max}}$), and stiffness at maximum load ($K_{P_{max}} = P_{max}/\delta_{P_{max}}$).

Table 15 – Stiffener pull-off tests results: maximum load P_{max}, displacement at maximum load $\delta_{P_{max}}$, and stiffness at maximum load $K_{P_{max}}$ (average $\pm$ relative standard deviation).

	P_{max} (N)	$\delta_{P_{max}}$ (mm)	$K_{P_{max}}$ (N/mm)
Untreated	1013 $\pm$ 5%	13.6 $\pm$ 5%	74.8 $\pm$ 7%
Abraded (240 grit)	1064 $\pm$ 4%	14.2 $\pm$ 7%	75.2 $\pm$ 3%
Peel ply	631 $\pm$ 16%	8.7 $\pm$ 15%	72.3 $\pm$ 2%

The results for the maximum load and stiffness are also shown in Figures 78a and 78b (respectively) in the format of a bar chart:

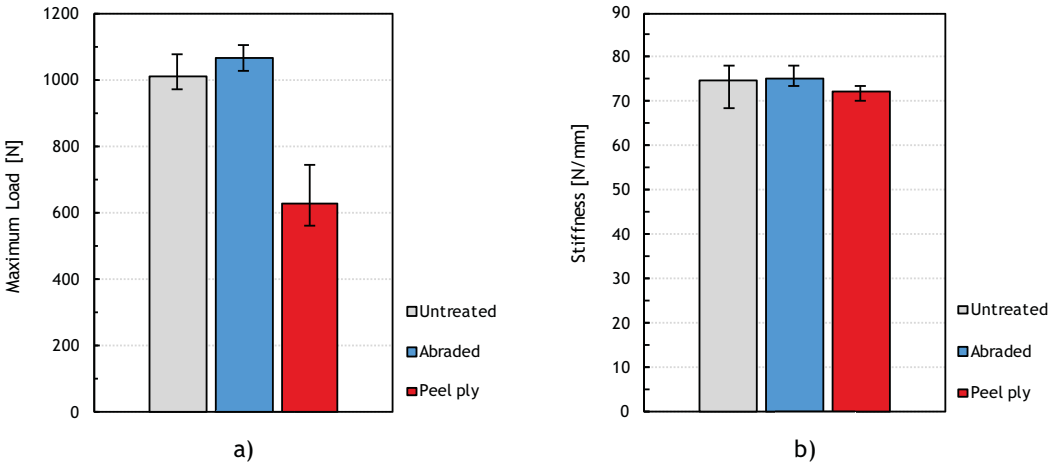

Figure 78 – SPOT results for the differently treated specimens: a) Maximum load; b) Stiffness.

By analysis of the obtained values for the maximum load, displacement at maximum load and stiffness, it is possible to establish the following conclusions:

The specimens which performed the best in terms of maximum load capacity were the ones abraded with 240 grit sandpaper, being followed by the untreated specimens (practically the same, only about 5% less). The peel ply specimens behaved clearly worse than these two series, with approximately 40% decrease in terms of maximum load. The maximum displacement values followed a similar trend, so that the stiffness was also maximum for the abraded series and minimum for the peel ply series, but now with a much lower deviation between the three series. In fact, when comparing the stiffness values, they were within a relative standard deviation of only ~2%. This is in accordance with the observation that the failure sequence was similar to all specimens, resulting from no significant difference in the stiffness of the joint.

In Figure 79, three typical load-displacement curves ($P-\delta$) for each series of specimens are presented. Four points of the curve for the peel ply specimen are linked to four pictures (Figure 80) taken during testing at the moments indicated in the curve. The failure sequence can be described as follows:

The test initiates at null displacement, when the skin is completely horizontal (Figure 80 – 1). After some displacement/bending of the skin, damage initiated at one of the tips (with no particular preference) of the stiffener flange, and propagated along the skin/adhesive interface (adhesive failure) towards the centre of the stiffener (Figure 80 – 2). Shortly after that, and before the first crack reached the centre, another similar crack initiated at the opposite side of the stiffener, also spreading towards the centre (Figure 80 – 3). The peak load occurred when the contact area reached a minimum value, and contact between the skin and the stiffener was only maintained in the centre, where there was lower local bending. At that point, both crack paths met, and the final failure occurred abruptly with complete detachment of the stiffener from the skin (Figure 80 – 4). This type of failure sequence will be further referred to as Type I.

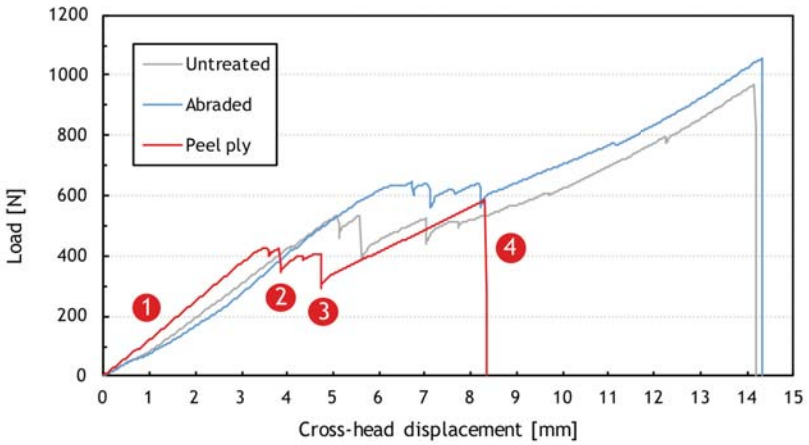

Figure 79 – Three typical load-displacement curves for differently treated specimens.

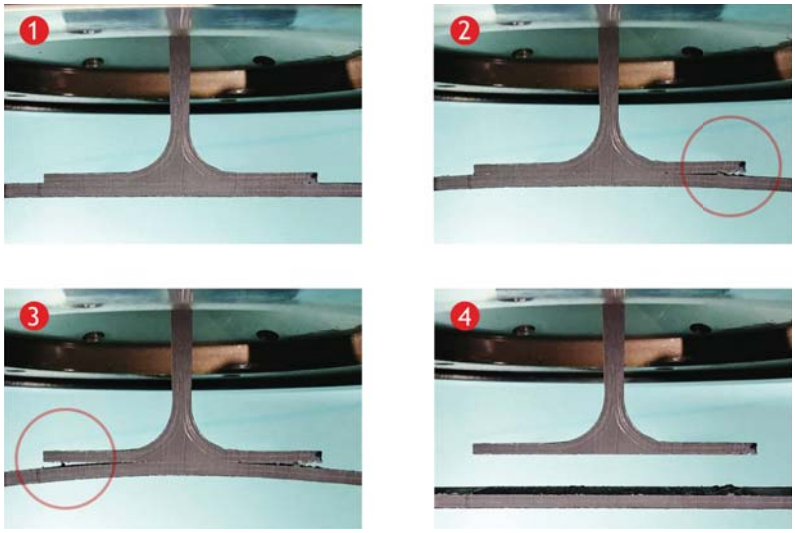

Figure 80 – Type I failure sequence: 1) Starting point; 2) Crack initiation at the tip of the stiffener flange; 3) Second crack initiation on the opposite side of the stiffener; 4) Complete detachment from the skin.

Doing a correlation between the obtained values and the surface characterization of the bonding surfaces, the following conclusions can be made:

An increase in the roughness parameters does not necessarily mean an increased strength of the joint. In fact, when considering the obtained R_a value (similar tendencies were found to the other parameters) for the three tested surfaces, the higher the R_a value, the smaller the maximum load of the bonded joint. However, it is presumed that at a micro-level, the morphology provided by the abrasion was ideal for the formation of mini scarf joints on the adherend surfaces, increasing the surface area and producing a better surface morphology for the adhesive to fill the very small groves and valleys and bond in. On the other hand, in the peel ply treated surfaces, the adhesive might not be able to penetrate into the valleys and make close contact with the adherend, resulting in less adhesion strength.

In terms of surface free energy, the SPOT results were contradictory to the obtained values for the peel ply specimen, which was the one with higher surface free energy (for both the dispersive and polar components) and the one which performed the worst both in terms of maximum load. One of the most probable causes for this difference is the surface roughness, which caused an increase on the apparent water contact angle according to the Wenzel equation [119]. Moreover, as already mentioned, the worse SPOT performance might have been caused by the presence of the fractured peaks of resin to which the adhesive would not bond.

A further detailed analysis was made by examining the fracture surfaces, both visually and using optical microscopy. Since the specimens within the same series exhibited very similar surfaces, some typical images will now be presented and described.

From visual inspection of the failure surfaces of the first untreated specimens, all the three types of laminar failure were macroscopically identified (Figure 81):

- Translaminar: through the thickness in which the fibres of the first (-45º) and second (0º) layers have been broken;
- Intralaminar: through the thickness in which only matrix or fibre/matrix interfaces of the second layer (0º) have been broken;
- Interlaminar (delamination): in the laminate plane, by separation between the first (-45º) and second (0º) plies. Easily identified by the exposed layer at the diagonal [35].

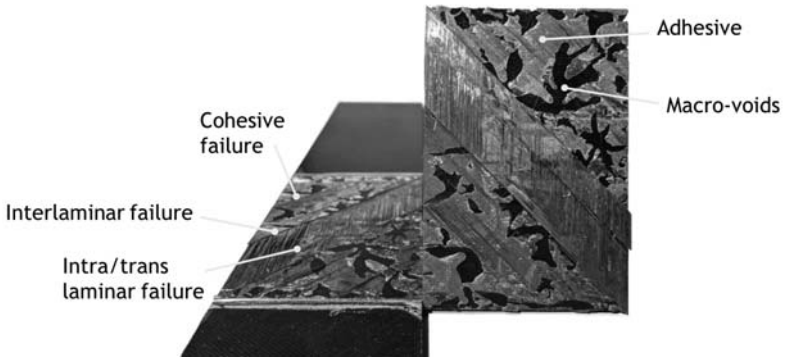

Figure 81 – Typical fracture surface of the untreated specimens.

Besides laminar failure, a layer of adhesive was found in both surfaces, meaning that cohesive failure has also occurred. As stated by Davis and Andrew [121], cohesive failure might arise from the large and irregular voids (macro-voids) found in the adhesive bondline of all specimens, leading to inadequate residual bond overlap.

All the untreated specimens exhibited similar fracture surfaces, only varying the predominance of each type of failure. Cohesive failure was dominant for all specimens (60-80%), but there was also inter/intra/translaminar failure of the CFRP skin (20-40%). Interlaminar failure is very frequently seen in bonded composite laminates because adhesives are highly susceptible to peel stresses and first ply delamination [121].

The specimens abraded with 240 grit sandpaper exhibited similar failure surfaces (Figure 82) as the untreated ones, but with smaller macro-voids and a slightly higher predominance of inter/intra/translaminar failure of the CFRP skin (30-40%).

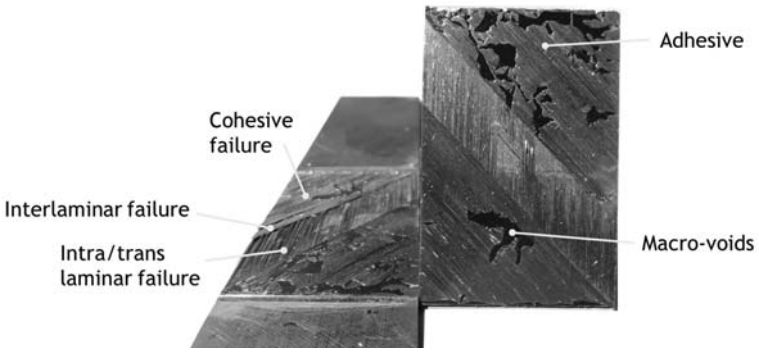

Figure 82 – Typical fracture surface of the abraded specimens.

As for the peel ply treated specimens, there was 100% cohesive failure in all specimens, with a thin layer of adhesive being left in both the skin and stiffener surfaces (Figure 83). Macro-voids could still be found, and account for a larger area than in the untreated and abraded specimens.

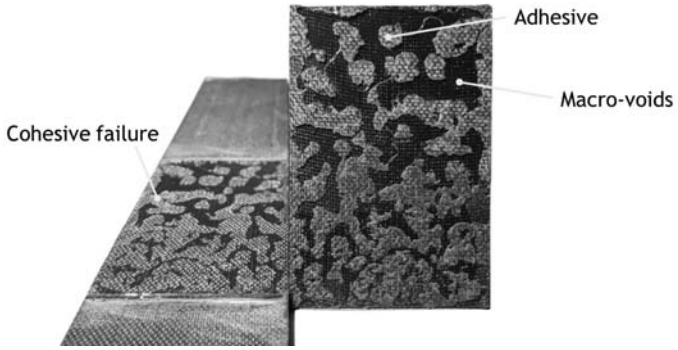

Figure 83 – Typical fracture surface of the peel ply treated specimens.

As a conclusion, it is possible to assume that the higher the load carrying capacity of the bonded joint, the higher the predominance of inter/intra/translaminar failure of the CFRP skin. Particularly for the peel ply treated specimens, which had the worst performance of all specimens, the fracture surfaces indicate 100% cohesive failure. Therefore, it is possible to do a correlation between the area covered with macro-voids and the maximum load of the joint: the higher the area of macro-voids, the less is the maximum load of the joint. The best results were found for the specimens abraded with 240 grit sandpaper.

The CFRP stiffener stays undamaged for all specimens, only with adhesive and/or skin's delaminated plies left embedded on its surface.

4.2.2. Influence of the Joint Fabrication Method

The results from the different methods of fabricating the joint and curing the adhesive are presented in Figure 84 in the format of a chart bar. Table 16 presents, once again (with the purpose of better convenience), the nomenclature of each specimen and the corresponding adhesive curing procedure.

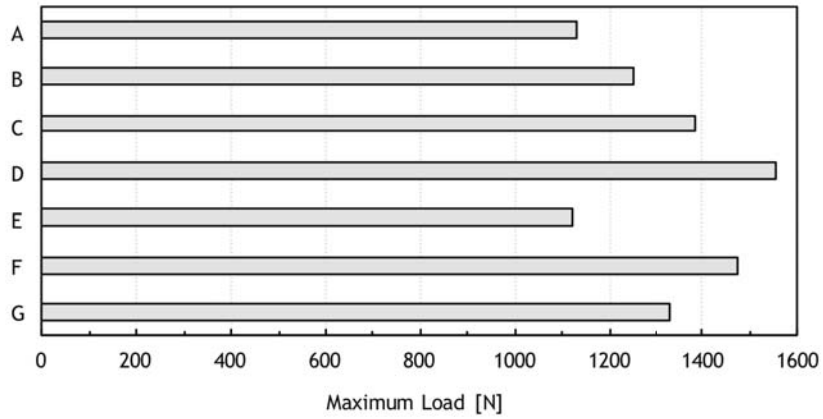

Figure 84 – Maximum load values for differently cured skin-to-stiffener joints.

Table 16 – Correlation between the specimen nomenclature and the curing method used.

Specimen's nomenclature	Number of adhesive films	Fibreglass carrier	Pressure	Vacuum release	Particles addition
A	2	No	No	No	No
B	4	No	No	No	No
C	4	Yes	No	No	No
D	4	Yes	5 bar	No	No
E	4	Yes	No	Yes (120 °C)	No
F	4	Yes	5 bar	Yes (120 °C)	No
G	4	No	5 bar	No	Cork

From the examination of the graph in Figure 84, particularly when comparing the specimens A, B, and C with the specimen E, it is possible to conclude that dismissing the "vacuum release" technique – which was assumed to be the cause of the large voids – and only the adhesive while performing a temperature cycle, was effective in increasing the maximum load capacity of the joint, presumably due to minimization of the voids. However, from the inspection of the

fracture surfaces (Figure 85), some small voids were still visible. The failure mechanism of the adhesive has moved from cohesive to adhesive, clearly identified by the layer of adhesive on the stiffener's surface. There were also 0º fibres embedded in the adhesive, resulting from inter/intra/translaminar failure of the CFRP skin. A similar fracture surface was found for the specimens A and C, which were cured under the same conditions (without pressure or "vacuum release") but using only two layers of adhesive or using four layers with a fibreglass carrier, respectively. Among these three specimens, the best results were obtained to the specimen C, which used the fibreglass carrier and four layers of adhesive.

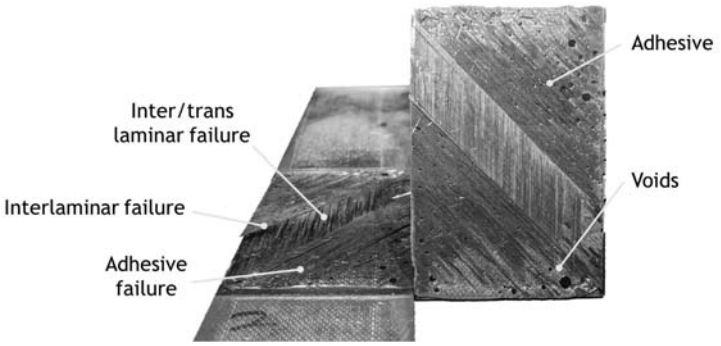

Figure 85 – Typical fracture surface of the specimens A, B and C.

When performing the "vacuum release" technique with the fibreglass carrier, the fracture surface (Figure 86) is fairly different from before (Figure 82), this time exposing the glass fibres at the location of the macro-voids. The failure mechanism was almost uniquely cohesive, but some residual inter/translaminar failure was also found in the CFRP skin.

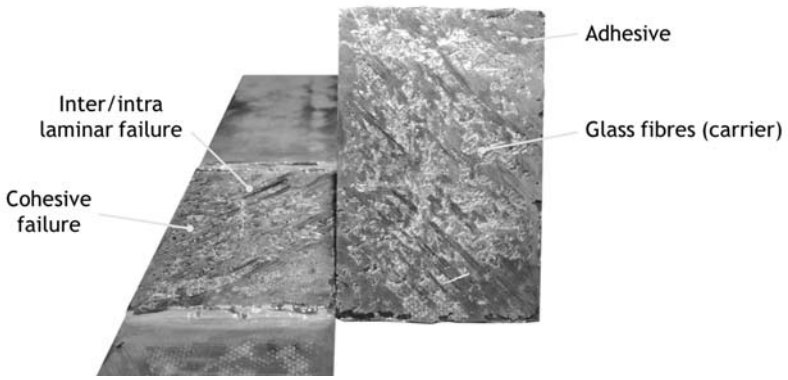

Figure 86 – Typical fracture surface of the specimen E.

The application of pressure was found to be very successful in terms of macro-void minimization. All specimens cured under 5 bar of pressure (D, F, G) exhibited very similar fracture surfaces (Figure 87) among them, but optimal results – both in terms of mechanical performance and uniform adhesive bondline – were found for the specimen D, which was cured using four layers of adhesive, a fibreglass carrier, and a hydrostatic pressure of 5 bar inside the

autoclave without using the “vacuum release” technique. The most probable cause for the poor performance of the specimen G is from the excessive percentage of cork (~11%) in terms of mass fraction of the uncured adhesive.

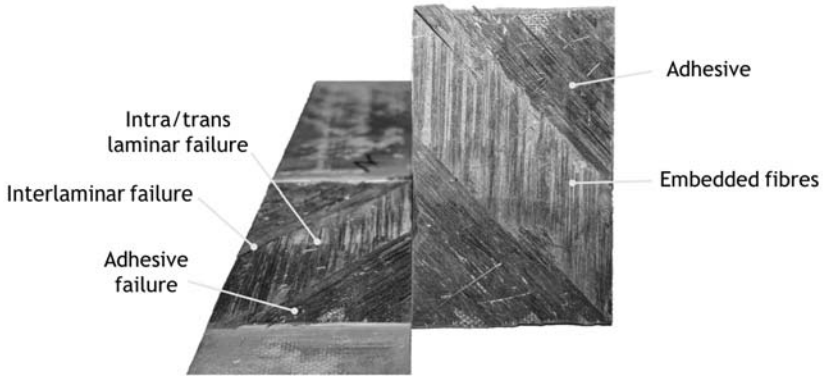

Figure 87 – Typical fracture surface of the specimens D, F and G.

Furthermore, the use of a carrier and duct tape (as an exterior barrier to avoid release of adhesive during its cure) has proved very efficient in controlling the bondline thickness and uniformity. It was confirmed that the “vacuum release” technique was associated with a tendency to macro-void formation. Interestingly, the specimen E, cured using the vacuum release and without pressure, was the only specimen that failed under cohesive failure of the adhesive, leading to the worst results in terms of maximum load. All the other specimens exhibited adhesive failure and some degree of inter/intra/translaminar failure.

4.2.3. Influence of the Noodle Design

The stiffener pull-off test results for the different noodle designs are listed in Tables 17, 18, and 19, in terms of load, displacement, and stiffness: at maximum load, failure load, and crack initiation, respectively.

Table 17 – Stiffener pull-off results: maximum load P_{max}, displacement at maximum load $\delta_{P_{max}}$, stiffness at maximum load $K_{P_{max}}$ (average $\pm$ relative standard deviation).

	P_{max} (N)	$\delta_{P_{max}}$ (mm)	$K_{P_{max}}$ (N/mm)
Std_fibres	1722 $\pm$ 13%	1.3 $\pm$ 15%	1369 $\pm$ 3%
Std_adhesive	1588 $\pm$ 13%	1.6 $\pm$ 39%	1073 $\pm$ 39%
Std_empty	1748 $\pm$ 7%	2.6 $\pm$ 11%	673 $\pm$ 7%
Tool_empty	2012 $\pm$ 6%	3.3 $\pm$ 24%	637 $\pm$ 18%
Tool_adhesive	1982 $\pm$ 7%	2.7 $\pm$ 42%	834 $\pm$ 48%

Table 18 – Stiffener pull-off results: failure load P_{fail}, displacement at failure load $\delta_{P_{fail}}$ and stiffness at failure load $K_{P_{fail}}$ (average $\pm$ relative standard deviation).

	P_{fail} (N)	$\delta_{P_{fail}}$ (mm)	$K_{P_{fail}}$ (N/mm)
Std_fibres	1209 $\pm$ 22%	2.8 $\pm$ 14%	430 $\pm$ 12%
Std_adhesive	1123 $\pm$ 9%	3.1 $\pm$ 1%	361 $\pm$ 8%
Std_empty	1607 $\pm$ 19%	3.2 $\pm$ 10%	506 $\pm$ 26%
Tool_empty	1932 $\pm$ 9%	3.9 $\pm$ 7%	498 $\pm$ 7%
Tool_adhesive	1629 $\pm$ 24%	3.6 $\pm$ 13%	447 $\pm$ 13%

Table 19 – Stiffener pull-off results: crack initiation load P_{init}, displacement at crack initiation $\delta_{P_{init}}$ and stiffness at crack initiation $K_{P_{init}}$ (average ± relative standard deviation).

	P_{init} (N)	$\delta_{P_{init}}$ (mm)	$K_{P_{init}}$ (N/mm)
Std_fibres	1722 $\pm$ 13%	1.3 $\pm$ 15%	1369 $\pm$ 3%
Std_adhesive	1583 $\pm$ 13%	1.3 $\pm$ 13%	1236 $\pm$ 12%
Std_empty	1600 $\pm$ 6%	1.4 $\pm$ 9%	1126 $\pm$ 4%
Tool_empty	1450 $\pm$ 14%	1.5 $\pm$ 9%	981 $\pm$ 8%
Tool_adhesive	1548 $\pm$ 18%	1.4 $\pm$ 10%	1137 $\pm$ 14%

However, differently from what happened in the previous tests, in these tests, the point at maximum load did not necessarily correspond to the failure load. The main reason for this is presumably the large increase in stiffness caused by the decreased skin span (185 mm to 100 mm). When compared to the stiffness values in Table 15 and 17 in terms of stiffness at maximum load, there was a 17 times increase in stiffness only by decreasing the span by 85 mm.

From the analysis of Table 19 it is possible to notice that for the joints produced using the auxiliary tool, the crack usually initiated at smaller loads than for the other joints. However, once the crack has initiated, the damage tolerance of the redesigned joints was substantially higher, with an increase of the load-carrying capacity of up to 17% in terms of maximum load and 60% in terms of the failure load (Figure 88), when compared to the standard joints filled with 0º fibres (Std_fibres). They were also able to withstand higher deflections of the skin until failure. Crack initiated at approximately the same displacement for all the specimens (between 1.3 and 1.5 mm).

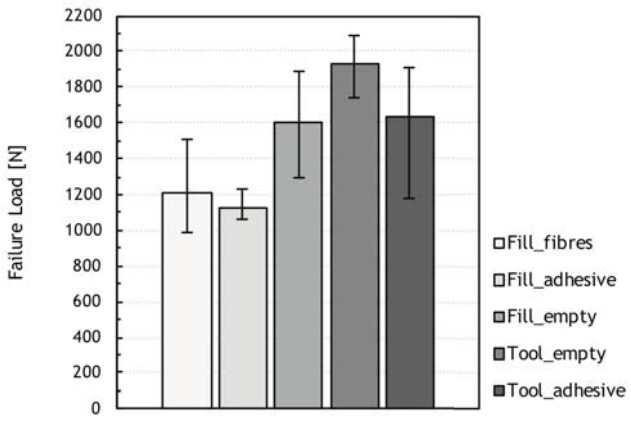

Figure 88 – Failure load.

The introduction of the adhesive in the noodle after using the auxiliary tool seems to have no benefit in the performance of the joint, both at the maximum and failure loads.

In terms of stiffness, the results are difficult to interpret, as different tendencies were found whether it was calculated at the crack initiation, maximum load, of failure load. However, it seems that generally the stiffness is typically lower for the specimens without noodle filling (Std_empty and Tool_empty) – except at the failure load – presumably because the empty space in the noodle has allowed for a higher deformation of the stiffener (as confirmed by the increased displacement values). The highest values of stiffness (at maximum load and crack initiation load) were obtained for the specimens filled with unidirectional fibres (Std_fibres), as it results in the most rigid stiffener (with higher fibre content).

As for the joints produced without using the auxiliary tool (standard scenario), it was interesting to conclude that the series which performed the best were the joints whose noodle was left empty (later filled with the prepreg resin during its cure). This is presumably caused by the different stiffness of the stiffener specimens, particularly in the noodle region, causing a different loading distribution in the joint. Another plausible cause for these deviations is from manufacturing deviations and defects, particularly in the stiffeners without filling material (Std_empty) or filled with adhesive prior to their cure (Std_adhesive). It was found that these specimens exhibited considerable defects such as fibre twisting (Figure 89a) and rich-resin regions (Figure 89b).

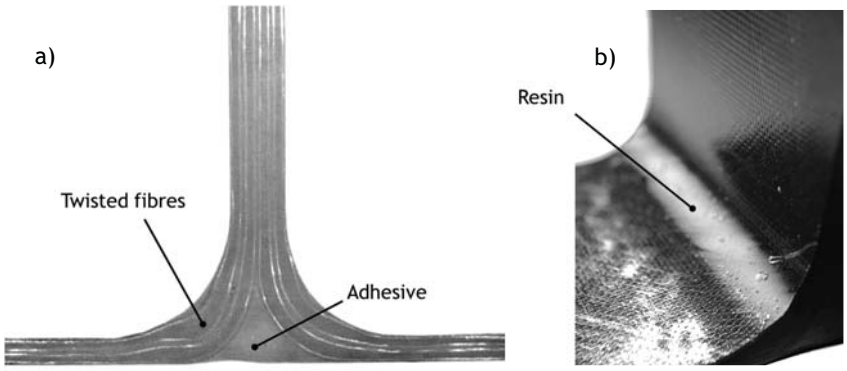

Figure 89 – Manufacturing-induced defects on specimens filled with adhesive: a) Fibre twisting; b) Resin-rich regions.

After the final failure of the skin-to-stiffener joints, there was still an amount of load being carried, and complete detachment could only be achieved by further pulling of the stiffener. This occurred as a sequence of fibre bridging (Figure 90) between the stiffener and the skin, which is one of the most frequent features of mode I fracture [35].

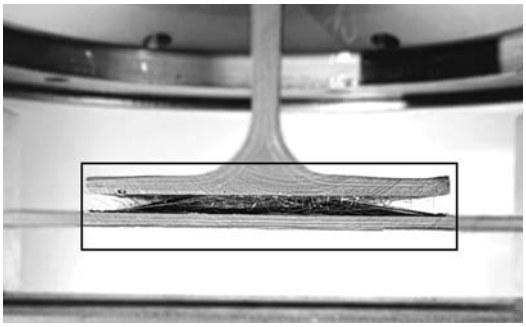

Figure 90 – Fibre bridging.

Besides the **type I** failure sequence already described in the subsection 4.2.1, three more types of failure sequences can be distinguished:

The failure sequence **type II** (Figure 91) is similar to type I, but in this case there is only one crack propagation, which initiated at one side of the stiffener flange and propagates towards the opposite end of the stiffener.

In both this failure sequence types, **I and II**, the abrupt geometry step (plus the possibility of resin-rich or poor consolidation regions) of the tip of the stiffener flange act as a local high stress concentration zone, leading to crack initiation. Under the quasi-static tensile loading, with the increased bending of the skin, the stiffener is too stiff to keep up with that deflexion, and the crack initiates through the development of peel stresses at the tip, which is the zone with higher stress concentrations (Figure 11b). The stiffener stays intact even after final failure. There is no relation between the occurrence of type I or II failure sequences and the maximum load value.

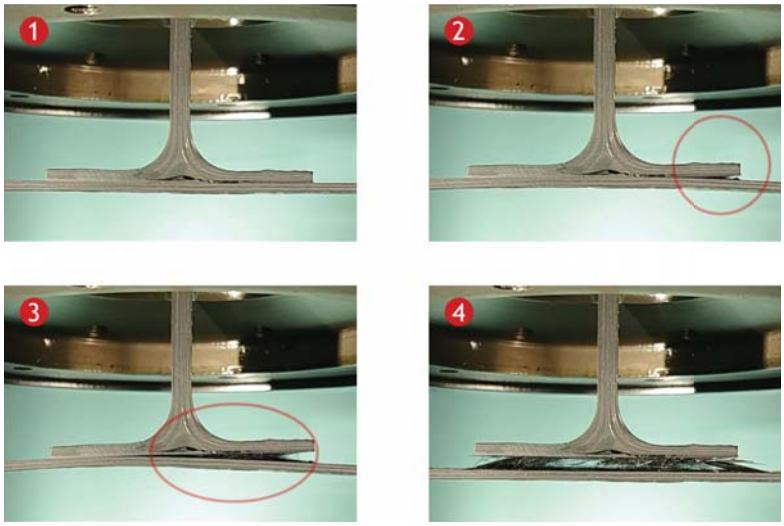

Figure 91 – Type II failure sequence on specimen "Std_adhesive": 1) Starting point; 2) Crack initiation; 3) Crack propagation; 4) Detachment from the skin.

In the failure sequence **type III** (Figure 92), failure initiated in the noodle region, spreading towards the top of the stiffener web. As the bending increases, two new cracks initiate almost simultaneously at the adhesive bondline, propagating from the centre (noodle) towards the tips. When the cracks reach the tips of the stiffener, final failure occurs and the stiffener detaches from the skin.

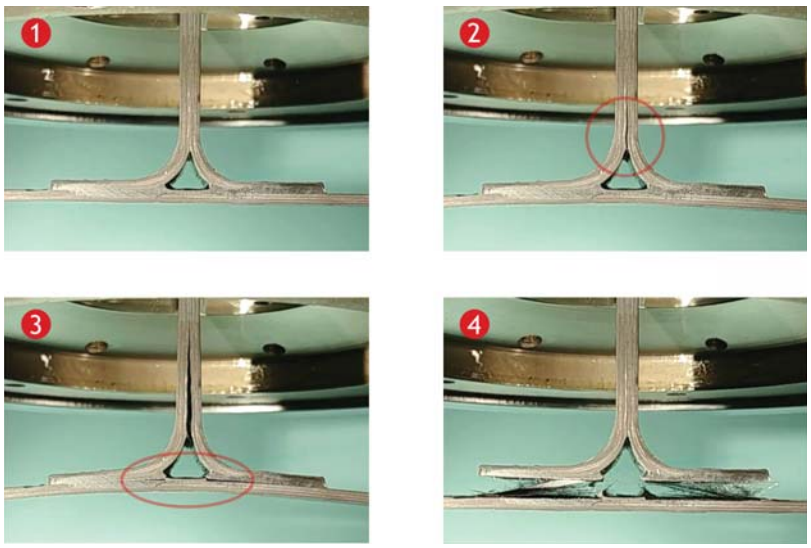

Figure 92 – Type III failure sequence on specimen "Tool_empty": 1) Starting point; 2) Crack initiation; 3) Crack propagation; 4) Detachment from the skin.

In the failure sequence **type IV** (Figure 93), the course of events is similar to type III, but because the noodle is filled with the adhesive, the failure propagates towards the top of the stiffener web but also along the curvature of the noodle and the transversally in the adhesive

filling, by means of multiple cracks that reach the adhesive bondline and then extend from the centre to the stiffener flanges' tips.

In both these failure sequence types, **III and IV**, the crack indicated at the noodle, and not on the tip of the stiffener, probably because the redesign of the noodle has caused a different stress distribution along the joint. Again, it can be assumed that this is because the stiffener is less stiff, allowing it to deform in the noodle region, and increasing by up to 40% the maximum displacement of the joint when compared to the standard joint filled with 0º fibres.

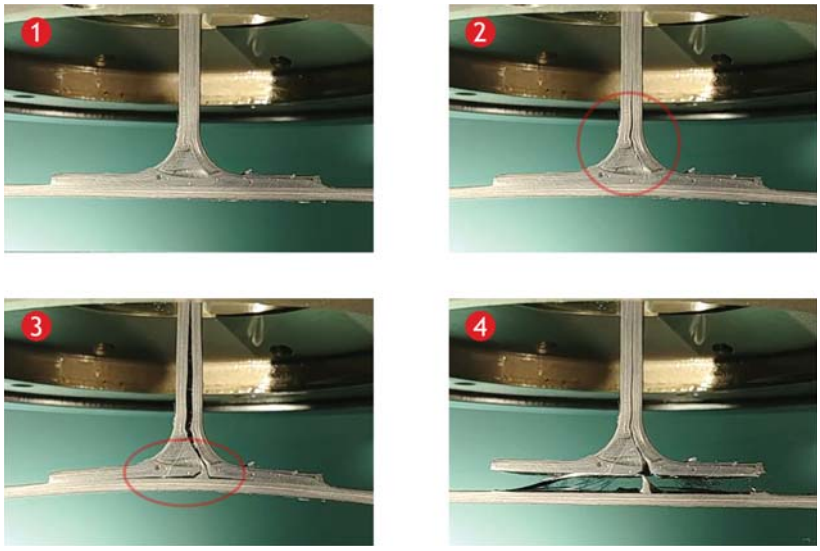

Figure 93 – Type IV failure sequence on specimen "Tool_adhesive": 1) Starting point; 2) Crack initiation; 3) Crack propagation; 4) Detachment from the skin.

Figure 94 illustrates a typical load-displacement ($P-\delta$) curve for each type of failure sequence.

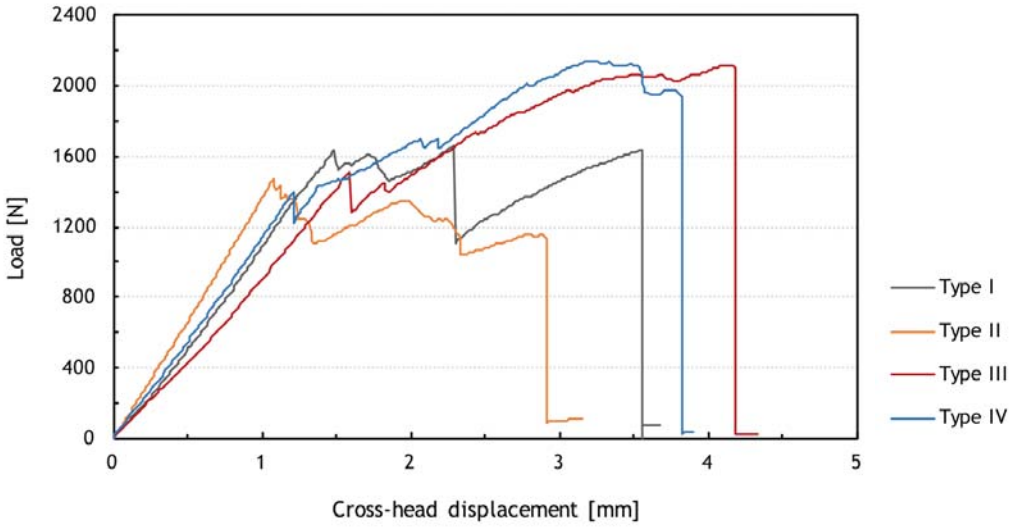

Figure 94 – Typical load-displacement curves for the different types of failure sequence.

Table 20 makes the correlation between the specimens' series and the type of failure sequence observed.

Table 20 – Correspondence between specimen series and the observed failure sequence type.

Specimen series	Failure sequence
Std_fibres	Type I (1/3) and Type II (2/3)
Std_adhesive	Type II (3/3)
Std_empty	Type I (1/3) and Type II (2/3)
Tool_empty	Type III (3/3)
Tool_adhesive	Type IV (2/3) and Type II (1/3)

In type III and IV failure sequences, the failure initiates within the noodle region and propagates upwards through the stiffener web. One problem that has been identified in these specimens is the waviness of the laminate, especially above the noodle region (Figure 95). This defect has been induced during the manufacture of the stiffener possibly due to insufficient consolidation and the gravity effect that, when at a fluid state of the resin, caused a drop of the laminate layers, leading to the formation of wrinkles. This defect could act as an initiation site for failure and induce premature delamination between the composite layers. A simple solution to this problem could have been by using the tools upside down, this way using the force of gravity to guarantee that the stiffener's web layers stay straight during the cure of the composite.

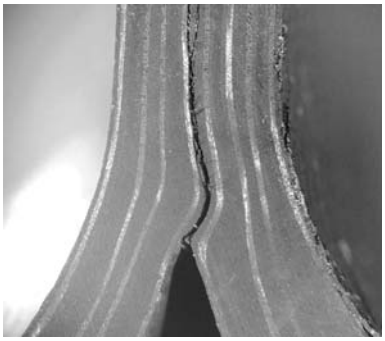

Figure 95 – Manufacture-induced waviness along the stiffener's web.

When examining the fracture surfaces, the specimens that failed according to the failure sequence type I and II had very similar surfaces (Figure 96), with the adhesive being left on the stiffener's foot, where it was possible to observe some embedded fibres as a result from interlaminar and translaminar failure of the skin laminate. Loose fibres were also found in both surfaces that might have originated from the intensive fibre bridging.

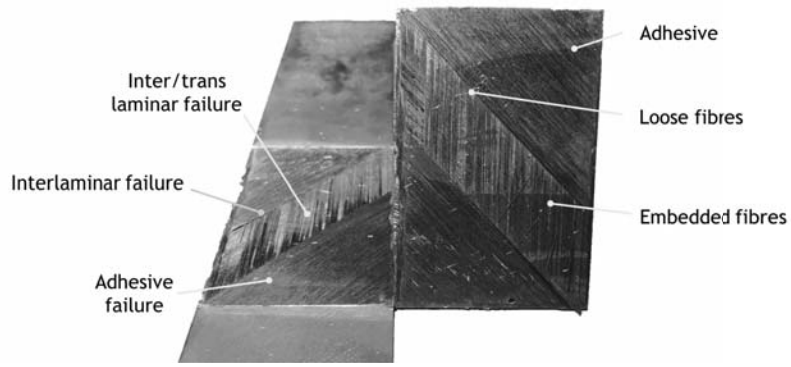

Figure 96 – Typical fracture surface of types I and II failure sequences.

On the specimens from the "Tool_empty" series, all failed under the sequence type III (Figure 97), it was clearly visible the adhesive left on the stiffener's flanges, but also on the skin in the noodle region. Interlaminar and intralaminar failure occurred in the skin laminate.

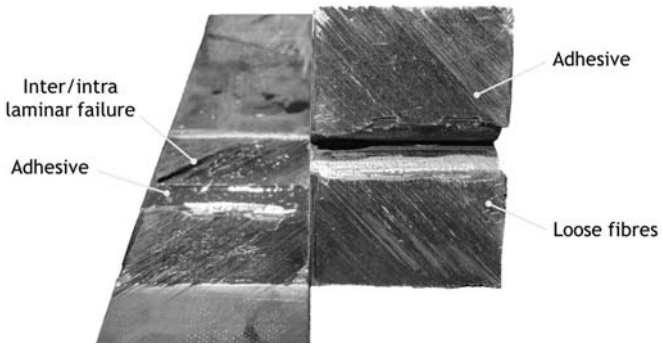

Figure 97 – Typical fracture surface of type III failure sequence.

Similarly, the specimens from the "Tool_adhesive" series which failed under the sequence type IV (Figure 98) exhibited adhesive failure with inter/intralaminar failure of the skin, but the adhesive used as noodle filling was found on both surfaces of the skin and the stiffener.

The fracture surfaces morphologies were consistent within the same type of failure sequence.

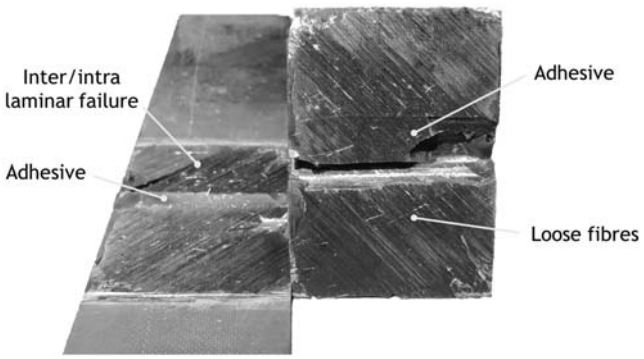

Figure 98 – Typical fracture surface of type IV failure sequence.

As a summary, types III and IV of failure sequence – which occurred on specimens where the auxiliary tool was used – were associated with joints with decreased load values at the crack initiation, but very successful on sustaining higher loads until the final failure. This means that the damage tolerance (the ability to sustain defects safely until a repair can be made) of these joints is considerably higher, and this is a very important aspect to consider during the design of aerospace structures. It is presumed that this increase in the damage tolerance was possible by a more uniform load distribution within the joint and reduction of the peak peeling stresses, thanks to the empty space in the noodle that has resulted in a less stiff joint. It was also noticed that the use of the 0º prepregged fibres had no benefit in increasing the SPOT performance of the joint, mainly because of two reasons: The composite noodle is primarily loaded in through thickness stress and there are no fibres in that direction; and secondly, when cooling down upon manufacturing of the T-shaped carbon composite, the fibres in the noodle region do not allow the resin to shrink, resulting in very high residual stresses in the matrix at that location [13].

The use of the auxiliary tool was also very effective on reducing the manufacture-induced defects like twisted fibres and excess resin, as previously reported in the literature [21] and also noticed during the development of this project (Figure 89). It was later found that it was not possible to fully eliminate the wrinkling effect (Figure 95), but it is believed that it would be completely avoided if the tooling setup was placed upside down to counteract the gravity. Furthermore, up to a 15% decrease in terms of weight of the stiffener can be achieved by using the auxiliary tool (without filling material), with the additional benefit of reduced material costs.

4.3. Fractographic Analysis

As mentioned in Chapter 3, the specimens had to be dissected into smaller sections for analysis using SEM. Following the previous conclusions regarding the failure sequence, three different locations were chosen for examination:

Location 1, at the area of crack initiation at the tip of the stiffener's flange (in the case of types I or II) or the crack propagation region if the crack initiated from the noodle (types III or IV) or initiated from the opposite side of the stiffener (type II);

Location 2, along the curvature of the noodle and to the crack propagation region in the stiffener's web.

Location 3, at the area of crack initiation or propagation along the stiffener's flange, equivalent to the location 1 but at the opposite side.

For locations 1 and 3, both matching fracture surfaces were exposed and analysed, however one contained many fibres and few fibre imprints (the lower face, on the skin), and the other was almost entirely covered with the adhesive with the matching fibre imprints (the upper face, on the stiffener).

Following the same procedure as for the macroscopic analysis of the fracture surfaces, the analysis of the microscopic morphologies was made by using some characteristic features of micrographs taken at different locations within the specimen. Only the specimens used to compare different noodle designs were observed using SEM, and consequently they will be the basis for further conclusions on the failure mechanisms taking place.

The failure sequence was already possible to infer from the experimental testing observations, as mentioned in the previous section. Once again, four different types of failure sequences can be distinguished, as illustrated in Figures 99 through 102:

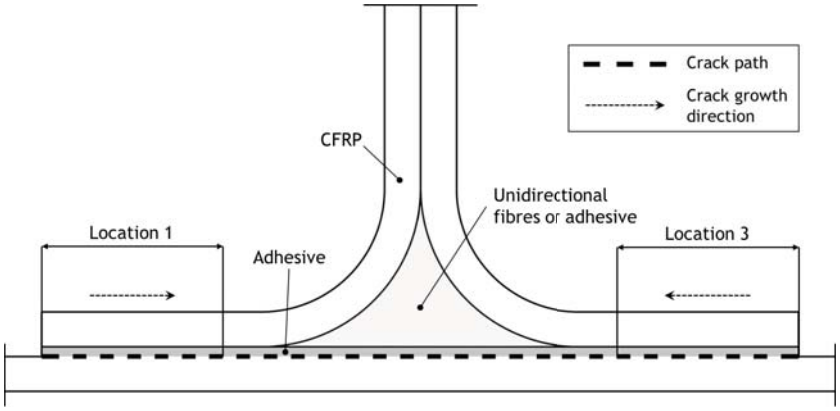

Figure 99 – Failure sequence type I.

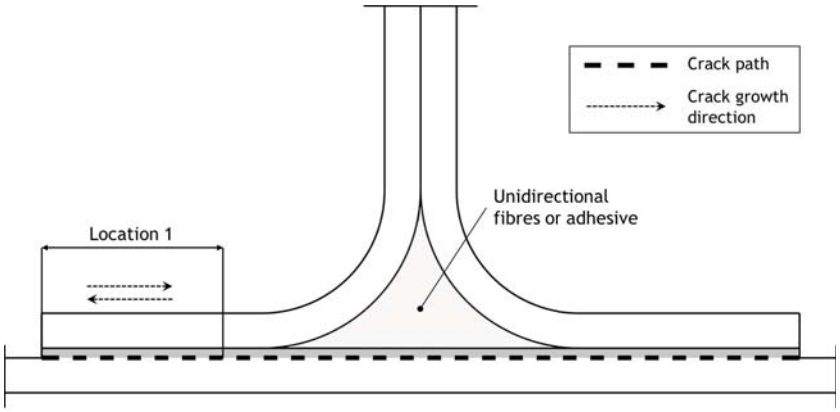

Figure 100 – Failure sequence type II.

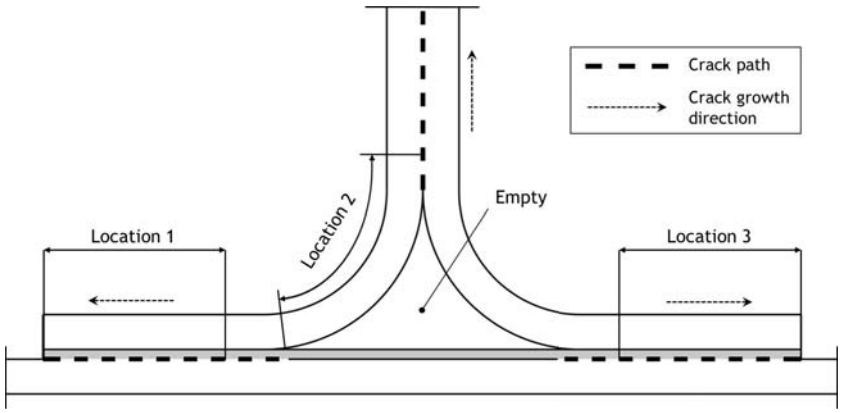

Figure 101 – Failure sequence type III.

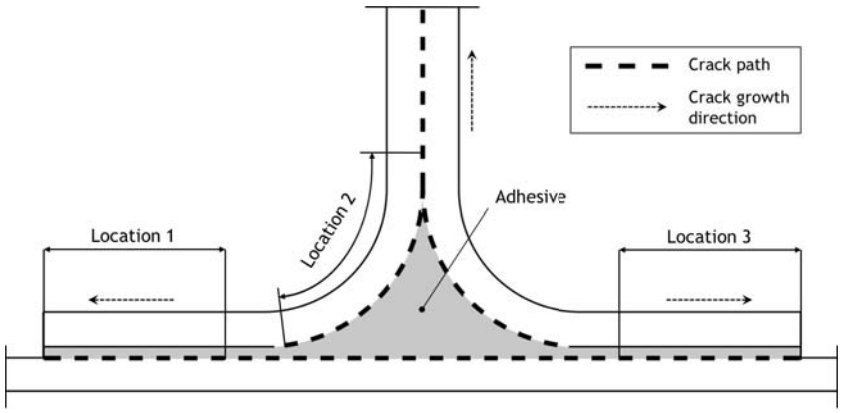

Figure 102 – Failure sequence type IV.

From a first SEM micrograph on the "as fractured" surface using a low magnification at the intersection between the first (-45º) and second (0º) plies, SEM analysis (Figure 103) allowed to confirm the previous observations of the coexistence of the three types of laminar fracture (interlaminar, intralaminar, and translaminar). The interaction between these different fractures types is an important factor in the behaviour of composites, being more thoroughly analysed using higher magnifications.

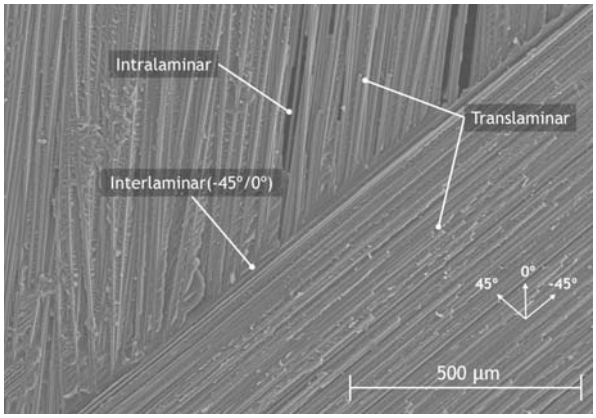

Figure 103 – Top view at the interception between the first (-45º) and second (0º) plies of the skin of specimens failed by sequence types I or II. SEM micrograph using a magnification of ×100.

Translaminar and intralaminar failure were more evident in the second ply (0º), possibly due to the interaction between successive intralaminar fractures (which tend to develop early in the damage development) and translaminar fractures [35].

Translaminar failure can be identified by the longitudinal splitting of the fibres and is essentially driven by a change in the direct stress across the width of a ply, thus inducing an in-plane shear loading within this ply. One of the most probable causes for this occurrence is from the fibre bridging between the CFRP skin's fibres and the adhesive, as it was clearly visible after debonding (Figure 90).

Intralaminar failure is recognisable by the "separation" between the second ply's fibres, where the matrix and fibre/matrix interfaces have been broken.

Interlaminar (delamination) between the first (-45º) and second (0º) plies is easily identified by the exposed second ply and the different fibre orientations at the interface (diagonal), where the two layers meet. According to Greenhalgh and Hiley [122], this failure type occurs because shear stresses orientated such that the delamination migrated into the skin laminate until it reached a -45º/0º interface, at which it remained because de 0º layer is aligned with the driving force.

From a closer examination it was possible to see that there was a significant amount of debris particles on the fracture surface (Figure 104), which sometimes made interpretation of the fracture morphology problematic. In the same figure, the broken fibre ends (translaminar failure) are clearly visible, as well as intralaminar failure from the fibres that were completely exposed after they separated from the matrix.

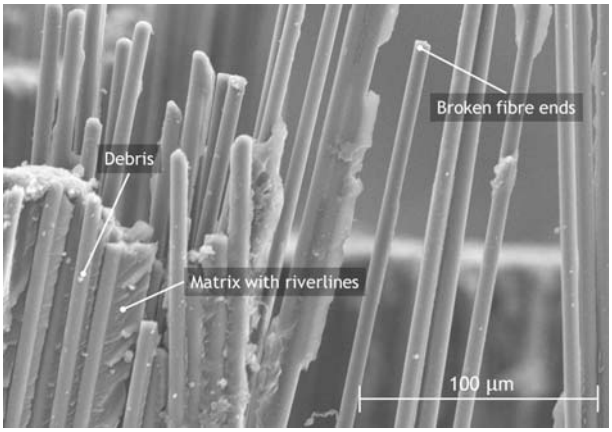

Figure 104 – Detail of intralaminar and translaminar failure of specimens with type I or II failure sequence. SEM micrograph using a magnification of ×500.

Starting from the tip of the stiffener's flange, at the location 1 of the specimens failed by the type I and II failure sequences, the first layers of the skin exhibited very little deformation of the matrix, which is a characteristic of rapid crack growth in brittle matrices. In these

materials, typical fractographic features such as textured microflow, riverlines and scarps can often be clearly observed. In fact, from further examination of the fracture surface using higher magnifications (Figure 105), it was possible to identify the presence of scarps and riverlines, which are features of a typical failure mode I morphology. Scarps form from the convergence between two adjacent crack planes, forming a sharp step [35].

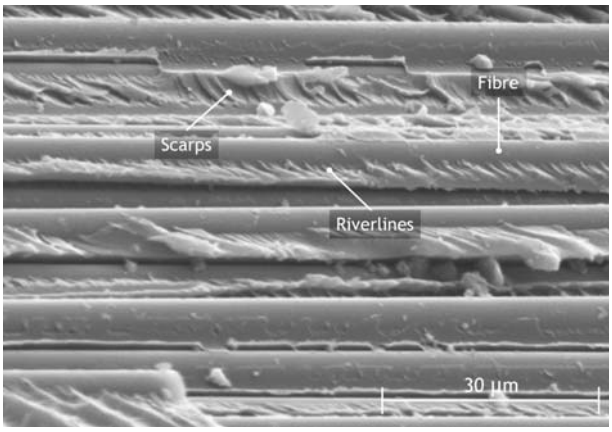

Figure 105 – Fractured surface features of specimens failed by sequence type I or II. Image taken at the tip of the skin (Location 1, -45º ply). SEM micrograph using a magnification of ×1500.

Moving towards the centre of the specimen (Figure 106), closer to the noodle, the second ply (0º) exhibited mixed mode I/II failure by the presence of sharp cusps and serrated feet, both of which are typical features of mixed mode fracture. Cusps appear as inclined platelets on the surface, while serrated feet develop from multiple micro-cracks at the edges of the cusps, which merge as the centre of the cusp is approached. It is also possible to observe the excellent quality of the interface between the fibres and matrix.

With the introduction of the failure mode II, the matrix surface becomes dominated by upright cusps, and fracture tends to develop closer to the fibre/matrix interface, leading to more bare fibres being evident.

These findings are in accordance with the observations already stated in the literature [35], expressing that despite initiating as a mode I fracture, as the fracture extends along the flange, the mode II component increases.

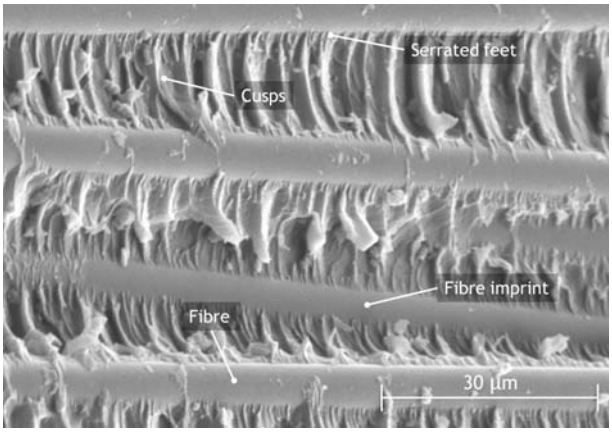

Figure 106 – Fractured surface features of specimens failed by sequence type I or II. Image taken near the centre of the skin (Location 1, 0º ply). SEM micrograph using a magnification of ×1500.

In the location 1 of the specimens failed by type III sequence ("Tool_empty" series), the skin's surface exhibited some similar features of mixed mode failure (Figure 107), but this time with increased angle of the cusps. According to Greenhalgh [35], there is a relationship between the cusp angle and the mode mixity (G_I/G_{II}): the higher the mode II component, the higher the value of the cusp angle. Therefore, it can be deduced that in this case the mode II is considerably more dominant (75-100%, by comparison with images from the literature).

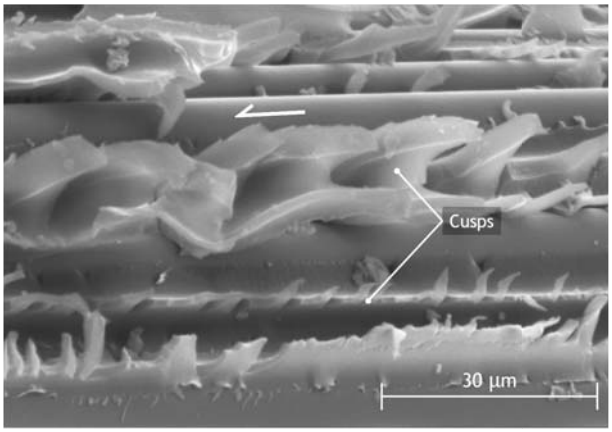

Figure 107 – Fractured surface features of specimens failed by sequence type III. Image taken at the skin's left side (Location 1, -45º ply). SEM micrograph using a magnification of ×1500.

Furthermore, it is possible to depict the shear direction from the cusps' orientation. As illustrated in Figure 108, if the cusps are leaning towards the left, the shear direction is from left to right; and vice-versa. Because the specimens were tilted to 60º prior to SEM observation, it can be very clearly seen that in this case, the shear direction is from right to left.

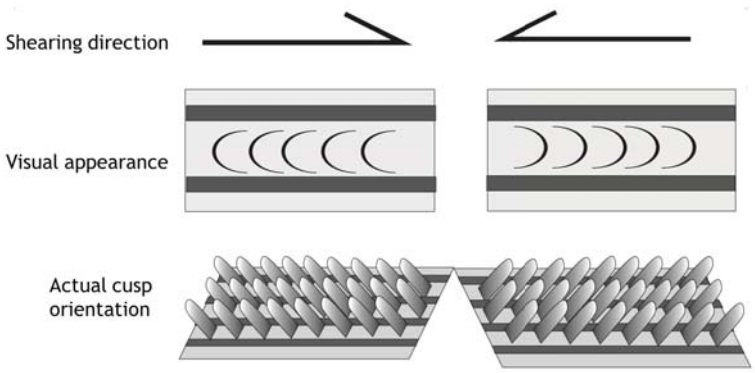

Figure 108 – Visual appearance of cusps and corresponding shear direction. Adapted from [35].

From the inspection of the location 3 (at the opposite side of the skin), the cusps exhibited an inverse orientation (Figure 109), which is in accordance with the crack propagation direction and failure sequence observed during experimental testing (Figures 92 and 101): the crack, as well as the relative shear direction on the skin, moves from the noodle region towards the tips of the stiffener flanges.

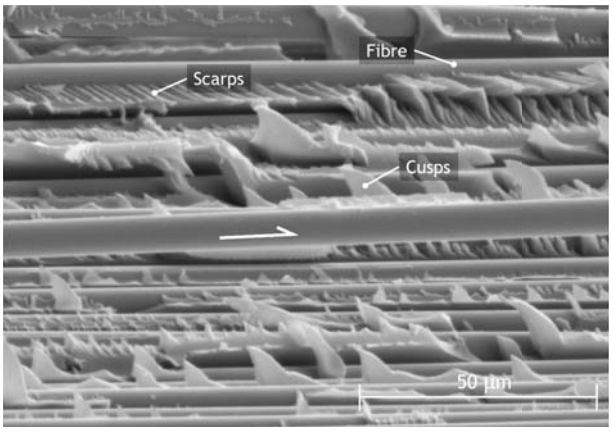

Figure 109 – Fractured surface features of specimens failed by sequence type III. Image taken at the skin's right side (Location 3, -45º ply). SEM micrograph using a magnification of ×1000.

From the upper surface (stiffener's foot), also at the location 3, the fracture surface is almost entirely covered with adhesive (Figure 110), with imprints of the matching (lower surface) fibres. Between the fibres imprints, the adhesive is highly deformed, exhibiting sharp and angled cusps. As expected, the cusp orientations oppose the ones found on the matching side (at the skin, Figure 109), providing an indication of the relative shearing directions of the two surfaces.

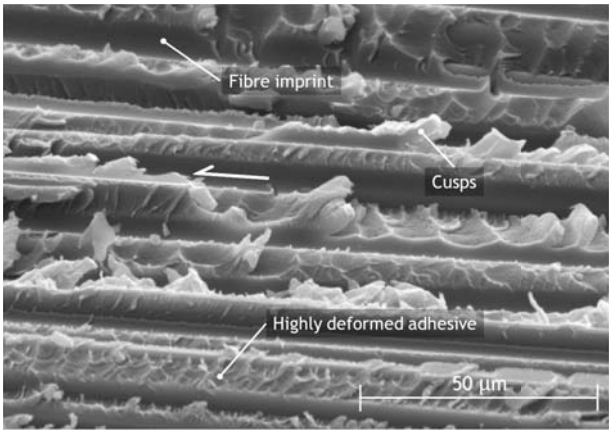

Figure 110 – Fractured surface features of specimens failed by sequence type III. Image taken at the stiffener's right flange (Location 3, -45º ply). SEM micrograph using a magnification of ×1000.

Besides, from a higher magnification inspection (Figure 111), the adhesive exposed some very small voids (less than 1 μm in diameter). This adhesive porosity can act as a local weakness and cause a reduction in its mechanical properties, and can also act as a route for corrosion or moisture ingress into a laminate and thus degrade the load-bearing layers.

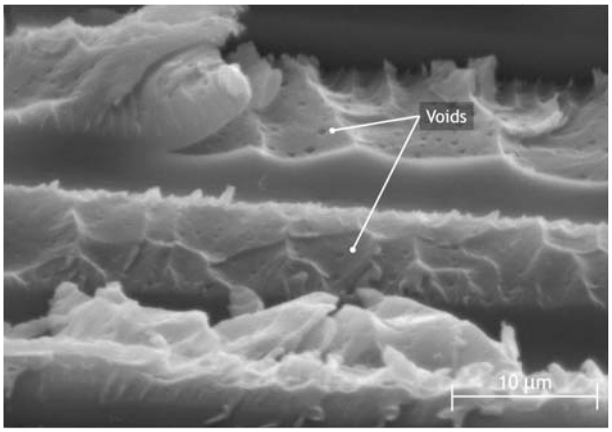

Figure 111 – Detail of the presence of voids on the adhesive fractured surface in specimens failed by sequence type III. Image taken at the stiffener's right flange (Location 3, -45º ply). SEM micrograph using a magnification of ×3000.

In the location 2, near the noodle region of one of the specimens failed by type III sequence, the adhesive left on the skin's surface unveiled a large macro void (Figure 112), from which it was possible to see extensive splitting of the randomly oriented glass fibres used as a carrier during the adhesive's cure. There was also some adhesive that extended into the laminate surface, where riverlines and textured microflow can be identified, which again are prevalent in brittle epoxy systems.

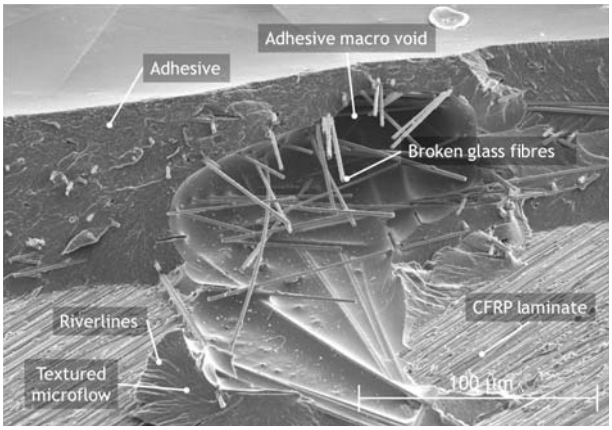

Figure 112 – Detail of a large void found at the adhesive bondline on specimens failed by sequence type III. SEM micrograph taken at the skin (Location 2, -45º ply) using a magnification of ×50.

At the location 3 of the same specimen, on the tip of the stiffener flange, it was macroscopically possible to identify a saw-tooth morphology, which at closer examination exhibited a stepped fracture of the adhesive (Figure 113). This type of fracture is a feature of in-plane shear failure, and considering the type of failure sequence and its location, it probably occurred at the final failure stages through mode II crack propagation from the centre of the stiffener. Aiding to this theory, from the analysis of the riverlines and the textured microflow from which they have developed, it is possible to infer the direction of the crack growth (indicated by the arrows), which is the direction in which the riverlines converge.

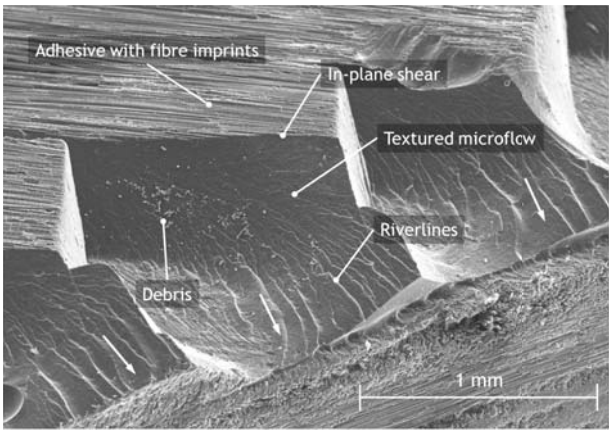

Figure 113 – Detail of a saw-tooth morphology on specimens failed by sequence type III. SEM micrograph taken at the stiffener (Location 3, -45º ply) using a magnification of ×50.

In location 2, at the stiffener's web, both the specimens failed by type III and IV sequences showed similar fracture surfaces (Figure 114), with scarps and riverlines being easily identified in the resin matrix, which are once again characteristic features of mode I dominated failure.

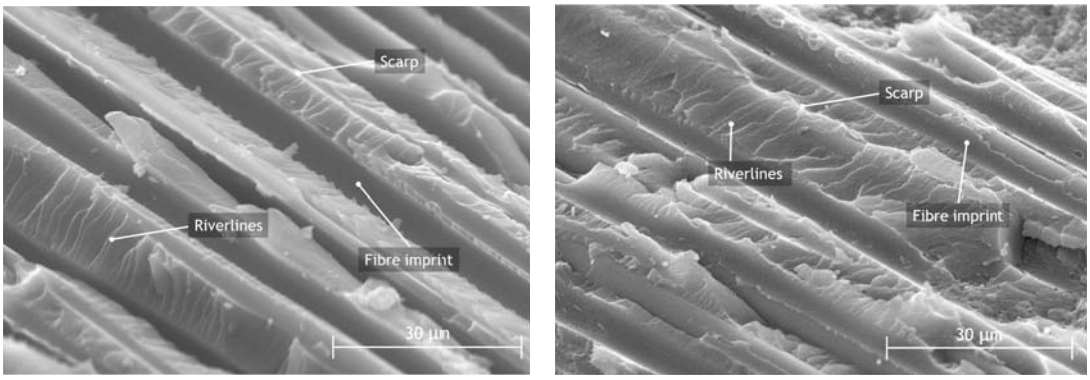

Figure 114 – Fractured surface features of specimens failed by the sequence: a) Type III; b) Type IV. SEM micrographs taken at the stiffener's web (Location 2, -45º ply) using a magnification of ×1500.

Finally, another noteworthy observation is the granular structure of the adhesive used as a noodle filler (failure sequence type IV), from which it was possible to depict a flow direction (Figure 115), indicating a direction of the fracture growth – starting from the noodle and moving upwards towards the stiffener web. Once again, the texture microflow is a characteristic that confirms the brittle nature of the adhesive.

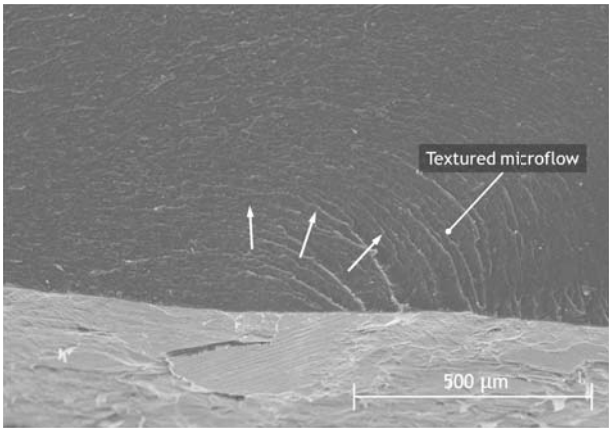

Figure 115 – Characteristic detail of the textured microflow found at the fractured adhesive on specimens failed by sequence type IV. SEM micrograph taken near the stiffener's noodle (Location 3) using a magnification of ×100.

As a summary of these microscopic observations, it is possible to say that the main failure mechanism undergoing at the disbond of the stiffener from the skin is mixed mode I/II delamination for all the specimens tested (including four types of failure sequences).

In the failure sequences type I and II, the crack initiates through the development of mode I peel stresses, but rapidly extends from the tip of the stiffener/skin interface towards the centre, promoting a redistribution of stresses within the joint and an increase of the mode II component. This phenomenon was already stated in the literature [35], but is even more obvious when comparing the SEM images at different locations of the skin (Figures 105 and 106), which at first exhibited the presence of scarps and riverlines (mode I morphology) and then

moved to a typical mode II predominant (mixed mode) fracture morphology, with shear cusps and serrated feet. It can also be noted that increasing the mode II component increases the degree of matrix deformation and total fractured area, which suggests a toughness increase with rising mode II component [122].

In the type III failure, damage initiates as mode I fracture within the noodle region and through the stiffener's web, but as the fracture extends along the flange, it does it under predominant mode II failure (Figure 107). Similar findings were made for the type IV failure (Figure 114b), with the additional observation that the failure propagates through the adhesive from the skin side towards the stiffener's web (Figures 114b and 115).

This page intentionally left blank

Chapter 5 – Final Remarks

Throughout this work, it was possible to create and develop a wide set of skills, from the study of the existing literature to the fabrication and experimental testing of bonded CFRP structures. The adopted step-by-step approach allowed to increase proficiency and overcome most of the difficulties found during the experimental part, from which it was possible to establish some important conclusions and suggestions for future work, as it will now be presented.

5.1. Final Conclusions

All the outlined objectives were successfully accomplished, and the following main conclusions can be drawn:

- Mechanical characterization of the bulk adhesive was made under some difficulties due to the formation of voids in the bulk specimens during their cure. Nevertheless, it was possible to conclude that the adhesive had a very brittle behaviour.
- Both the single lap and skin-to-stiffener joints were successfully produced. The fabrication procedure for the T-joints was published in the proceedings of the XVI Portuguese Conference on Fracture [123].
- Single lap shear tests were performed on five specimens, allowing for increased proficiency in manufacturing and testing adhesive joints. The evaluation of the different manufacture parameters was not conclusive due to the reduced number of specimens, as a consequence of the delamination found after water jet machining.
- The results from the surface characterization of the differently treated surfaces were useful in understanding the nature of the surface, but have not be shown to effectively predict the quality of bonding.
- Regarding the differently treated specimens, abrasion with 240 grit sandpaper was shown to be associated with the highest values of maximum load of the T-joint; while the peel ply has performed the worst, probably due to the fractured peaks of resin that were left on the surface after removing the peel ply layer. The fracture surfaces exhibited a considerable amount of macro-voids, which were associated with a lower joint strength. Failure was 100% cohesive for the peel ply treated specimens, but with the increase of the maximum load for the abraded and untreated specimens, intra/inter/translaminar failure of the CFRP skin was also visible.
- The optimal method for curing the adhesive was found to be using four layers of adhesive, a fibreglass carrier, and a hydrostatic pressure of 5 bar inside the autoclave. Some of the fracture surfaces exhibited very distinct morphologies depending on the curing method used.

- When evaluating the different designs of the stiffener noodle, it was found out that the usage of the auxiliary tool was very effective in increasing the damage tolerance of the cured T-joints, especially when no filler material is used; with the additional benefits of reducing the weight and material costs of the joint.
- Fractographic analysis confirmed that the main failure mechanism undergoing in the bonded skin-to-stiffener T-joint (when using a skin span of 100 mm) is mixed mode I/II delamination for all the types of failure sequences. Damage typically initiates as mode I fracture within the tip of the stiffener's flange (types I and II) or in the noodle region (types III and IV), but as the fracture extends along the stiffener's foot, it does it under predominant mode II failure.

5.2. Future Work

Considering that the results obtained when using the auxiliary tool were very satisfactory, resulting in a considerably higher damage tolerance of the T-joint, it seems logical that the next step should be to further pursue the validation and testing of this promising design alternative, particularly by performing a numerical modelling of the redesigned T-joint using finite element analysis. This is of vital importance not only to predict the reliability of these bonded structure, but also to use evaluate the performance of the joint under a variety of geometries (e.g. different noodle radius), materials (e.g. ductile adhesive) and loading conditions (e.g. fatigue), offering an important route to material optimisation. An accurate strength prediction of this joint is also essential to decrease the amount of expensive testing at the design stage, and expected to result in a more efficient use of composites and adhesives, lower structural weight, and lower material and manufacturing costs.

It is believed that the presented experimental work can serve as a good foundation for future numerical simulations of the behaviour of skin-to-stiffener T-joints, as it provides a very comprehensive description of the failure sequence, failure mechanisms and fracture modes, which can then be used and compared to when establishing the conditions for the numerical model. The materials used were also properly described, including the mechanical characterization of the bulk adhesive.

From an experimental approach, it would be interesting to find out if the performance of the joints and the failure mechanisms would be different using a different adhesive (more ductile), or by toughening the adhesive (increase ductility) using nano or micro-particles (e.g. rubber or cork), leading to smoother stress distributions along the adhesive layer and consequently better performance of the joints, as suggested in the literature.

References

[1] S. T. d. Freitas and J. Sinke, "Failure analysis of adhesively-bonded skin-to-stiffener joints: Metal–metal vs. composite–metal," *Engineering Failure Analysis,* vol. 56, pp. 2-13 , 2015.

[2] G. Scarselli, C. Corcione, F. Nicassio and A. Maffezzoli, "Adhesive joints with improved mechanical properties for aerospace applications," *International Journal of Adhesion and Adhesives,* vol. 75, pp. 174-180, June 2017.

[3] S. T. d. Freitas and J. Sinke, "Failure analysis of adhesively-bonded metal-skin-to-composite-stiffener: Effect of temperature and cyclic loading," *Composite Structures,* vol. 166, pp. 27-37, April 2017.

[4] W. G. Roeseler, B. Sarh and M. U. Kismarton, "Composite Structures: The First 100 Years," in *16th International Conference on Composite Materials*, Japan, 2007.

[5] F. Smith, "The Use of Composites in Aerospace: Past, Present and Future Challenges," Avalon Consultancy Services Ltd, 2016.

[6] A. Baker, S. Dutton and D. Kelly, Composite Materials for Aircraft Structures, Second edition ed., Reston, VA: Institute of Aeronautics and Astronautics, 2004.

[7] A. Higgins, "Adhesive bonding of aircraft structures," *International Journal of Adhesion & Adhesives,* vol. 20, pp. 367-376, 2000.

[8] M. Banea and L. da Silva, "Adhesively bonded joints in composite materials: An overview," *Proceedings of the Institution of Mechanical Engineers Part L Journal of Materials Design and Applications ,* January 2009.

[9] S. Budhe, M. Banea, S. de Barros, d. Silva and L.F.M., "An updated review of adhesively bonded joints in composite materials," *International Journal of Adhesion and Adhesives,* vol. 72, pp. 30-42, January 2017.

[10] C. Katsiropoulos, A. Chamos, K. Tserpes and S. Pantelakis, "Fracture toughness and shear behavior of composite bonded joints based on a novel aerospace adhesive," *Composites: Part B,* vol. 43, no. 2, pp. 240-248, March 2012.

[11] Automated Dynamics, "Composites for Aerospace," [Online]. Available: http://www.automateddynamics.com/markets/aerospace. [Accessed 13 April 2018].

[12] W. R. Broughton, L. E. Crocker and M. R. L. Gower, "Design Requirements for Bonded and Bolted Composite Structures," National Physical Laboratory, Teddington, UK, 2002.

[13] S. T. d. Freitas, Interviewee, *The adhesive bond is not the weakest link in current carbon fiber reinforced plastic stiffener to skin structures.* [Interview]. July/August 2016.

[14] D. A. Dillard, Advances in structural adhesive bonding, Cambridge: Woodhead Publishing Limited, 2010.

[15] L. Burns, A. Mouritz, D. Pook and S. Feih, "Bio-inspired hierarchical design of composite T-joints with improved structural properties," *Composites: Part B,* vol. 69, p. 222–231, 2015.

[16] M. Carneiro, R. Campinho and F. Silva, "Experimental and numerical analysis of adhesively-bonded T joints under peel loads," *Procedia Manufacturing ,* vol. 13, pp. 51-58, 2017.

[17] K. Vijayaraju, P. Mangalgiri and B. Dattaguru, "Experimental study of failure and failure progression in T-stiffened skins," *Composite Structures,* vol. 64, pp. 227-234, 2004.

[18] C. H. Kim, D. H. Jo and J. H. Choi, “Failure strength of composite T-joints prepared using a new 1-thread stitching process,” *Composite Structures,* vol. 178, p. 225–231, 2017.

[19] E. Greenhalgh and M. H. Garcia, “Fracture mechanisms and failure processes at stiffener run-outs in polymer matrix composite stiffened elements,” *Composites: Part A,* vol. 35, p. 1447–1458, 2004.

[20] H. Wu, J. Xiao, S. Xing, S. Wen, F. Yang and J. Yang, “Numerical and experimental investigation into failure of T700/bismaleimide composite T-joints under tensile loading,” *Composite Structures,* vol. 130, p. 63–74, 2015.

[21] C. Huang, “Study on co-cured composite panels with blade-shaped stiffeners,” *Composites: Part A,* vol. 34, p. 403–410, 2003.

[22] X. Ma, K. Bian, J.-y. Lu and K. Xiong, “Experimental research on detection for interface debond of CFRP T-joints under tensile load,” *Composite Structures,* vol. 158, p. 359–368, 2016.

[23] D. J. Haugen, “Fracture of Skin-Stiffener Intersections in Composite Wind Turbine Blade Structures,” Montana, 1998.

[24] R. Krueger, P. J. Minguet and T. K. O’Brien, “Implementation of interlaminar fracture mechanics in design: An overview,” in *14th International Conference on Composite Materials*, San Diego, 2003.

[25] R. Trask, S. Hallett, F. Helenon and M. Wisnom, “Influence of process induced defects on the failure of composite T-joint specimens,” *Composites: Part A,* vol. 43, p. 748–757, 2012.

[26] L. Burns, A. Mouritz, D. Pook and S. Feih, “Strengthening of composite T-joints using novel ply design approaches,” *Composites Part B,* vol. 88, pp. 73-84, 2016.

[27] D. D. Cartie, G. Dell’Anno, E. Poulin and I. K. Partridge, “3D reinforcement of stiffener-to-skin T-joints by Z-pinning and tufting,” *Engineering Fracture Mechanics,* vol. 73, p. 2532–2540, 2006.

[28] J. Bigaud, Z. Aboura, A. Martins and S. Verger, “Analysis of the mechanical behavior of composite T-joints reinforced by one side stitching,” *Composite Structures,* vol. 184, pp. 249-255, 2018.

[29] E. Greenhalgh, A. Lewis, R. Bowen and M. Grassi, “Evaluation of toughening concepts at structural features in CFRP—Part I: Stiffener pull-off,” *Composites: Part A,* vol. 37, p. 1521–1535, 2006.

[30] T. Koh, S. Feih and A. Mouritz, “Experimental determination of the structural properties and strengthening mechanisms of z-pinned composite T-joints,” *Composite Structures,* vol. 93, p. 2222–2230, 2011.

[31] M. Li, P. Chen, B. Kong, T. Peng, Z. Yao and X. Qiu, “Influences of thickness ratios of flange and skin of composite T-joints on the reinforcement effect of Z-pin,” *Composites Part B,* vol. 97, pp. 216-225, 2016.

[32] Y.-B. Park, B.-H. Lee, J.-H. Kweon, J.-H. Choi and I.-H. Choi, “The strength of composite bonded T-joints transversely reinforced by carbon pins,” *Composite Structures,* vol. 94, p. 625–634, 2012.

[33] T. A. S. Fuertes, T. Kruse, T. Körwien and M. Geistbeck, “Bonding of CFRP primary aerospace structures – discussion of the certification boundary conditions and related technology fields addressing the needs for development,” *Composite Interfaces,* vol. 22, no. 8, pp. 795-808, 2015.

[34] Scopus, “Analyze search results: Documents by year,” [Online]. Available: https://goo.gl/jkXaaD. [Accessed 2 June 2018].

[35] E. S. Greenhalgh, Failure analysis and fractography of polymer composites, Cambridge, UK: Woodhead Publishing Limited, 2009.

[36] M. Neto, A. Amaro, L. Roseiro, J. Cirne and R. Leal, Engineering Computation of Structures: The Finite Element Method, Springer, 2015.

[37] Federal Aviation Administration, “Advanced Composite Materials,” in *Aviation Maintenance Technician Handbook*, vol. 1, FAA, 2012.

[38] K. K. Chawla, Composite Materials: Science and Engineering, 3rd Edition ed., New York: Springer, 2012.

[39] M. Standridge, “Aerospace materials — past, present, and future,” 13 August 2014. [Online]. Available: http://www.aerospacemanufacturinganddesign.com/article/amd0814-materials-aerospace-manufacturing/. [Accessed 11 April 2018].

[40] R. Witik, F. Gaille, R. Teuscher, H. Ringwald, V. Michaud and J.-A. Månson, “Assessing the economic and evironmental potential of out of autoclave processing,” in *18th International Conference of Composite Materials* , 2011.

[41] Z. August, G. Ostrander, J. Michasiow and D. Hauber, “Recent developments in automated fiber placement of thermoplastic composites,” *Sampe Journal,* vol. 50, no. 2, pp. 30-37, March 2014.

[42] S. Das, J. Warren, D. West and S. M. Schexnayder, “Global Carbon Fiber Composites Supply Chain Competitiveness Analysis,” Clean Energy Manufacturing Analysis Center, Golden, Colorado, 2016.

[43] C. Grant, “Automated processes for composite aircraft structure,” *Industrial Robot: An International Journal,* vol. 33, no. 2, pp. 117-121, 2006.

[44] Automated Dynamics, “Composites Manufacturing Options,” [Online]. Available: http://www.automateddynamics.com/resources/innovation/automated-manufacturing-composites. [Accessed 21 January 2018].

[45] J. Sloan, “ATL and AFP: Defining the megatrends in composite aerostructures,” 30 June 2008. [Online]. Available: https://www.compositesworld.com/articles/atl-and-afp-defining-the-megatrends-in-composite-aerostructures. [Accessed 5 February 2018].

[46] C. Red, “The Outlook for Thermoplastics in Aerospace Composites, 2014-2023,” 1 September 2014. [Online]. Available: https://www.compositesworld.com/articles/the-outlook-for-thermoplastics-in-aerospace-composites-2014-2023. [Accessed 18 March 2018].

[47] A. Kinloch, B. Blackman and W. Teo, “The adhesive bonding of polymeric matrix composites,” in *17th International Conference on Composite Materials*, Edinburgh, UK, 2009.

[48] C. Ageorgesa, L. Yea and M. Houb, “Advances in fusion bonding techniques for joining thermoplastic matrix composites: a review,” *Composites: Part A,* vol. 32, pp. 839-857, 2001.

[49] S. Pappadà, A. Salomi, J. Montanaro, A. Passaro, A. Caruso and A. Maffezzoli, “Fabrication of a thermoplastic matrix composite stiffened panel by induction welding,” *Aerospace Science and Technology,* vol. 43, p. 314–320, 2015.

[50] Composites World, “Fiber reinforcement forms (2017),” 17 March 2016. [Online]. Available: https://www.compositesworld.com/articles/fiber-reinforcement-forms-2016. [Accessed 2018 April 2].

[51] R. Schledjewski, “Thermoplastic tape placement process – in situ consolidation is reachable,” *Plastics, Rubber and Composites,* vol. 38, no. 9-10, pp. 379-386, 2009.

[52] D. Modi, A. Comer, R. M. O’Higgins and M. A. McCarthy, “Thermoplastic composites: In-situ consolidation or in-situ welding?,” in *19th International Conference on Composite Materials*, Montreal, Canada, 2013.

[53] Z. Qureshi, T. Swait, R. Scaife and H. El-Dessouky, “In situ consolidation of thermoplastic prepreg tape using automated tape placement technology: Potential and possibilities,” *Composites: Part B,* vol. 66, p. 255–267, 2014.

[54] D. Gates, “MTorres aims to take carbon-fiber technology for jets to the next level,” 5 December 2017. [Online]. Available: https://www.seattletimes.com/business/boeing-aerospace/mtorres-aims-to-take-carbon-fiber-technology-for-jets-to-the-next-level/. [Accessed 20 April 2018].

[55] Adhesives tool kit, “Adhesive bonding - a guide to best practice,” [Online]. Available: http://www.adhesivestoolkit.com/Docu-Data/SurfacePreTreatment.xtp. [Accessed 22 April 2018].

[56] A. J. Kinloch, Adhesion and Adhesives: Science and Technology, Chapman & Hall, 1987.

[57] L. F. M. da Silva, A. Ochsner and R. D. Adams, Handbook of Adhesion Technology, Berlin: Springer Heidelberg, 2011.

[58] G. Gardiner, “Hole ambitions! Optimize? Customize?,” Gardner Business Media, Inc. , 4 September 2012. [Online]. Available: https://www.compositesworld.com/articles/hole-ambitions-optimize-customize. [Accessed 22 March 2018].

[59] N. Chowdhury, W. K. Chiu, J. Wang and P. Chang, “Static and fatigue testing thin riveted, bonded and hybrid carbon fiber double lap joints used in aircraft structures,” *Composite Structures,* vol. 121, p. 315–323, 2015.

[60] R. D. Adams and W. C. Wake, Adhesive Joints in Engineering, 2 ed., London: Chapman & Hall, 1997.

[61] S. Ebnesajjad and A. H. Landrock, Adhesives Technology Handbook, Third Edition ed., San Francisco: Elsevier, 2015.

[62] J. Shields, Adhesives handbook, Third Edition ed., Butterworth-Heinemann, 1984.

[63] C. C. Chamis and P. L. N. Murthy, “Simplified procedures for designing adhesively bonded composite joints,” *Journal of Reinforced Plastics and Composites,* vol. 10, no. 1, p. 29–41, 1991.

[64] ASTM International, “ASTM D5573-99(2012), Standard Practice for Classifying Failure Modes in Fiber-Reinforced-Plastic (FRP) Joints,” West Conshohocken, PA, 2012.

[65] P. Schreurs, “Fracture Mechanics,” Eindhoven University of Technology, Eindhoven, 2012.

[66] R. P. Romero and Á. L. Ramírez, “Analysis of rubber adhesive: FE simulation of damage propagation over rubber adhesive under fatigue in mixed-mode loading,” University of Skovde, Skovde (Sweden), 2014.

[67] “Principles and practices of adhesive bonded structural joints and repairs,” *International Journal of Adhesion & Adhesives* , vol. 19, pp. 91-105, 1999.

[68] J. Mohan, A. Ivankovic and N. Murphy, “Mode I fracture toughness of co-cured and secondary bonded composite joints,” *International Journal of Adhesion & Adhesives,* vol. 51, p. 13–22, 2014.

[69] S. M.G., K. J.H., C. J.H., B. J.H., S. M.H., S. S.J. and L. J., "Effect of manufacturing methods on the shear strength of composite single-lap bonded joints," *Composite Structures,* vol. 92, p. 2194–2202, 2010.

[70] J. Wingfield, "Treatment of composite surfaces for adhesive bonding," *International Journal of Adhesion and Adhesives* , vol. 13, no. 3, July 1993.

[71] G. Gardiner, "Wet and dry peel plies," 9 August 2016. [Online]. Available: https://www.compositesworld.com/blog/post/wet-and-dry-peel-plies. [Accessed 1 March 2018].

[72] M. Kanerva, E. Sarlin, M. Hoikkanen, K. Rämö, O. Saarela and J. Vuorinen, "Interface modification of glass fibre–polyester composite–composite joints using peel plies," *International Journal of Adhesion & Adhesives,* vol. 59, p. 40–52, 2015.

[73] A. Kozbial, Z. Li, C. Conaway, R. McGinley, S. Dhingra, V. Vahdat, F. Zhou, B. D'Urso, H. Liu and L. Li, "Study on the Surface Energy of Graphene by Contact Angle Measurements," *Langmuir,* vol. 30, no. 28, 2014.

[74] J. M. Arenas and J. J. A. C. Narbón, "Optimum adhesive thickness in structural adhesives joints using statistical techniques based on Weibull distribution," *International Journal of Adhesion & Adhesives,* vol. 30, p. 160–165, 2010.

[75] M. J. Hoke, "Adhesive Bonding of Adhesive Bonding of Composites Composites," Abaris Training Inc., Reno, Nevada.

[76] Federal Aviation Administration, "Chapter 1: Aircraft Structures," in *Aviation Maintenance Technician Handbook*, vol. 1, 2012.

[77] A. Sivia, J. Grewal, A. Bhinder and R. Saini, "A Study on the Skin-Stringer Panel of an Aircraft," *International Journal of Aerospace and Mechanical Engineering,* vol. 1, no. 1, 2014.

[78] R. T. Haftka and Z. Gürdal, Elements of Structural Optimization, Springer Netherlands, 1992.

[79] Y. K. (. B. C. Lin., "Stresses in Continuous Skin-Stiffener Panels Under Random Loading," *Journal of the Aerospace Sciences,* vol. 29, no. 1, pp. 67-75.

[80] J. T. S. Wang and S. B. Biggers, "Skin/Stiffener Interface Stresses in Composite Stiffened Panels," National Aeronautics and Space Administration, Langley, 1984.

[81] L. A. Burns, "Biomimetic Design of Aerospace Composite Joints," RMIT University, Melbourne, 2012.

[82] S. Kumari and P. Sinha, "Finite element analysis of composite wing T-joints," *Journal of Reinforced Plastics and Composites,* vol. 21, no. 17, pp. 1561-1585, 2002.

[83] Dassault Systèmes, "Abaqus Technology Brief (TB-05-VCCT-1)," 2007.

[84] R. Loendersloot, T. Ooijevaar, L. Warnet, A. de Boer and R. Akkerman, "Vibration based structural health monitoring of a composite plate with stiffeners," in *International Conference on Noise and Vibration Engineering*, Leuven, Belgium, 2010.

[85] M. T. v. H. Silva, P. P. Camanho, A. T. Marques and P. M. Castro, "3D-reinforcement techniques for co-bonded CFRP/CFRP and CFRP/metal joints: a brief review," *Ciência & Tecnologia dos Materiais ,* vol. 29, p. 102–107, 2017.

[86] Composite Materials (Italy) s.r.l., "REM Epoxy matrix," Legnano, December 2015.

[87] Composite Materials (Italy) s.r.l., "CIT HS160 T700 REM UD tape 36%," Legnano, November 2015.

[88] Composite Materials (Italy) s.r.l., “EA451 Adhesive Film,” Legnano, January 2015.

[89] J. A. B. P. Neto, “Estudo Paramétrico de Juntas Adesivas em Material Compósito,” Faculty of Engineering of the University of Porto, Porto, 2011.

[90] W. D. Bascom, “Durability of composites and adhesive bonds,” Naval Research Laboratory, Washington, D.C., 1977.

[91] L. F. da Silva, R. Adams and M. Gibbs, “ Manufacture of adhesive joints and bulk specimens with high-temperature adhesives,” *International Journal of Adhesion & Adhesives,* vol. 24, p. 69–83, 2004.

[92] W. D. Bascom and R. L. Cottington, “Air Entrapment in the Use of Structural Adhesive Films,” *The Journal of Adhesion,* vol. 4, no. 3, pp. 193-209, 1972.

[93] R. Chester and J. Roberts, “Void minimization in adhesive joints,” *International Journal of Adhesion and Adhesives,* vol. 9, no. 3, pp. 129-138, 1989.

[94] R. L. P. Patrick, Treatise on adhesion and adhesives: structural adhesives with emphasis on aerospace applications, vol. 4, New York: Marcel Dekker, 1976.

[95] ASTM International, “ASTM D638-14, Standard Test Method for Tensile Properties of Plastics,” West Conshohocken, PA,, 2014.

[96] L. Silva and R. Adams, “Measurement of the mechanical properties of structural adhesives in tension and shear over a wide range of temperatures,” *Journal of Adhesion Science and Technology,* vol. 19, no. 2, p. 109–141, 2005.

[97] ASTM International, “ASTM D5868-01(2014), Standard Test Method for Lap Shear Adhesion for Fiber Reinforced Plastic (FRP) Bonding,” West Conshohocken, PA, 2014.

[98] L. F. da Silva, D. A. Dillard, B. Blackman and R. D. Adams, Testing Adhesive Joints: Best practices, Weinheim: Wiley-VCH, 2012.

[99] R. Garcia and P. Prabhakar, “Bond interface design for single lap joints using polymeric additive manufacturing,” *Composite Structures,* vol. 176, p. 547–555, 2017.

[100] Y. Boutar, S. Naïmi, S. Mezlini and M. B. S. Ali, “Effect of surface treatment on the shear strength of aluminium adhesive single-lap joints for automotive applications,” *International Journal of Adhesion & Adhesives,* vol. 67, p. 38–43, 2016.

[101] G. A. Allen, J. C. Dinkel and J. S. Sentz, “Method for fabricating an advanced composite aerostructure article having an integral co-cured fly away hollow mandrel”. United States Patent US006458309B1, 1 October 2002.

[102] C. C. Pancorbo, R. D. Casado, M. D. C. Nodal, A. P. Pastor, A. G. Garcia and M. H. Garcia, “Process for manufacturing pre-cured parts of composite material with green-applied stiffeners”. United States Patent US006508909B1, 21 January 2003.

[103] Kismarton and M. U., “Composite stiffeners for aerospace vehicles”. United States Patent USOO8720825B2, 13 May 2014.

[104] P. N. Vines, A. G. Garcia and C. C. Pancorbo, “Method for manufacturing elements of composite materials by the co-bonding technique”. United States Patent US 20020144401A1, 10 October 2002.

[105] A. P. Pastor, J. S. Fernández and F. E. García, “Method for manufacturing "T" shaped stringer for an aircraft and curing tool used thereof”. United States Patent US 20110315307A1, 29 December 2011.

[106] P. L. M. Royo, F. E. Benavides, A. P. Pastor and I. P. Garcia, “Stringers made of composite material with a bulb”. United States Patent US 20070039284A1, 22 February 2007.

[107] M. Danzi, “Manufacturing of polymer composites OOA prepreg technology”.

[108] AZO Materials, “Debulking and autoclave processing for tooling materials,” 24 October 2013. [Online]. Available: https://www.azom.com/article.aspx?ArticleID=10210. [Accessed 3 December 2017].

[109] P. F. Mayuet, F. Girotb, A. Lamíkiz, S. Fernández-Vidal, J. Salguero and M. Marcos, “SOM/SEM based characterization of internal delaminations of CFRP samples machined by AWJM,” in *The Manufacturing Engineering Society International Conference*, 2015.

[110] E. Gadelmawlaa, M. Kourab, T. Maksoudc, I. Elewaa and H. Soliman, “Roughness parameters,” *Journal of Materials Processing Technology,* vol. 123, no. 1, pp. 133-145, 2002.

[111] F. F. Farshad, T. C. Pesacreta, J. D. Garber and S. R. Bikki, “A comparison of surface roughness of pipes as measured by two profilometers and atomic force microscopy,” *Scanning,* vol. 23, pp. 241-248, 2001.

[112] A. Barbosa, L. da Silva, J. Abenojar, M. Figueiredo and A. Ochsner, “Toughness of a brittle epoxy resin reinforced with micro cork particles: Effect of size, amount and surface treatment,” *Composites Part B,* vol. 114, pp. 299-310, 2017.

[113] P. Santos, “Resistência ao Impacto de Compósitos Híbridos,” Universidade da Beira Interior, Covilhã, 2010.

[114] R. Lokhande, A. Deshpande and A. Mache, “Taguchi Analysis of Bonded Single-Lap Joint in Hemp Fiber Composite,” *International Journal of Engineering Technology and Sciences,* vol. 5, June 2016.

[115] B. D. Flinn, B. K. Clark, J. Satterwhite and P. J. V. Voast, “Influence of peel ply type on adhesive bonding of composites,” Soceity of Advancement of Materials and Process Engineering (SAMPE), Seattle, 2008.

[116] H. E. Bennett and J. O. Porteus, “Relation Between Surface Roughness and Specular Reflectance at Normal Incidence,” *Journal of the Optical Society of America,* vol. 51, no. 2, pp. 123-129, 1961.

[117] J. D. Hochhalter, “Replicated Mirrors using Carbon Fiber Reinforced Polymers,” University of New Mexico, 2005.

[118] B. D. Flinn and A. C. Tracey, “Improving adhesive bonding of composites through surface characterization: Variables that affect contact angle measurements on peel ply surfaces,” Seattle, WA, 2009.

[119] R. N. Wenzel, “Resistance of Solid Surfaces to Wetting by Water,” *Industrial & Engineering Chemistry,* vol. 28, no. 8, pp. 988-994, 1936.

[120] G. Wolansky and A. Marmur, “Apparent contact angles on rough surfaces: the Wenzel equation revisited,” *Colloids and Surfaces A: Physicochemical and Engineering Aspects,* vol. 156, p. 381–388, 1999.

[121] M. Davis and A. McGregor, “Failure in Real Bonded Structures: Adhesive Bond Failure Forensics,” Adhesion Associates; Prosolve, March 2016.

[122] E. Greenhalgh and M. Hiley, “Fractography of polymer composites: current status and future issues,” in *13th European conference on composite materials*, Stockholm, Sweden, 2008.

[123] J. V. Cardoso, J. N. Pereira and A. P. Silva, “Fabrication of adhesively-bonded CFRP T-joints for stiffener pull-off tests,” in *XVI Portuguese Conference on Fracture 2018*, Covilhã, 2018.

This page intentionally left blank

Annex A

	Comments	Service temperature (ºC)	Cure
Epoxy	High strength and temperature resistance, relatively low cure temperatures, easy to use, low cost	-40 to +100 (180*)	One-part epoxies cure with temperature. Two-part epoxies cure at room temperature (cure can be accelerated with temperature)
Cyanoacrylates	Fast bonding capability to plastic and rubber but poor resistance to moisture and temperature	-30 to +80	Fast cure (second or minutes) upon exposure to moisture at room temperature
Anaerobics	Designed for fastening and sealing applications in which a tight seal must be formed without light, heat or oxygen, suitable for bonding cylindrical shapes	-55 to +150	Cure in the absence of air or oxygen at room temperature
Acrylics	Versatile adhesives with capabilities of fast curing and tolerate dirtier and less prepared surfaces	-40 to +120	Cure through a free radical mechanism
Polyurethanes	Good flexibility at low temperatures and resistant to fatigue, impact resistance, and durability	-200 to +80	Room temperature
Silicones	Excellent sealant for low stress applications, high degree of flexibility and very high temperature resistance, capability to seal or bond materials of various natures, long cure times, and low strength	-60 to +300 (350**)	Room temperature
Phenolics	Good strength retention for short periods of time, limited resistance to thermal shocks	-40 to +175 (260**)	Cure with temperature and high pressure
Polyimides	Thermal stability, dependent on a number of factors, difficult processability	-40 to +250 (300**)	Cure with temperature and high pressure
Bismaleimides	Very rigid, low peel properties	-50 to +200 (230**)	Cure with temperature and high pressure

*With different filler materials; **intermittent.

From: M. Banea and L. da Silva, "Adhesively bonded joints in composite materials: An overview," *Proceedings of the Institution of Mechanical Engineers Part L Journal of Materials Design and Applications* , January 2009 [8].

Glossary

For the benefit of the reader, a glossary of some of the terms used regarding the subject of adhesive bonding is presented below. Most of the terms were reproduced from the draft European standard prEN 923.

Adherend: A body that is, or is intended to be, held to another body by an adhesive.

Adhesion: The state in which two surfaces are held together by surface bonds.

Adhesive: A non-metallic substance capable of joining materials by surface bonding (adhesion), and the bond possessing adequate internal strength (cohesion).

Adhesive, Bonding: material joining process in which an adhesive, placed between the adherend surfaces, solidifies to produce an adhesive bond.

Adhesive, Contact: An adhesive that is applied to both adherends and when allowed to become apparently dry will instantly develop a firm bond when applying a vigorous but not sustained pressure.

Bond: A joint between adherends achieved by an adhesive. To join adherends by means of an adhesive.

Bond Strength: The stress necessary to bring an adhesive joint to the point of failure with failure occurring in or near the plane of the bond-line.

Cohesion: The state in which the particles of a single substance are held together by primary or secondary valence forces.

Cure: To change the physical properties of a material (usually from a liquid to a solid) by chemical reaction, by the action of heat and catalysts, alone or in combination, with or without pressure.

Failure, Adhesive: The failure of an adhesive bond such that the separation appears to be at the adhesive/adherend interface.

Failure, Cohesive: Failure within the body of the adhesive, i.e. not at the interface. An adhesive in film form, with or without a carrier.

Film Adhesive: An adhesive in film form, with or without a carrier.

Bondline Thickness: Thickness of the fully cured adhesive layer.

High Energy Surfaces: Thermodynamically, typical high energy surfaces are found on clean ceramics and metals.

Joint: A junction of two adjacent adherends.

Low Energy Surfaces: Thermodynamically, typical low energy surfaces are found on plastics and composites and are difficult to bond to, without some surface treatment.

Primer: A chemical coating which may be applied to an adherend prior to application of adhesive, to stabilise a pre-treated surface, to improve adhesion and/or to improve durability, e.g. performance in hot/wet environments.

Resin: A solid, semi-solid or liquid, usually organic material that has an indefinite and often high molecular mass and, when solid, usually has a softening or melting range and gives a conchoidal fracture. In a broader sense, the term is used to designate any polymer that is the basic material for plastics.

Sealant: An adhesive material, used to fill gaps where movement may occur in service and, when set, has elastic properties, e.g. silicone window frame sealants. The term is also used for a material filling a void against the ingress or egress of a fluid under pressure, e.g. anaerobic engine block flange sealants.

Shelf Life: The time of storage under stated conditions during which an adhesive may be expected to retain its working properties.

Structural: The term used to describe a bond, or an adhesive, if it is capable of sustaining in a structure, a specified strength level under a combination of stresses for a long period of time. The combination of stresses may include peel and shear forces, fluctuating loads, environmental exposure, or steady load.

Tack: The property of a material that enables it to form a bond immediately on contact with another surface which may be an adherend or another layer of adhesive.

Thermoplastics: Plastics capable of being repeatedly softened by increases in temperature and hardened by decreases in temperature.

Thermosets: Polymers or copolymers which, when cured by heat or other means, change into substantially infusible and insoluble products.

Time, Curing: The period of time during which an assembly is subjected to heat or pressure, or both, to cure the adhesive.

Untreated Surface: A surface which has not been cleaned (may still be in the state as supplied by the manufacturer).

Wetting: The ability of a liquid (adhesive) to spread on a specific solid surface.